

Surface Resistance Minimization in SRF Cavities by Reduction of Thermocurrents and Trapped Flux

DISSERTATION

zur Erlangung des Grades eines Doktors
der Naturwissenschaften

vorgelegt von

M.Sc. Julia-Marie Köszegi

eingereicht bei der

Naturwissenschaftlich-Technischen Fakultät
der Universität Siegen

1. Gutachter: Prof. Jens Knobloch

2. Gutachter: Prof. Andreas Jankowiak

Datum der mündlichen Prüfung: 8. Juni 2017

Abstract

Trapped magnetic flux is known to be a major cause of radio-frequency (RF) dissipation in superconducting RF cavities for particle accelerators. Especially in many new machines, which operate at high field in the continuous-wave mode, these additional losses can be unacceptably high, both from an operational and economic point of view.

Recent measurements demonstrated that the procedure with which SRF cavities are cooled to the superconducting state dramatically impacts the niobium surface resistance which in turn governs the RF power dissipation. We found a direct correlation between the temperature difference during cooldown and the surface resistance. We believe that thermocurrents generated during the cooldown at the niobium cavity and the titanium tank, which holds the helium, generate a magnetic field. This field is subsequently trapped when the cavity transitions to the superconducting state.

To determine the extent of thermocurrents, the thermopowers of niobium and titanium were measured in the temperature range from 10 K to 100 K. Numerical simulations of the cavity system were performed based on these results. The obtained current distribution was used to estimate the magnetic field at the RF surface of the cavity, which critically depends on the temperature profile of the cavity. Direct measurements of the trapped flux confirmed the simulations and were consistent with the observed increase in surface resistance.

The extent to which the magnetic flux is actually trapped also depends on the cooldown conditions. Recent experimental findings, including those of other groups and a theoretical description, were compiled. Two selected topics were addressed by additional measurements. For one, we studied the flux expulsion in a conduction-cooled cavity and found that it is favored by a homogenous temperature profile during the superconducting transition. Secondly, we used magneto-optical studies to visualize the different shapes of the superconducting phase front during either cooldown or during field penetration. The results provide important starting points for further investigations of flux expulsion.

Zusammenfassung

Eingefrorener magnetischer Fluss ist eine bekannte Ursache der hochfrequenz (HF) Verluste in supraleitenden HF Resonatoren für Teilchenbeschleuniger. Insbesondere für neue Beschleuniger, die mit hohen Feldern im Dauerstrichbetrieb arbeiten, können diese Verluste sowohl von einem betrieblichen als auch einem wirtschaftlichem Gesichtspunkt her unakzeptabel hoch werden.

Wie jüngste Messungen zeigen, hat die Abkühlprozedur, mit der SHF Resonatoren auf Betriebstemperatur gebracht werden, einen deutlichen Einfluss auf den Oberflächenwiderstand des Niobs und damit die HF Verluste. Wir haben einen direkten Zusammenhang zwischen den Temperaturunterschieden während des Abkühlens und dem Oberflächenwiderstand gefunden. Die vermutliche Ursache hierfür sind Thermoströme, die während des Abkühlvorgangs im System aus Niobresonator und dem aus Titan gefertigtem Heliumtank entstehen. Diese Ströme generieren ein Magnetfeld, das im Material während des supraleitenden Phasenübergangs eingefroren wird.

Um die Thermoströme zu quantifizieren wurden die Seebeck-Koeffizienten von Niob und Titan im Temperaturbereich von 10 K bis 100 K gemessen. Auf dieser Grundlage wurden numerische Simulationen des Resonatorsystems durchgeführt und aus der errechneten Stromverteilung anschließend das Magnetfeld an der HF Oberfläche bestimmt. Dieses hing kritisch von der Temperaturverteilung im System ab. Eine direkte Messung des eingefrorenen Flusses bestätigte die Ergebnisse der Simulationen und war konsistent mit dem ermittelten Anstieg des Oberflächenwiderstandes.

Die Menge des tatsächlich eingefrorenen Flusses hängt außerdem stark von den Abkühlbedingungen ab. Aktuelle Studien zu diesem Thema, einschließlich experimenteller Ergebnisse anderer Gruppen und einer theoretischen Beschreibung, wurden zusammengefasst und zwei ausgewählte Fragestellungen mit zusätzlichen Experimenten vertieft. Dafür wurde zum einen ein durch Wärmeleitung gekühlter Niobresonator untersucht. Hierbei wurde die Flussverdrängung durch gleichförmiges Abkühlen während des supraleitenden Phasenübergangs verbessert. Im Anschluss wurden magneto-optische Messungen durchgeführt um die unterschiedlich geformten Phasenfronten, zum einen während des Abkühlens und zum anderen während des Eindringens des Magnetfelds, sichtbar zu machen. Die dabei identifizierten Unterschiede liefern einen wichtigen Ausgangspunkt für weiterführende Studien zur effektiven Flussverdrängung.

To Alfred Vogt

Contents

List of Figures	iii
List of Tables	vi
List of Symbols and Abbreviations	vii
1 Introduction: Pushing Niobium to its Limits	1
2 Basic Principles	9
2.1 RF Cavities for Particle Acceleration	9
2.1.1 RF Resonators	10
2.1.2 Figures of Merit	10
2.2 RF Superconductivity	12
2.2.1 The Origin of Superconductivity	12
2.2.2 Phenomenology and Theoretical Descriptions	14
2.2.3 AC Losses in Superconductors	17
2.2.4 Knobs for the Reduction of RF Dissipation	20
2.3 Trapped Magnetic Flux	21
2.3.1 The Structure of a Flux Line	21
2.3.2 Flux Pinning	23
2.3.3 Losses Due to Trapped Flux	25
2.3.4 Sources of Magnetic Field in the SRF Environment	31
2.4 Thermoelectric Currents	32
2.4.1 Thermoelectric Currents in the SRF Environment	32
2.4.2 The Thermoelectric Effect	35
2.5 Experimental Methods	40
2.5.1 The HoBiCaT Cryostat	40
2.5.2 Measurement of the Quality Factor and the Accelerating Field	41
2.5.3 Measurement of the Magnetic Field	45
2.5.4 Measurement of the Temperature	50

3	Evidence of Thermoelectric Loss Contribution in Cavity Tests	51
3.1	The TESLA Cavity and Its Passband Modes	52
3.2	HoBiCaT Cooldown Schemes	54
3.3	The BCP Cavity	57
3.3.1	The BCS and the Residual Resistance	58
3.3.2	Correlation of Residual Resistance and Cooling Parameters	59
3.3.3	Spatial Distribution of the Losses	64
3.4	The N-Doped Cavity	66
3.4.1	The BCS and the Residual Resistance	67
3.4.2	Correlation of Residual Resistance and Cooling Parameters	68
3.4.3	Correlation of Residual Resistance and Directly Measured Magnetic Field	69
4	Estimate of Thermoelectrically Generated Magnetic Field	72
4.1	The Thermopower	73
4.1.1	The Thermopower in Literature	73
4.1.2	The Thermopower Measurement Setup (PPMS)	75
4.1.3	Software and Data Analysis	76
4.1.4	Results	78
4.2	The Thermovoltage as a Function of Temperature	80
4.3	The Thermocurrent and Its Magnetic Field	81
4.3.1	Thermocurrent: Simulation of Two Coaxial Cylinders	82
4.3.2	Thermocurrent: Simulation of the Cavity Geometry	87
4.4	Direct Measurement of the Magnetic Field at the RF Surface	95
4.4.1	Change in Magnetic Field During a Cycle	96
4.4.2	Phase Transition and Trapped Flux	99
4.4.3	Comparison to RF Data	102
4.4.4	Comparison to Simulations	103
4.5	Discussion: Thermocurrents in SRF Cavities	103
5	Flux Trapping and Flux Expulsion	105
5.1	The Kinetics of the Phase Transition in Superconductors	106
5.2	Recent Progress in SRF Science	109
5.3	Tests on Samples	110
5.3.1	3 GHz Cavity	110
5.3.2	Magneto-optical Imaging	116
5.4	Discussion: Flux Trapping and Flux Expulsion	127

6 Summary and Outlook	128
6.1 Conclusions	128
6.1.1 Thermocurrents	128
6.1.2 Flux Expulsion	130
6.2 Outlook	130
Appendices	132
A The Thermoelectric Effect: Charge and Heat Currents	133
B The Fluxgate Magnetometer in Detail	135
C The AMR Sensor in Detail	137
D Measured Thermopower Values as a Table	140
E AMR Sensors for SRF Application	141
Acknowledgements	151

List of Figures

1.1	Single cavity refrigeration and overall wall-plug power for the 35 LCLS-II modules.	3
1.2	Schematic diagram of the BCS resistance and the sensitivity to trapped flux as a function of electron mean free path.	4
1.4	Line of argument for thermocurrents.	7
2.1	A TESLA-type cavity fabricated from niobium.	9
2.2	Sketch of the electric and magnetic field in the fundamental TM_{010} mode.	10
2.3	The critical fields of a type-II superconductor.	14
2.4	Spatial variations of the order parameter and the magnetic flux density in a flux line.	22
2.5	Variation in energy when a flux line passes through a pinning center and the variation of the interaction force.	24
2.6	Trapped flux lines in a superconducting cavity wall.	26
2.7	Oscillation of a flux line in superconducting niobium.	28
2.8	Line of argument for thermocurrents.	34
2.9	Sketch to explain Seebeck voltage.	37
2.10	Seebeck voltage for different temperature profiles.	38
2.11	Seebeck voltage for superconductor and equal materials.	38
2.12	The HoBiCaT cryostat.	40
2.13	Nine-cell cavity in a horizontal test assembly.	41
2.14	RF measurement setup at HoBiCaT with phase-locked-loop.	42
2.15	Forward and reflected power during a pulsed measurement.	44
2.16	Detectable field range for several magnetic field sensing technologies.	46
2.17	Cross section of a fluxgate magnetometer.	47
2.18	AMR sensor: Ferromagnetic thin film with 45° shorting bars.	49
3.1	Field distributions of three passband modes of a TESLA-type cavity.	53
3.2	Field orientation in the π , $8/9\pi$ and $1/9\pi$ mode.	53
3.3	The earth's magnetic field inside the HoBiCaT cryostat at room temperature.	54
3.4	Cryoplant setup of HoBiCaT.	55

3.5	Temperatures during the different cooling schemes.	56
3.6	BCS fits of three measurements.	58
3.7	Average R_{res} measured in three passband modes as a function of the temperature difference along the cavity.	61
3.8	Residual resistance measured in the three passband modes as a function of ΔT_{av} , ΔT_{min} and ΔT_{max}	63
3.9	Shifted residual resistance values versus scaled temperature differences.	63
3.10	R_{res} for the $1/9\pi$ mode and $8/9\pi$ mode as a function of R_{res} obtained for the π mode.	65
3.11	Positions of the temperature and magnetic field sensors.	67
3.12	Residual resistance measured in two passband modes as a function of the temperature difference along the cavity in an N-doped cavity.	69
3.13	Temperature and magnetic field data during the cooldown and Cycle 12.	70
3.14	Residual resistance as a function of the peak magnetic field.	71
4.1	Literature values for the thermopower of Nb and Ti.	74
4.2	A PPMS sample mounted to the thermal transport option.	75
4.3	PPMS temperature and voltage response to a heater pulse at the hot and the cold thermometer.	76
4.4	PPMS data for a niobium sample at 150 K for four different heating periods.	77
4.5	The thermopower of the titanium samples.	78
4.6	The thermopower of the niobium samples.	79
4.7	The experimental data of Figure 3.9 with the integrated thermovoltage.	81
4.8	Simplified geometry for numerical simulations.	82
4.9	Different boundary areas outside of the tank in the Comsol simulations.	83
4.10	Coordinates for exporting the magnetic field distribution.	85
4.11	The absolute magnetic field at in r direction and in ϕ direction.	86
4.12	The absolute magnetic field and the top-bottom temperature difference in z direction and ϕ direction.	87
4.13	Comsol model of the cavity in the tank with adjusted resistance and magnetic shielding.	88
4.14	Heat capacity C_p , thermal conductivity κ and electrical conductivity σ data used for the Comsol simulations.	89
4.15	Magnetic field inside cavity and tank in a logarithmic scale for Study 5 temperature boundaries.	90
4.16	Simulated magnetic field across the cavity.	91
4.17	Magnetic field distribution around a growing superconducting spot.	92
4.18	Magnetic field of a growing superconducting spot.	93
4.19	Generic magnetic field peak in the measurements together with simulated magnetic field values.	94

LIST OF FIGURES

4.20	Positions of the six fluxgates for the direct measurement of the magnetic field inside the cavity.	96
4.21	Temperatures on the tank and magnetic field values inside the cavity during Cycle 4.	97
4.22	Change in magnetic field during Cycles 5 and 8.	98
4.23	Direct measurement of the trapped inside the cavity by six fluxgates.	99
4.24	Directly measured trapped flux in cells 1, 5 and 9 together with conceivable distributions of trapped magnetic flux in all nine cells.	101
4.25	RF data from Figure 3.10 compared to conceivable distributions of trapped flux.	101
5.1	A rod in a longitudinal magnetic field during sc phase transition.	107
5.2	Photo of the 3 GHz three-cell cavity with brackets and posts.	110
5.3	Setup of the 3 GHz cavity with three fluxgates and five Cernox sensors.	111
5.4	Various cooling parameters for evaluation of the 3 GHz cavity test.	112
5.5	Temperature at Cx1 and magnetic field at FG1 during an oscillation of the cavity temperature around the transition temperature.	113
5.6	Magnetic field measured during phase transitions	114
5.7	The expelled magnetic field measured in the superconducting state as a function of temperature difference between the cavity equators.	115
5.8	Photo of the MO imaging setup.	117
5.9	Microscopic image of the sample surface (magnification 10x).	117
5.10	Setup of imaging with a magneto-optical indicator film.	118
5.11	Sequence of the applied magnetic field during the magnetic field loop.	119
5.12	Penetration of magnetic field during the magnetic field loop.	120
5.13	Direct comparison of the machining marks and the flux penetration pattern (Figure 5.12(d)).	121
5.14	The relative grey scale values of Figures 5.12(f) and (g).	121
5.15	Trapped flux after field cooling in 10 mT (magnification 10x).	122
5.17	Phase front propagation during cooldown in an AC field	125
5.18	Contours of trapped flux pattern that indicate the shape of the phase front or a magnetic field loop and for a cooldown in AC field.	126
B.1	Sketch of a fluxgate magnetometer.	135
C.1	AMR sensor: Ferromagnetic thin film with 45° shorting bars.	138
C.2	AMR with typical Wheatstone bridge of four ferromagnetic thin films.	138
E.1	Direct measurement of the magnetic field inside the cavity.	141
E.2	Output of magnetic field sensors during thermal cycles.	142
E.3	Direct comparison of fluxgate and AMR signal during Cycle 15.	143

List of Tables

2.1	Material parameters for niobium.	17
2.2	Thermocurrent density in a closed loop.	39
3.1	TESLA cavity design parameters and simulated values.	52
3.2	Examples of measured residual resistances of the three passband modes.	59
4.1	Results of the simulations.	84
D.1	Thermopower of niobium and titanium between 10 K and 100 K.	140

Symbols

a, b	Fit parameters.
$\alpha(T)$ and $\beta(T)$	Expansion coefficients of free energy in GL theory.
\mathbf{B}	Magnetic field vector.
β	Ratio of particle speed v to the speed of light c .
2Δ	Superconducting energy gap.
\mathbf{E}	Electric field vector.
e	Elementary charge $e = 1.6022 \cdot 10^{-19}$ C.
E_{acc}	Accelerating electric field.
G	Geometry factor.
\mathbf{H}	Magnetic field vector.
\hbar	Planck constant $\hbar = 1.0546 \cdot 10^{-34}$ J s.
H_{c1}	Lower critical magnetic field.
H_{c2}	Upper critical magnetic field.
\mathbf{J}_s	Superconducting current density.
κ	Ginzburg-Landau parameter $\kappa = \lambda_L/\xi_{\text{GL}}$.
k	Boltzmann constant $k = 1.3806 \cdot 10^{-23}$ m ² kg/s ² /K.
l	Mean free path.
λ_L	London penetration depth.
m	Mass.
μ_0	Vacuum permeability.
n_0	Sum of superconducting and normal conducting particles.
n_n	Number of normal conducting particles.
n_s	Number of superconducting particles.
ω_0, f_0	Resonance frequency.
P_{diss}	Power dissipated inside a cavity wall.
P_f	Power directed to a cavity, forward power.
P_r	Power reflected by the cavity.
P_t	Power transmitted through the cavity.
ϕ_0	Magnetic flux quantum.
ψ	Complex pseudowave-function, order parameter in GL theory.
$ \psi ^2$	Local density of sc charge carriers in GL theory.
Q_0	Unloaded quality factor.
Q_L	Loaded quality factor.
R_{BCS}	Bardeen-Cooper-Schrieffer surface resistance.
R_{res}	Residual resistance.

RRR	Residual resistance ratio.
R_s	Surface resistance.
S	Seebeck coefficient, also called thermopower.
σ_n	Electrical conductivity in the normal state.
τ_L	Exponential decay time of stored energy in a cavity.
T_c	Critical temperature.
ξ_{GL}	Ginzburg-Landau coherence length.

Abbreviations

AC	Alternating current.
AMR	Anisotropic magnetoresistive effect.
BCP	Buffer Chemical Polishing.
BCS	Bardeen, Cooper and Schrieffer.
bERLinPro	Berlin Energy Recovery Linac Project.
BESSY-VSR	Variable pulse-length storage ring project at Berliner Elektronenspeicherring-Gesellschaft für Synchrotronstrahlung.
CD	Cooldown.
CERN	European Organization for Nuclear Research.
CW	Continuous wave.
Cx	Cernox sensor.
DC	Direct current.
DESY	Deutsches Elektronen-Synchrotron.
ESS	European Spallation Source.
FCC	Future Circular Collider.
FG	Fluxgate magnetometer.
FRIB	Facility for Rare Isotope Beams.
FV	Filling valve in the HoBiCaT cryostat.
GL	Ginzburg-Landau.
HIE-ISOLDE	High Intensity and Energy Isotope Separator On Line Device.
HoBiCaT	Horizontal bi-cavity test facility.
HOM	Higher order mode.
HZB	Helmholtz-Zentrum Berlin.
ILC	International Linear Collider.
JTV	Joule-Thomson valve in the HoBiCaT cryostat.
LCLS-II	Linac Coherent Light Source II.
LHe	Liquid helium.
LN	Liquid nitrogen.
nc	Normal conducting.
RF	Radio frequency.
sc	Superconducting.
SLAC	Stanford Linear Accelerator Center.
SRF	Superconducting radio-frequency.
TESLA	TeV-Energy Superconducting Linear Accelerator.
XFEL	European X-Ray Free-Electron Laser.

Chapter 1

Introduction: Pushing Niobium to its Limits

Worldwide, more than 30,000 accelerators are currently operated for the most diverse purposes [1]. The applications include medical therapy, ion implantation and industrial processing, but the largest and most fascinating machines are operated in science. Accelerators provide particle beams for high-energy and nuclear physics. Recent examples of such machines are the electron-positron International Linear Collider (ILC) and Future Circular Collider (FCC), which is the follow-on project of the Large Hadron Collider. Both accelerators are in the planning stage. Apart from the beam itself, the synchrotron radiation emitted by the accelerated particles is a vital tool of solid-state physics and materials science. Light sources, which are currently in construction, are the European X-Ray Free-Electron Laser (XFEL) and Linac Coherent Light Source II (LCLS-II). These projects, colliders as well as light sources, have one thing in common: They all rely on superconducting radio-frequency (SRF) cavities to transfer energy to the particle beam.

Advantages of SRF Cavities

The outstanding properties of SRF cavities can be illustrated with the example of light sources. A common trend for them is to require some combination of continuous wave (CW) operation, high average currents, short pulses, low beam emittance and little energy spread [2]. Normal conducting cavities reach their limitations at such combinations. With them, the design considerations must mainly focus on the reduction of the very large power dissipation. A high shunt impedance, small beam tubes and high RF frequencies are required. Yet, the desired current and beam brightness can still get limited due to higher-order-mode-driven beam instabilities. The influence of such higher order modes (HOMs) must therefore be minimized. One possible

approach is to open the beam tubes further. The HOMs then propagate through them and to an absorber. Thereby their impact diminishes. However, the larger beam tubes also lead to an unwanted increase in power dissipation in return.

Similar to the beam tube quandary, almost all design approaches concerning high currents compete with the goals for loss reduction. Normal conducting cavities cannot reconcile the diverging demands to achieve the desired beam parameters. SRF cavities offer a solution. They have a surface resistance several orders of magnitude below that of copper. Power dissipation requirements can hence be relaxed, which allows for large beam pipes, HOM-optimized shunt impedances and other modifications. High currents can be accelerated. Flexible pulse lengths and CW beams required for free electron lasers and energy recovery linacs become feasible. Moreover, SRF cavities preserve extraordinarily low emittances, which are required for e.g. the ILC project.

Limits of SRF Cavities

Despite the many advantages, SRF cavities are limited in their performance. Over the last decades, SRF research focused on the achievement of higher accelerating gradients (above 30 MV m^{-1}) to increase the real-estate gradient of the proposed projects. Thereby, the number of cavities needed for a desired total energy was reduced and, more important, the accelerators became smaller.

The second limit of SRF cavity performance is the dissipated power at the low operation temperature of about 2 K. A cavity's surface resistance R_s is usually described as composed of a temperature-dependent BCS term R_{BCS} (named after the Bardeen-Cooper-Schrieffer theory of superconductivity) and a residual resistance R_{res} , which does not change with temperature [3]. The BCS surface resistance can be explained by analysis of the charge carriers in the superconductor. Below transition temperature, the conduction electrons start to form Cooper pairs. Superconducting Cooper pairs have zero resistance for DC currents but since they have a mass and momentum, they cannot instantly shield RF field from the normal conducting electrons and small RF losses rise. R_{BCS} accounts for that contribution. All other effects, which cause additional losses, are summarized in the residual resistance.

The losses in SRF cavities are lower by a factor of about 10^6 compared to normal conducting structures. However, they are still critical because every dissipated watt in the cavity requires about one kilowatt of wall-plug power for the cryoplant due to the fundamental limitation given by Carnot efficiency. The cryoplant can therefore easily become one of the main cost drivers of an accelerator project. Previous machines with focus on high gradients operated at low repetition rates and required good quality

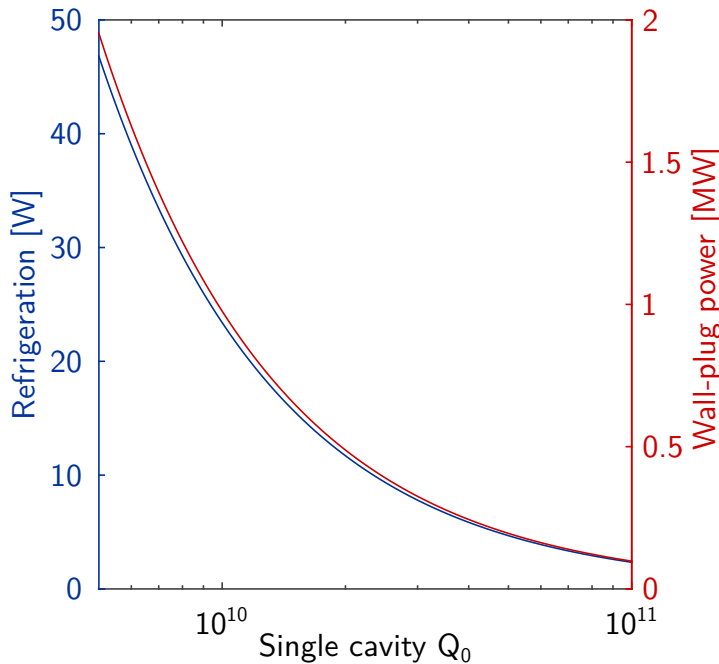


Figure 1.1: The refrigeration of a single cavity and the overall wall-plug power for the 35 LCLS-II modules^a operated at 15 MV m^{-1} and 2 K as a function of the single cavity quality factor.

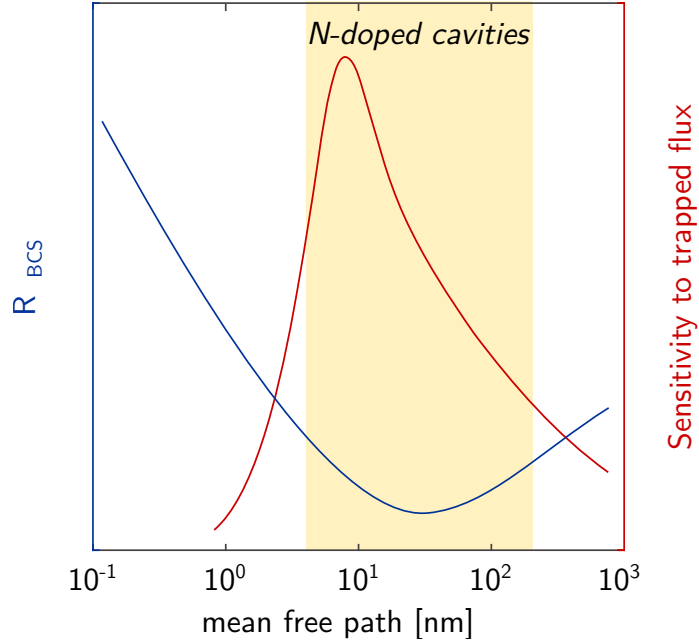
^a8 Cavities per module [4], Cavity parameters from [6]

factors Q_0 ($Q_0 \propto 1/R_s$) of about 10^{10} . Accelerators operating with CW beams, however, demand a quality factor that is at least twice as high. LCLS-II cavities, as one examples, will operate at a moderate gradient and are specified to achieve at least a Q_0 of $2.7 \cdot 10^{10}$. Figure 1.1 shows how the needed wall-plug power for the refrigeration of all 35 modules of the LCLS-II accelerator[4] increases when the average quality factor of the single cavities is reduced. The capital cost for the cryoplant rises accordingly - by several million euros [5].

To give further examples for the importance high Q -cavities, the XFEL does not run in CW mode, however, it employs about 800 superconducting cavities [7] and for that reason alone the losses must be kept at bay. Apart from light sources, several proposed types of the FCC require very high beam currents and will therefore also operate SRF cavities at high repetition rates [8].

The number of the by now mentioned machines demonstrates the high level of reliability that SRF cavities have already achieved, as well as the large number of projects that can benefit from further improvement. Thinking beyond the scope of large scale accelerators, SRF research that focuses on Q_0 improvement can also lead to a strong simplification in the cryoplants and thereby enable compact accelerators for smaller laboratories and turnkey systems for industrial application.

Figure 1.2: A schematic diagram of the BCS resistance from [11] and the sensitivity to trapped flux from [12] as a function of electron mean free path.



The Surface Resistance Challenge

Approaches on Q_0 improvement are usually surface treatment processes during manufacture. One recent example for a new cavity treatment targets the purity of the niobium [9, 10]. When SRF cavities are operated at high accelerating fields, the surface starts to warm up due to RF dissipation. Since the BCS resistance increases exponentially with temperature, the heat needs to be conducted away to prevent thermal runaway, which would eventually quench the cavity. Best thermal conductivity of the niobium is achieved by employing high purity material. The residual-resistance ratio RRR that gives the quotient of the resistivity at room temperature and resistivity in normal conducting state extrapolated to absolute zero is a measure of the purity and is usually at 300 for bulk niobium cavities. The BCS resistance of high RRR material, however, is increased compared to a material with lower purity of e.g. $RRR = 13$ [11]. In the last years, it was demonstrated that annealing of the high purity niobium with titanium or nitrogen can bring the BCS resistance in the surface to a minimum without compromising the bulk thermal conductivity [9, 10].

A different approach, that is also used in this thesis, targets the residual resistance and namely the contribution due to trapped magnetic flux. When a perfect superconductor is cooled through the superconducting phase transition, all ambient magnetic field should be expelled by the Meissner effect. However, lattice imperfection and impurities in the real material lead to trapping of the magnetic flux lines. Once the RF field is switched on, the flux lines start to oscillate and to dissipate

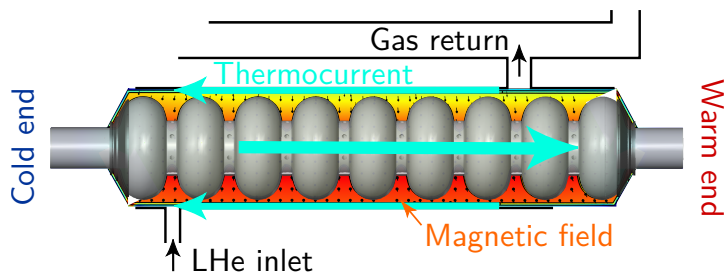
power. Trapped flux is a known cause of residual losses but since most cavities are equipped with one or even two magnetic shields, little research has been focused on it so far. During the early days of SRF, the surface resistance values were limited to the $\mu\Omega$ range [13]. Trapped flux causes $3.5 \text{ n}\Omega$ per μT , as a rule of thumb for TESLA cavities, and hence was a minor cause of dissipation. However, with the progress of SRF technology more and more causes of dissipation were eliminated and trapped flux became more conspicuous. The last years have drawn even more attention to trapped flux because it emerged that the very promising annealing of niobium with nitrogen (so-called N-doping), that helps with R_{BCS} , can increase the susceptibility to trapped flux by almost a factor of 10 [12]. Its positive effect can therefore be canceled or even inverted by only a small amount of trapped flux. Figure 1.2 shows the BCS resistance and the sensitivity to trapped flux as a function of electron mean free path, which is a measure of material purity. The range covered by N-doped cavities treated with various annealing temperatures and durations is marked yellow. The figure illustrates how the minimum in BCS resistance and the maximum in Sensitivity to trapped flux almost coincide. Nitrogen annealing is applied to the SRF cavities of LCLS-II hence these findings have a major project impact. This unanticipated side effect demonstrates further that, though the cryo costs provide a motivation for research on trapped flux, the topic is per se of fundamental interest.

Trapped Flux in a Horizontal Test Assembly

In the past, losses due to trapped flux were often discussed in a narrow frame. It was assumed that any magnetic field that is present in vicinity to a cavity during superconducting phase transition will cause dissipation proportional to its amplitude during operation. This simplified model is sufficient for many purposes. However, in the context of high- Q cavities, where every $\text{n}\Omega$ counts, it is necessary to include all effects involved in flux trapping in the description. For one, not all magnetic field leads to dissipation. Only the magnetic field that gets trapped inside the material at the RF surface during the superconducting phase transition will contribute to the RF losses. For a thorough understanding one must even go further and evaluate the origin of the magnetic field.

Experiments in module-like test stands have revealed that a cavity exhibits a spread in residual resistance when cooled down in different ways [14, 15], even though neither the magnetic shield nor anything else was changed in the setup. In vertical test, no similar effect had been observed before. The best horizontal results matched the vertical tests but the studies indicated that the quality factor can significantly

Figure 1.3: Magnetic field inside the cavity-tank system. The liquid helium is supplied from the bottom left. The arising temperature difference drives a thermocurrent and a magnetic field establishes.



decrease between vertical and horizontal testing or between different horizontal tests, just due to the cooling procedure. Since a horizontal test is much closer to accelerator operation, this observation raised concerns.

For example, one cavity tested at HZB exhibited R_{res} values of 6.4 n Ω and 13.6 n Ω for two different cool down procedures from room temperature to 1.8 K in a horizontal test. That translates to a 50 % increase in refrigeration power. Possible causes like a change in the efficacy of the magnetic shielding or in surface adsorbates were ruled out [16] leaving a change in trapped magnetic flux as the only remaining explanation.

The observations pose the question whether the horizontal test setup carries properties that promote trapped flux. One fundamental difference between vertical and horizontal testing lies in the way that the liquid Helium (LHe) is provided. In a vertical test, the cavity hangs in a bath of LHe. For the horizontal test, however, it is welded into a LHe tank. Thereby, a thermocouple is created because the tank is fabricated from titanium and the cavity from niobium. Large temperature differences can occur in the system during the cooldown and the non-uniform temperature distribution translates into a thermocurrent with an associated magnetic field that will result in additional R_{res} if trapped during the superconducting phase transition. Figure 1.3 shows a sketch of the effect. The detailed investigation of it is the main task of this thesis along with the question how flux trapping in general can be minimized or even completely avoided in SRF cavities.

Thermoelectrically Generated Magnet Field

Chapter 3 of this thesis presents an experimental study, which shows how the losses in a cavity in a horizontal test assembly correlate with large temperature gradients in the system. The findings are a strong indication of a thermoelectric contribution to the residual resistance. However, the temperature difference does not directly translate into losses. Several intermediate steps are involved and for a clear identification of the thermoelectric effect as the cause of the increased dissipation all steps in the line of argument must be tracked and several open questions need answers. The

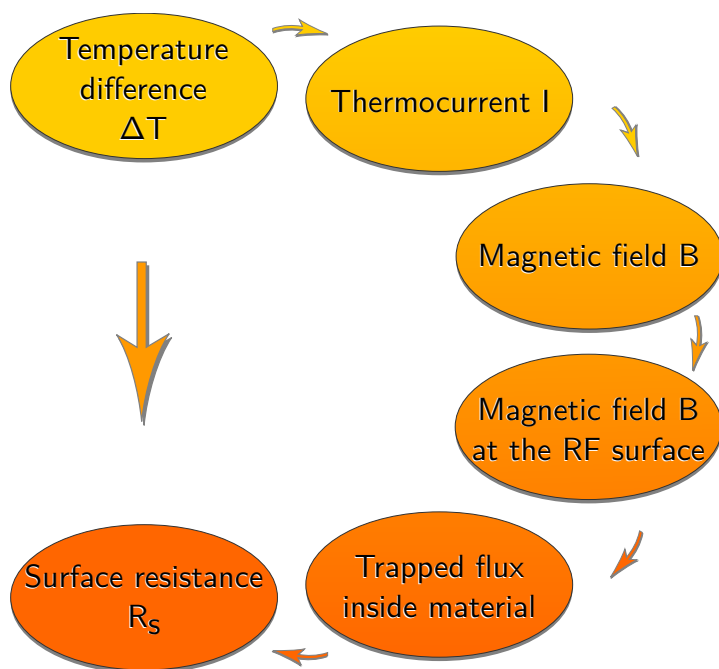


Figure 1.4: Line of argument: In order to prove the thermocurrent hypothesis we need to understand the thermocurrent in the cavity-tank system, the generated magnetic field, especially at the RF surface and finally we must evaluate how much of the generated field gets trapped during the phase transition.

steps are listed in Figure 1.4 and addressed in Chapter 4. Starting from the known temperature difference between the cavity ends, the thermocurrent in the system is evaluated. Here, we find the first open question: The material parameter that connects temperature gradient and electric voltage is called Seebeck coefficient S . For niobium and titanium, the S values at cryogenic temperatures had to be measured. Sections 4.1 and 4.2 present the results.

The next step is to understand the generated magnetic field distribution in the cavity-tank system, especially at the RF surface. Here, we find the second open question: The cavity-tank system is cylindrically symmetrical and by Ampère’s Law no magnetic field should reach in inner surface of the cavity. However, as demonstrated by numerical simulations in Section 4.3, the mechanic symmetry is broken by an additional bottom-to-top temperature gradient, which causes electric asymmetry.

The final question is whether the magnetic field gets trapped or expelled during the superconducting phase transition. Only flux that is trapped inside the material will contribute to RF dissipation. In Section 4.4, a direct measurement of the magnetic field inside an SRF cavity during cooldown is presented. Thereby, the loop from temperature difference all the way to surface resistance is closed.

In addition, Chapter 5 addresses the question under which conditions the magnetic field present during the phase transition is trapped or expelled in a more general context. Two specific questions are targeted with studies on samples utilizing fluxgate magnetometers and magneto-optical imaging.

Chapter 4 with the focus on thermocurrents and Chapter 5 with the focus on flux expulsion are closed by discussions in Sections 4.5 and 5.4. Main conclusions are drawn and an outlook is given, both in Chapter 6. A suitable cooldown procedure for high- Q cavities in an accelerator module is suggested and an impetus for future research is provided.

In order to establish common ground before the presentation of measurement results, Chapter 2 will introduce some basic principles. Section 2.1 will clarify the context in which cavities are used, followed by an introduction to the general and the RF properties of superconductors with the focus on niobium in Section 2.2. The process of flux trapping will be described in Section 2.3 and the thermoelectric effect as an origin of magnetic field will be discussed in Section 2.4. Section 2.5 will close the basics chapter with a summary of the experimental methods used to measure temperature and magnetic field in the cryogenic environment as well as an explanation how the cavity figures of merit that characterize the RF performance are obtained.

Main results of the thesis have been published in References [17], [18], [19] and [20].

Chapter 2

Basic Principles

The main subject of this thesis concerns the RF performance improvement of superconducting cavities for particle acceleration. This chapter will provide the necessary basics, which a reader needs to understand the later presented studies and to follow the line of argument in Figure 1.4.

2.1 RF Cavities for Particle Acceleration

The purpose of a particle accelerator is, as its name implies, to accelerate particles. Energy must be transferred to a particle beam. To achieve that, the electrons, protons or ions are exposed to an electric field and by passing it they gain energy. The voltage that creates the electric field cannot be increased arbitrarily. Therefore, AC systems were developed, where each particle passes the same voltage several times and hence the energy gain is multiplied by the number of passes. Figure 2.1 shows a so-called TESLA-type cavity [6] with nine cells that is fabricated from niobium and operates at 1.3 GHz.



Figure 2.1: A TESLA-type cavity, fabricated from niobium, operating frequency 1.3 GHz (Courtesy FG-ISRF, HZB).

2.1.1 RF Resonators

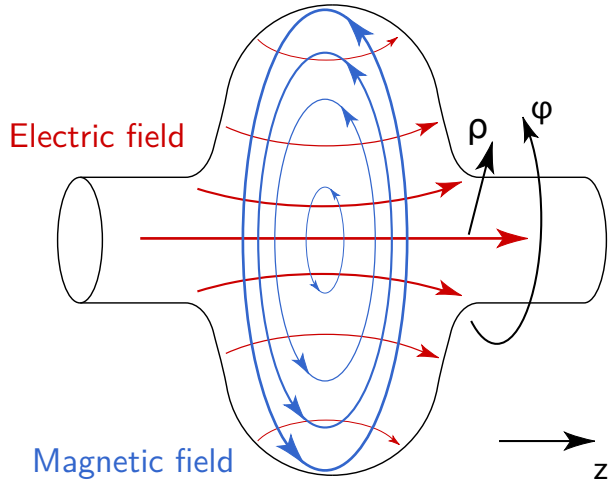
A cavity stores electromagnetic energy and provides the accelerating electric field. Relevant frequencies range from a few kHz up to the GHz region. The following sections will explain the AC properties of a cavity along the lines of Reference [21].

The electromagnetic field inside an cavity is the solution of the wave equation

$$\left(\nabla^2 - \frac{1}{c} \frac{\partial^2}{\partial t^2} \right) \begin{Bmatrix} \mathbf{E} \\ \mathbf{H} \end{Bmatrix} = 0 \quad (2.1)$$

with the boundary conditions $\hat{n} \times \mathbf{E} = 0$ and $\hat{n} \cdot \mathbf{H} = 0$, where \hat{n} is the unit vector normal to the surface. Since a resonant cavity is cylindrically symmetrical, all solutions to Equation 2.1 can be separated in two families based on the direction of the electric and magnetic field: TE_{mnp} modes with only transverse electric field and TM_{mnp} modes with only transverse magnetic field and a longitudinal component of the electric field, which is used for particle acceleration. The indices m , n , and p denote the number of nodes in the ϕ , ρ and z directions in cylindrical coordinates. The fundamental accelerating mode is the TM_{010} mode. Figure 2.2 shows a sketch of the electric and magnetic field in TM_{010} mode in a TESLA-like shape. Other modes can be used for e.g. particle deflection.

Figure 2.2: A sketch of the electric and magnetic field of the fundamental TM_{010} mode, which is used for particle acceleration. Displayed is a one cell cavity of a TESLA-like shape.



2.1.2 Figures of Merit

The properties of different cavity shapes, materials and modes can be compared via a number of figures of merit, which will be introduced in the next section following Reference [21].

The accelerating electric field E_{acc} is defined as the ratio of the accelerating voltage V_c that is obtained by integrating electric field along the particle trajectory z through the cavity, divided by the length of the cavity L

$$E_{\text{acc}} = \frac{V_c}{L} = \frac{1}{L} \left| \int_0^L E_z(\rho = 0, z) e^{i\omega_0 z/c} dz \right| \quad (2.2)$$

with ω_0 being the resonance frequency. E_{acc} gives information on how much energy can be provided to a particle beam per unit length. A very good superconducting cavity for $\beta = v/c = 1$ achieves a gradient about 40 MV m^{-1} .

The second figure of merit that is of importance in this thesis is the unloaded quality factor of the cavity Q_0 . It is defined as the ratio of the stored energy divided by the power dissipated in one RF period

$$Q_0 = \frac{\omega_0 U}{P_{\text{diss}}} = \frac{\omega_0 \mu_0 \int_V |\mathbf{H}|^2 dV}{\int_S R_s |\mathbf{H}|^2 da}. \quad (2.3)$$

U is the energy stored within the cavity's volume V and P_{diss} is the power dissipated as heat in its wall. S is the inner surface of the cavity and μ_0 is the vacuum permeability. U and P_{diss} are given by

$$U = \frac{1}{2} \mu_0 \int_V |\mathbf{H}|^2 dV, \quad (2.4)$$

$$P_{\text{diss}} = \frac{1}{2} \int_S R_s |\mathbf{H}|^2 da. \quad (2.5)$$

Third, assuming that the surface resistance is uniform over the cavity surface and does not depend on the amplitude of the applied field, which is usually valid at low fields, a geometry factor G can be defined. It provides a direct relation between the quality factor Q_0 and the surface resistance R_s

$$G = \frac{\omega_0 \mu_0 \int_V |\mathbf{H}|^2 dV}{\int_S |\mathbf{H}|^2 da} = Q_0 R_s. \quad (2.6)$$

G depends only on the cavity shape but not its size and is obtained from numerical simulations. R_s is, in the end, the material property that must be evaluated to find ways for cavity performance improvement. All results that will be presented in Chapter 3 originate from RF measurements of Q_0 as a function of E_{acc} and temperature that are converted to R_s by the use of G . The experimental setup for the RF tests and the underlying equations are explained in Section 2.5.2.

2.2 RF Superconductivity

Superconductors have several outstanding features. One is that they have very low, for DC currents even zero, electrical resistance. A superconducting cavity dissipates orders of magnitude less power than a normal conducting (nc) one and even though a superconducting (sc) cavity has to be operated at cryogenic temperatures, applying SRF technology can still be advantageous. Several important benefits were already discussed in the introduction. Therefore, this section will be confined to one example: A superconducting cavity can accelerate high beam currents in continuous wave (CW) operation at high gradients. In a normal conducting cavity this combination would produce losses high enough to melt the cavity walls.

The majority of recent accelerator projects relies on the advantages of SRF technology e.g. both projects at HZB (bERLinPro and BESSY-VSR) and the light sources European XFEL at DESY and the LCLS-II at SLAC, which are currently under construction. Apart from electron accelerators also proton and ion machines use SRF technology, for example the European spallation source ESS in Lund, the LHC at CERN and its proposed successor FCC, as well as HIE-ISOLDE (also CERN) and FRIB (Michigan State University).

2.2.1 The Origin of Superconductivity

The main goal of this thesis is to reduce the RF dissipation in superconducting niobium thus it must be explained how the surface resistance is described, calculated and measured for a superconductor under a high frequency electromagnetic field. We will start with the general properties of superconductors.

Cooper Pairing

The microscopic origin of superconductivity was first described by Bardeen, Cooper and Schrieffer in the BCS theory [22]. They developed a description of superconductivity based on the Cooper pairing mechanism. A Cooper pair consists of two electrons with opposite momentum that are bound by a phonon, a quantized lattice vibration. The pair has a total spin of 0 or in some cases 1. While electrons are fermions that underlie the Fermi-Dirac statistics, Cooper pairs are composite bosons that underlie the Bose-Einstein statistics. Hence, all Cooper pairs in a superconductor have the same quantum mechanical ground state, which alters the density of states below its transition temperature T_c . Several outstanding properties result thereof. The most prominent ones are the vanishing of the DC resistance, flux quantization and ideal

diamagnetism. The following sections will summarize the theoretical description and some phenomenological features along the lines of Reference [23].

The Two-Fluid Model

A convenient starting point for the review of the superconductor properties is the charge carriers density. At T_c , the first conduction electrons form Cooper pairs. The density of Cooper pairs starts to increase as the temperature is lowered until all conduction electrons are bound in pairs at 0 K. The number of Cooper pairs n_s can be described as

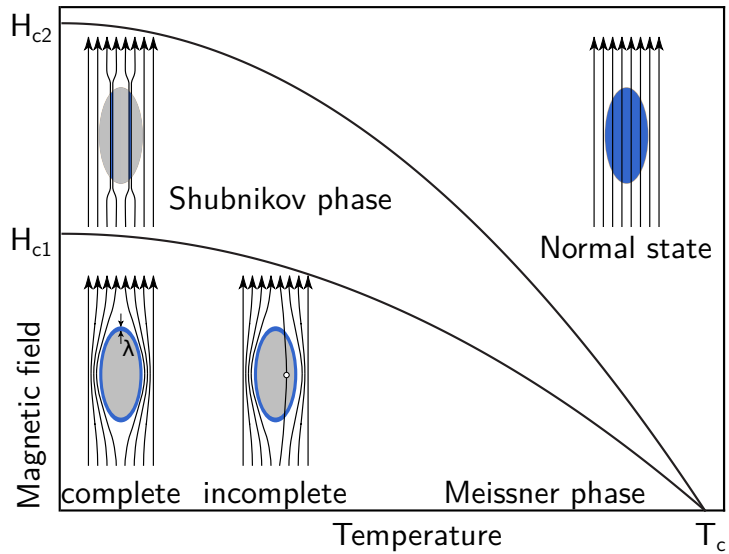
$$n_s = n_0(1 - t^4), \quad (2.7)$$

with $t = T/T_c$ and $n_0 = n_s + n_n$. The number of normal electrons n_n decreases accordingly. The applied accelerating RF field acts on both, the superconducting and the normal conducting electrons. The overall response of the superconductor can therefore be described as a superposition of the responses of two fluids to the RF field: a superconducting channel and a normal conducting, lossy channel. From this picture it becomes apparent that the surface resistance of a superconductor must have a strong dependence on two parameters. First, the temperature because it defines the number of normal and superconducting electrons and second, the frequency because it influences the fraction of current that each channel carries. Electrons and Cooper pairs have a mass and therefore inertia. While in the DC case the whole current is carried in the superconducting channel and the normal conducting electrons are shielded from the electric field, an AC field cannot be shielded instantly by a supercurrent. The normal conducting electrons start to participate in the oscillation and with increasing frequency the lossy, normal conducting channel will contribute increasingly.

Density of States and the Energy Gap

The formation of Cooper pairs also influences the density of states of the material. No states exist anymore at and close to the Fermi level due to the bosonic nature of the Cooper pairs. They are described by the a common condensed-state wave function. No Cooper pair can be excited to a different state than the other Cooper pairs. The only possible excitation requires to break up a Cooper pair into two electrons, which requires a minimum energy that is the binding energy of the pair. As a consequence, an energy gap of $2 \Delta(T)$ opens in the density of states at the Fermi level.

Figure 2.3: The critical fields of a type-II superconductor. Above H_{c2} , the material is in the normal state. Below H_{c2} , the magnetic field is quantized and below H_{c1} , the magnetic field is expelled. Pinning sites (dislocations or normal conducting precipitates) may hinder the expulsion. They lead to flux pinning and hence an incomplete Meissner phase.



2.2.2 Phenomenology and Theoretical Descriptions

Another remarkable difference, beside the disappearance of DC resistance, is the response to an external magnetic field.

Meissner Effect and Critical Magnetic Field

Niobium exhibits superconductivity below $T_c \approx 9.2$ K in two different states. In the Meissner state, experiments show that a small magnetic field, present in the initially normal sample, is expelled when the material turns superconducting (Meissner effect). Furthermore, a magnetic field, which is switched on after the phase transition, is hindered to penetrate the material. A superconductor hence is a perfect diamagnet: a flux expelling material. This feature is different from a “normal” perfect conductor, which can be called a flux conserving material. The difference becomes apparent when we compare the cooldown through T_c in the presence of a magnetic field (“field cooled”) with a cooldown in no magnetic field (“zero field cooled”) with the field being turned on after transition. A perfect conductor will preserve either state during transition. A superconductor, however, will expel any field and in both cases lead to the same final state where no magnetic field penetrates the bulk material. Figure 2.3 illustrates the field distributions in a superconductor. Furthermore, it shows that the Meissner state collapses not only if T_c is exceeded but also if a critical magnetic field value H_{c1} is reached. At H_{c1} , the external magnetic field starts to enter the material in the quantized form of flux lines. Each line contains one elementary flux quantum ϕ_0 (Shubnikov phase). The area in between the flux lines remains superconducting while the core of each flux line is normal conducting. If the magnetic field is increased

further above the second critical value H_{c2} , the superconductivity breaks down and the field penetrates all the material. A sketch of the three states together with the associated magnetic field distributions and the critical limits is given in the figure. Both critical fields are temperature dependent and can be approximated as

$$H_c(T) \approx H_c(0)(1 - t^2). \quad (2.8)$$

Superconductors are classified in two types depending on their response to an external magnetic field. Niobium is counted as type-II, as any superconductor that exhibits a Shubnikov phase. Type-I superconductors, in contrast, can only exist in the Meissner state. Their superconductivity breaks down at the critical field H_c , an example is lead.

The London Equations: Theory for Perfect Conductivity and the Meissner Effect

In 1935, when Cooper pairs were still unknown, the brothers F. and H. London developed a phenomenological description to explain the Meissner effect. They started at two equations for the current density \mathbf{J}_s and the microscopic electric field \mathbf{E} and magnetic field \mathbf{B}

$$\frac{\partial}{\partial t} \mathbf{J}_s = \frac{n_s q^2}{m} \mathbf{E} \quad (2.9)$$

$$\nabla \times \mathbf{J}_s = -\frac{n_s q^2}{m} \mathbf{B} \quad (2.10)$$

with n_s , the number of superconducting particles that varies continuously from zero at T_c to the maximum value at 0 K, m is the mass of the charge carriers and q their charge. Since a superconducting Cooper pair consists of two electrons, q is twice the elementary charge e . The first London equation describes perfect conductivity and the second London equation can be combined with the Maxwell equation $\nabla \times \mathbf{B} = \mu_0 \mathbf{J}$ yielding

$$\nabla^2 \mathbf{B} = \frac{\mu_0 n_s q^2}{m} \mathbf{B}. \quad (2.11)$$

The solution of the equation leads to the description of the Meissner effect. The magnetic field is exponentially screened from the interior of the superconductor with a penetration depth λ_L , the London penetration depth. For a flat boundary between free space and superconductor parallel to x and the z axis normal to the boundary

we obtain:

$$B_x(z) = B_0 e^{-z/\lambda_L} \quad (2.12)$$

$$\text{with } \lambda_L = \left(\frac{m}{\mu_0 n_s q^2} \right)^{1/2} \quad (2.13)$$

The Ginzburg-Landau Theory: Deriving the Origin of the Shubnikov Phase

In parallel to Bardeen, Cooper and Schrieffer, the Soviet physicists Ginzburg and Landau developed an alternative approach to describe superconductivity, which was later demonstrated to be a limiting form of the BCS theory. They introduced a complex pseudowave-function ψ as an order parameter that describes the superconducting particles. Physically, it represents the wave function of the Cooper pairs' center-of-mass motion. The quantity $|\psi|^2$ can be interpreted as the *local* density of superconducting charge carriers n_s . The formalism was able to treat features beyond the scope of the London theory as the coexistence of magnetic field and superconductivity e.g. in the intermediate state where due to the geometry of the sample superconducting and normal conducting areas coexist at $H \approx H_c$. Furthermore, it lead to the first theoretical description of the Shubnikov phase by Abrikosov. The Ginzburg-Landau theory starts at the free-energy density f and expands it in $|\psi|^2$. In the absence of fields and gradients, the difference between the normal state f_n and the superconducting state f_s becomes

$$f_s - f_n = \alpha |\psi|^2 + \frac{1}{2} \beta |\psi|^4 \quad (2.14)$$

with the expansion coefficients $\alpha(T)$ and $\beta(T)$. Subsequently, the theory introduces a characteristic length, called the GL coherence length ξ_{GL}

$$\xi_{\text{GL}}(T) = \frac{\hbar}{|2m\alpha(T)|^{1/2}} \quad (2.15)$$

where \hbar is the Planck constant. The GL coherence length characterizes the distance over which $\psi(\mathbf{r})$ can vary without energy increase. It is a function of temperature. In a pure superconductor far below T_c the GL coherence length can be approximated by the Pippard coherence length. Pippard proposed a nonlocal generalization of the London equation and argued that only electrons within kT_c of the Fermi energy can play a major role in a phenomenon that sets in at T_c . Their momentum range is $\Delta p = kT_c/v_F$. The uncertainty-principle yields

$$\xi = a \frac{\hbar v_F}{kT_c} \quad (2.16)$$

where v_F is the Fermi velocity, k is the Boltzmann constant and a is a numerical constant. BCS later confirmed the equation and determined $a = 0.18$. ξ_{GL} can be thought to represent the smallest size of a wave packet that the superconducting charge carriers can form. For temperatures close to T_c , ξ_{GL} diverges.

The ratio of the characteristic lengths λ_L/ξ_{GL} defines the GL parameter κ that is approximately temperature independent. It gives information on the surface energy associated with a domain wall between superconducting and normal conducting domains. For a small κ value, the superconductor has a positive wall energy. Energy is required to increase the total surface of any domain interface. Type-I superconductors exhibit small κ values. Type-II superconductors feature large κ values. Here, the wall energy is negative causing domains to subdivide until the microscopic limit of ξ_{GL} is reached. Thereby, the ambient field can exist within the material arranged in locally separated flux lines: the Shubnikov phase establishes. The crossover between the two regimes is at $\kappa = 1/\sqrt{2}$. The number was found numerically by Ginzburg and Landau.

Characteristic Parameters of Niobium

To this point, several theoretical concepts were introduced. They provide the basics for the following sections hence here a brief summary of the important characteristic parameters together with the niobium values (Table 2.1).

Table 2.1: Material parameters for niobium [24].

Parameter	Unit	Description	Nb
T_c	K	transition temperature	9.25
$\lambda_L(0)$	nm	London penetration depth (at 0 K)	32
$\xi_{GL}(0)$	nm	Ginzburg-Landau coherence length (at 0 K)	39
$2\Delta/kT_c$	1	energy gap	3.5...3.85

2.2.3 AC Losses in Superconductors

Dependence on Temperature and Frequency in Theory

After the general description of superconductivity, we can now turn to the more specific question of RF dissipation in superconducting material along the lines of Reference [24]. As explained above, not all conduction electrons form Cooper pairs at temperatures above 0 K. Hence, both contributions to RF dissipation, normal

conducting electrons and Cooper pairs, must be evaluated according to the two fluid model. The first London equation (Equation 2.9) can be extended to

$$\frac{\partial \mathbf{J}}{\partial t} = \frac{n_s q^2}{m} \mathbf{E} + \sigma_n \frac{\partial \mathbf{E}}{\partial t} \quad (2.17)$$

where $\sigma_n = \sigma \cdot n_n / n_0$ is the electrical conductivity σ of the metal in the normal state just above T_c multiplied by the number of normal electrons n_n and divided by the sum of all charge carriers n_0 . The solution for Equation 2.17, again, yields a penetration depth λ . If the first term on the right-hand side dominates, λ can be approximated by the London penetration depth. Including the temperature dependence of the charge carrier density from the two fluid model we obtain

$$\lambda(T) = \lambda_L(T) = \lambda_L(0)[1 - t^4]^{-1/2}, \quad (2.18)$$

which has proven to be a good approximation for $t > 0.6$. To obtain a result that is valid for low temperatures, the BCS density of state must be included. The result is valid for $t < 0.5$ [24]

$$\frac{\lambda(T) - \lambda(0)}{\lambda(0)} = \sqrt{\frac{\pi \Delta}{2kT}} \exp(-\Delta/kT), \quad (2.19)$$

which contains the characteristic exponential decrease with temperature that originates in the energy gap and will appear in the calculation of the surface resistance as well. The latter can be deduced by evaluating photon absorption and emission based on the BCS density of states. The dissipated power is given by the transition rate multiplied by the energy of the absorbed photon and by the matrix element integrated over available quasi-particle states and photons. The matrix element includes the momentum and energy properties of the quasi-particles and of the photons (for details see Reference [24]). Finally, the surface resistance is proportional to the dissipated power and for $t < 0.5$, $\hbar\omega \ll kT$, $\hbar\omega \ll \Delta$

$$R_s \propto \frac{\mu_0^2 \omega^2 \lambda^3 \sigma \Delta}{kT} \ln \left(\frac{2.246kT}{\hbar\omega} \right) \exp(-\Delta/kT) \quad (2.20)$$

is obtained [25]. In this microscopic treatment, the normal fluid that accounts for dissipation in the two fluid model, is represented by thermally excited quasi-particles. Based on the resulting description, a fit function for experimental data can be designed.

A Fit Function for Experimental Data

When SRF research started more than 60 years ago, most of the theoretical findings described in the previous sections were still undiscovered and anyone trying to improve RF performance had to establish a model to describe the RF losses. Pippard was, for example, one of the first to propose a fit function for surface resistance versus temperature [26], which later evolved to today's understanding of T -dependent losses, R_{BCS} . Some time later, Fawcett and Kaplan described a derivation of the T -dependent function at low temperatures [27]. The surface resistance was not decreasing with temperature anymore but reached a constant minimum value, the residual resistance R_{res} . Based on Equation 2.20, a reliable semi-empirical fit function for the surface resistance measured at a fixed accelerating field has been established [25]

$$R_s = \left(\frac{af^2}{T} \right) \exp \left(-\frac{bT_c}{T} \right) + R_{\text{res}}. \quad (2.21)$$

The first fit parameter a depends on the purity of the material and changes with the surface treatment. For bulk niobium, the first term is usually in the range of some $10 \mu\Omega$. The second term bT_c incorporates the energy gap with the fit parameter b that is in the range of 1.75 to 1.93 based on the data in Table 2.1. The third fit parameter is the residual resistance R_{res} that would disappear for the best cavities but usually amounts to a few $\text{n}\Omega$.

RF Penetration Depth and Material Purity

After the experimental fit function was discussed, one last topic needs to be addressed. The penetration depth λ in Equation 2.20 is not the London penetration depth but the RF penetration depth. For normal conductors it is described by the skin effect or in case of high purity materials by the anomalous skin effect. Pippard proposed a definition of RF penetration in superconductors analogous to the anomalous skin effect where a general ξ ($1/\xi = 1/\xi_{\text{GL}} + 1/l$) plays the role of the electron mean free path l [28]. The mean free path is the average distance that an electron can travel between collisions with scattering centers. The dependence of λ on l can be approximated as

$$\lambda \approx \lambda_L (1 + \xi_{\text{GL}}/l)^{1/2} \quad (2.22)$$

and the surface resistance hence depends on l as

$$R_s \propto \left(1 + \frac{\xi_{\text{GL}}}{l} \right)^{3/2} l. \quad (2.23)$$

Two limits for RF dissipation can be defined. In the “clean” limit, l is much larger than ξ_{GL} and R_s increases linear with l . In the “dirty” limit, l is smaller than ξ_{GL} and R_s becomes proportional to $(1/l)^{1/2}$. The optimum purity is hence at $l = \xi_{\text{GL}}/2$, which is around 20 nm for niobium close to 0 K. The dependence of the resistance on the mean free path was already displayed in Figure 1.2 in the introduction.

2.2.4 Knobs for the Reduction of RF Dissipation

After understanding the physics of RF dissipation, we can now turn to reducing it with focus on resonators for electrons with $\beta = v/c = 1$. The most obvious approach would be to reduce the operating temperature, which would exponentially decrease R_s . However, the efficiency of the cryoplant is decreasing with temperature as well. The optimum operation temperature to balance losses and wall-plug power is within the 1.8 to 2 K window. A further reduction of temperature would increase the needed wall-plug power again.

Next, one could consider reducing the operating frequency, which would decrease the resistance according to a square law. This, however, would enlarge the resonators and the overall accelerator. The real-estate gradient would be reduced, which is lethal for projects with many cavities like high-energy LINACs. The optimum for the frequency has emerged to be around 1 GHz.

Since frequency and temperature are more or less fixed, the improvement of R_s can be attained by changing material properties to optimize R_{BCS} (the parameters a and b in Equation 2.21). Recently established annealing techniques [9, 10] change the purity of the niobium in a surface layer and thereby achieve a decrease in R_{BCS} . Several other approaches target the residual losses. Investigations revealed that the main contribution to it is trapped magnetic flux. Niobium is a type-II superconductor though its κ is close to the crossover. Hence, when it is cooled through phase transition in an ambient magnetic field, it first enters the Shubnikov phase. Flux lines form. When the temperature is further lowered, the material enters the Meissner state and, in a perfect superconductor, all flux is expelled. In real materials, imperfections in the material can pin flux lines at favorable locations and thereby hinder the expulsion. The flux gets trapped and causes additional RF dissipation. The next section will explain the physics of flux lines, flux pinning and the calculation of losses due to flux line oscillation under RF field.

2.3 Trapped Magnetic Flux

But what apparently happens is that in type II superconductors there are small regions containing magnetic flux which are essentially in the normal state. Direct currents flow around these regions and thus suffer no losses, but high frequency currents cannot bypass these regions, and power is dissipated. We have tried niobium and certain other materials and, except for one experiment, all the tests I know of have been poorer with type II superconductors.

William M. Fairbank, Stanford University, 1966 in [29]

In the early days of SRF cavities were all fabricated from lead, a type-I superconductor. Lead has a T_c of 7.2K and a critical field of 80mT. A few MV m^{-1} accelerating gradient and reasonably high Q values up to the 10^9 range were demonstrated [29]. The results however did not meet the high expectations originating from theoretical predictions and hence the community turned its interest towards type-II superconductors. The first investigations with the new materials yielded already the first problems. As the quotation of W. Fairbanks given above shows, one main challenge was trapped magnetic flux and it remains so up to today.

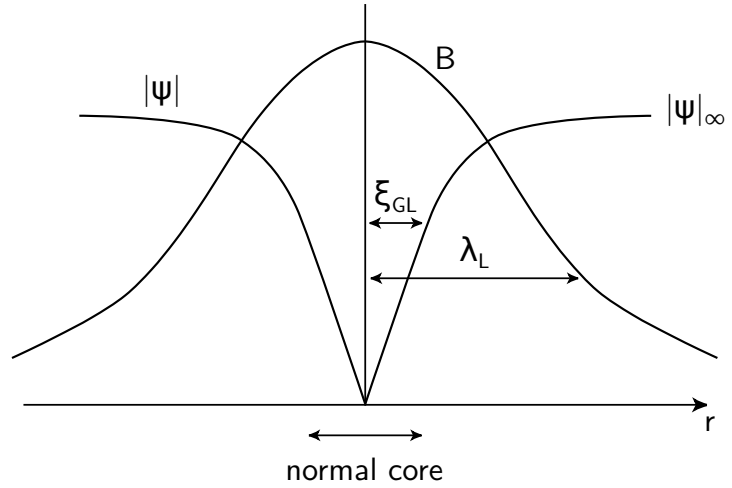
2.3.1 The Structure of a Flux Line

When we cool a superconductor at finite ambient magnetic field, it first enters the Shubnikov phase (see Figure 2.3). The magnetic field is now quantized in the form of flux lines and the parameters of the superconductor are not constant in this area. In the center of the flux line, the material is normal conducting and the magnetic flux density B has its maximum. The order parameter $|\psi|^2$ is zero. With increasing distance to the center r , the number of Cooper pairs $n_s = |\psi|^2$ increases and B decreases. Figure 2.4 shows a sketch of the spatial variation in B and indicates ξ_{GL} and λ_L . B and ψ can also be calculated as functions of r . Reference [30] contains a detailed derivation that will, in excerpts, be presented in the following.

For a typical type-II superconductor, the London theory can be used but Equation 2.10 must be modified. Assuming a very narrow area of the core and a magnetic field applied in z direction with \mathbf{i}_z being the unit vector in that direction, the magnetic structure in the region outside it can be described by the modified London equation

$$\lambda_L^2 \nabla \times \nabla \times \mathbf{B} + \mathbf{B} = \mathbf{i}_z \phi_0 \delta(\mathbf{r}). \quad (2.24)$$

Figure 2.4: Spatial variations of the order parameter and the magnetic flux density in a flux line in case of a superconductor with $\kappa \gg 1$ [30].



$\delta(\mathbf{r})$ is a two-dimensional delta function. The coefficient ϕ_0 comes from the requirement that the total amount of magnetic flux of the flux line is ϕ_0 , one quantum of magnetic field. The solution of Equation 2.24 is given by

$$B(r) = \frac{\phi_0}{2\pi\lambda_L^2} K_0\left(\frac{r}{\lambda_L}\right) \quad (2.25)$$

where K_0 is the modified Bessel function of the zeroth order. Since this function diverges at $r = 0$ but the magnetic flux density should have a finite value, Equation 2.24 is still not correct inside the core region but can be used for approximation of the magnetic flux density outside it.

The flux line is upheld by a current that has only an azimuthal component. The current density is given by

$$J(r) = -\frac{1}{\mu_0} \cdot \frac{\partial B}{\partial r} = \frac{\phi_0}{2\pi\mu_0\lambda_L^3} K_1\left(\frac{r}{\lambda_L}\right) \quad (2.26)$$

where K_1 is the modified Bessel function of the first order. In the region $\xi_{GL} \ll r \ll \lambda_L$ the equation reduces to

$$J(r) = \frac{\phi_0}{2\pi\mu_0\lambda_L^2} \frac{1}{r}. \quad (2.27)$$

Furthermore, ψ is increasing with r and can be approximated by

$$\frac{\psi}{|\psi_\infty|} = g(r) \exp(-i\theta) \quad (2.28)$$

$$\text{with } g(r) \simeq cr \left[1 - \frac{r^2}{8\xi_{GL}^2} \left(1 + \frac{B(0)}{\mu_0 H_{c2}} \right) \right]. \quad (2.29)$$

$|\psi_\infty|$ is the equilibrium value of the order parameter in the superconductor far from the flux line, θ is the azimuthal angle and c is a constant. The function g can be

approximated by a hyperbolic tangent

$$g \simeq \tanh\left(\frac{r}{r_n}\right) \quad (2.30)$$

with r_n being numerically calculated to

$$r_n = \frac{4.16\xi_{\text{GL}}}{\kappa^{-1} + 2.25}. \quad (2.31)$$

For niobium, r_n is in the order of ξ_{GL} (around 40 nm) and exhibits the same temperature dependence.

2.3.2 Flux Pinning

Flux lines interact with each other, they repel each other, and in the Shubnikov phase close to H_{c2} the interaction causes the flux lines to form a regular lattice. In terms of the GL theory, the presence of a magnetic field due to flux lines and the associated spatial variation of ψ must be accounted for. The free energy density in the superconductor f_s is now given by

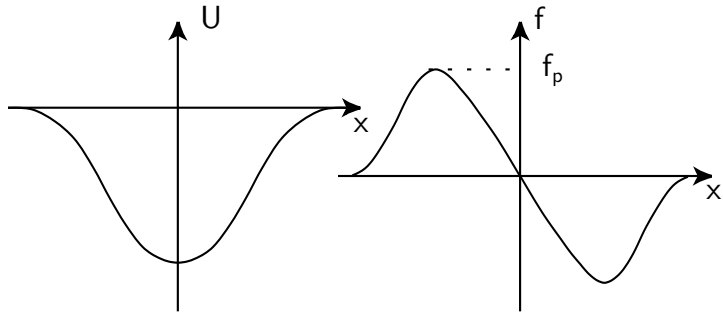
$$f_s = f_n(0) + \alpha|\psi|^2 + \frac{\beta}{2}|\psi|^4 + \frac{1}{2\mu_0}(\nabla \times \mathbf{A})^2 + \frac{1}{2m}|(-i\hbar\nabla + 2e\mathbf{A})\psi|^2 \quad (2.32)$$

where $f_n(0)$ is the free energy density in the normal state in the absence of a magnetic field, m is the mass of a Cooper pair, \mathbf{A} is the vector potential (including magnetic field) and α and β are the coefficients in the expansion of f_s as a power series of $|\psi|^2$. The equation is the more general form of Equation 2.14.

The flux line lattice is distorted by pinning centers like voids, dislocations, grain boundaries, inclusions, etc. The material properties (including T_c , H_c and ξ_{GL}) in a pinning center differ from properties in the surrounding superconducting material. This variation is included in the theory by the expansion coefficients α and β , which now depend on location and consequently the free energy does so, too. The result is a force that pulls flux lines towards locations of lower energy: the pinning force. At lower magnetic fields, the spacing between the flux lines increases until their interaction almost vanishes. The pinning force becomes the dominating force. Here, it is easier to understand why pinning centers are favorable locations for the flux lines:

When a single flux line penetrates the superconductor, the free energy will change simply due to the presence of the magnetic field, as shown in Equation 2.32. Integration over θ and r (in cylindrical coordinates) yields an increase of about $1.55\pi\mu_0 H_c \xi_{\text{GL}}^2$ per unit length [30]. This energy U is required to break up the Cooper pairs in the center of the flux line in order to establish a normal conducting region. U does not

Figure 2.5: Variation in energy U when a flux line passes through a pinning center and the variation of the interaction force $f = \partial U/\partial x$. The elementary pinning force f_p is the maximum value of f [30].



depend on location in a perfect superconductor. However, the presence of pinning centers with different material properties causes a local variation in free energy and hence U will depend on location as well. Figure 2.5 shows the variation of the energy U when a flux line is displaced across a pinning center from left to right. Let us consider a normal conducting precipitate as an example. When a flux line is introduced to the superconductor far away from a pinning center, the energy is increased because energy is needed to break up the Cooper pairs in that region. In the presence of a normal conduction precipitate, however, less energy is needed to introduce a flux line because the precipitate is already normal conducting. U is reduced with respect to the surrounding superconductor as shown in the figure.

The interaction force between a pinning center and a flux line is defined as the spatial gradient of the energy $f = \partial U/\partial x$. It is also displayed in Figure 2.5. The flux line experiences an attractive force when it approaches the pinning center. Once it reached the center, the force vanishes. If the flux line is further displaced, the force changes sign and the flux line is hindered from leaving the pinning center. The elementary pinning force f_p of a small pinning center is defined as the maximum value of the interaction force

$$f_p = \left(-\frac{\partial U}{\partial x} \right)_{\max}. \quad (2.33)$$

For the calculations, the pinning mechanics are classified into condensation energy interaction (including normal precipitates and grain boundaries), elastic interaction, magnetic interaction and kinetic energy interaction according to the associated energy. For derivation of the pinning forces see Reference [30]. Only one example will be shown here: The pinning force of a normal precipitate on the flux line of the length D

$$f_p \simeq 0.430\pi \frac{\xi_{GL} D^2 \mu_0 H_c^2}{a_f} \left(1 - \frac{B}{\mu_0 H_{c2}} \right). \quad (2.34)$$

Based on that equation, a flux line with the length of 1 cm in niobium close to 0 K and at an ambient field of 1 μ T experiences a pinning force of ≈ 3 mN by a small normal conducting precipitate.

For SRF cavities the density of flux lines is low and we can approximate that they barely interact with each other. The flux line spacing a_f ($a_f = (2\phi_0/\sqrt{3}B)^{1/2}$ for a triangular flux line lattice) becomes about $50\ \mu\text{m}$ for $1\ \mu\text{T}$ ambient field, which is very large compared to the penetration depth, coherence length and diameter of the flux lines. The response to a pinning force can therefore be treated individually what simplifies the problem to some extent but even under this relaxed conditions, GL theory gives only rough approximations.

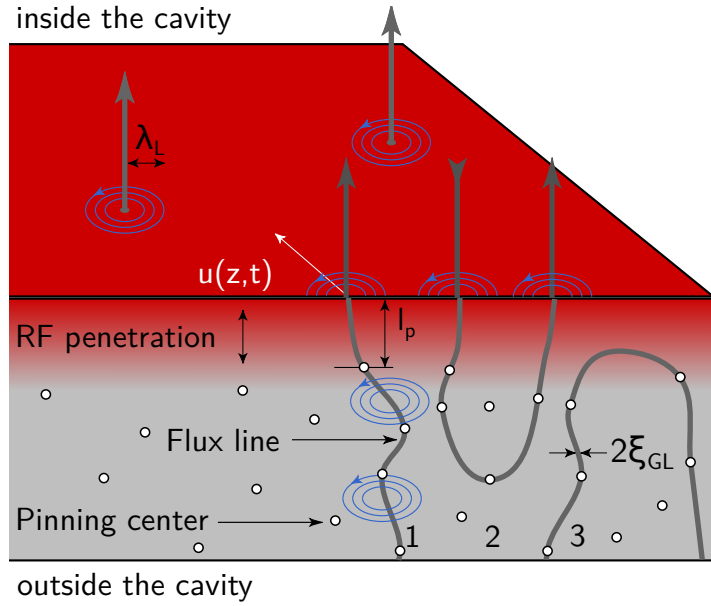
In the more general case the interaction of flux lines can not be neglected. Though elementary pinning is well defined, the actual calculation of the overall pinning force F_p between all pinning centers and the whole flux line lattice is a very complex problem. This so-called “summation problem” is still occupying theorists today. For strong pinning centers, however, we can assume that F_p will be proportional to the number of pinning centers N_p and the elementary pinning force f_p (linear summation)

$$F_p \simeq N_p f_p. \quad (2.35)$$

2.3.3 Losses Due to Trapped Flux

When a superconducting cavity is cooled down for operation, it first passes into the Shubnikov phase and later further into the Meissner state. Here, by definition, all magnetic field should be expelled as explained in Section 2.2.2. However, pinning centers in the niobium prevent expulsion, which causes flux lines to remain in the material even below H_{c1} . The flux lines get trapped. Until a few years ago it was assumed based on Reference [31] that SRF cavities trap close to 100% of the ambient field. Recent research exploits ways to reduce this number, which will be the topic of Chapter 5. A reduction is most desirable because all trapped flux lines dissipate power when exposed to RF fields. The losses depend on material parameters such as the penetration depth and the critical magnetic field as well as the frequency and amplitude of the applied RF field. The ensuing derivations follow Reference [32], where trapped flux lines are regarded as elastic strings that oscillate under an applied RF field. The calculations assume a strong pinning. No flux line is able to leave its pinning site. Furthermore, the penetration depth is approximated by the London penetration depth. For high-purity niobium SRF cavities operated at low temperature these approximations are valid.

Figure 2.6: Trapped flux lines in a sc cavity wall. Possible configurations are (1) flux line going all the way through the material, (2) pinned semiloop at the surface (3) flux line segment crossing the region of the RF field penetration. The RF $H(t)$ penetrates a thickness of λ_L and the flux line segments at the inner surface oscillate. Figure adapted from Reference [32].



The Model of Oscillating Flux Line Strings

Figure 2.6 shows an SRF cavity wall. Flux lines (dark grey strings) are pinned to pinning centers (white dots) and hence trapped in the superconductor. The distance between pinning center and inner cavity surface is labeled l_p . The flux lines are upheld by circular currents (blue circles). The structure of every individual vortex is the one described in Section 2.3.1. The flux lines can be trapped in three different configurations, which are also displayed. A (weak) RF field $H(z, t) = H_p \exp(-z/\lambda_L + i\omega t)$ is applied in parallel to the surface and penetrates the red area.

The equation of motion can be formulated with u being the displacement of the vortex parallel to the surface and z being the coordinate perpendicular to the surface pointing into the material:

$$\eta \frac{du}{dt} = F \exp(-z/\lambda_L + i\omega t) + \hat{\epsilon} \frac{d^2 u}{dz^2} \quad (2.36)$$

The equation has three terms. The right hand side includes the RF driving force that penetrates as deep as λ_L and has the amplitude $F = \phi_0 H_p / \lambda_L$. It is the cause of the flux line oscillation. The second term on the right hand side incorporates the 3D properties of each flux line. They are strings, which can end on the RF surface (1) or form a semiloop with either both ends (2) or no end (3) on the RF surface. The three configurations are displayed in Figure 2.6. In any case, the string nature of the flux lines adds an extra degree of freedom to the system compared to e.g. the equation of motion of a point mass. For explanation purposes, a flux string can be compared to a spring, which exerts a force when its length is changed. This force is

proportional to the deformation of the spring. For the elastic flux line strings, the displacement during oscillation causes a line tension because the string remains fixed at the pinning center at one end. The resulting force is proportional to the second derivative of the displacement u with respect to z . The operator $\hat{\epsilon}$ in Equation 2.36 is a tensor that describes this dispersive flux line tension and thereby accounts for the “elasticity” of the flux line strings. It also includes an anisotropy parameter, which is however not needed for niobium. The solution of u does not include $\hat{\epsilon}$ but its Fourier transform ϵ , which is a constant for isotropic superconductors. Further details are provided in Reference [32].

Finally, the term on the left hand side in Equation 2.36 takes the dissipation into account. The flux lines move in a viscous medium and $\eta = \phi_0 B_{c2} / \rho_n$ is the viscous drag coefficient with the upper critical field $B_{c2} = \phi_0 / 2\pi \xi_{GL}^2$ and the normal-state resistivity ρ_n . At this point we see that the loss mechanism used in the model is the scattering of normal conducting electrons. They exist in the core of the flux line and are exposed to the RF field.

Solution of the Equation of Motion

After understanding all terms of the equation of motion, we can proceed with the search for a solution to describe the flux line displacement u as a function of t and z . Two boundary conditions must be fulfilled: First, it is assumed that the pinning is strong and hence the flux line stays fixed at the pinning center at all times: $u(l_p) = 0$. Second, the flux line is always perpendicular to the surface of the conductor: $du/dz(0) = 0$. Furthermore, only the case is considered where $l_p > \lambda_L$ to show a complete solution. In cases where λ_L exceeds l_p , e.g. in thin films, it must be taken into account that the currents reach flux line segments behind the pinning center. The solution of the equation of motion (Equation 2.36) for the presented constraints is

$$u(z, t) = \frac{H_p \phi_0 \lambda_L}{i\omega \eta \lambda_L^2 - \epsilon} e^{i\omega t} \left[e^{-z/\lambda_L} + \frac{\sinh(q_\omega z)}{q_\omega \lambda_L} - \frac{\cosh(q_\omega z)}{\cosh(q_\omega l_p)} \left(e^{-l_p/\lambda_L} + \frac{\sinh(q_\omega l_p)}{q_\omega \lambda_L} \right) \right]$$

with $q_\omega = (i\eta\omega/\epsilon)^{1/2}$ and $\epsilon = \phi_0 g / 4\pi\mu_0 \lambda_L^2$, g can be used to account for anisotropy in the superconductor and is set to 0.5 for niobium, which is isotropic. The result shows that the displacement is maximum at the surface of the superconductor and decreases along z . The equation is rather confusing therefore Figure 2.7 shows u along z for the segment of a flux line between the pinning center and the surface for typical niobium parameters. Only the position of the center of the flux line is displayed.

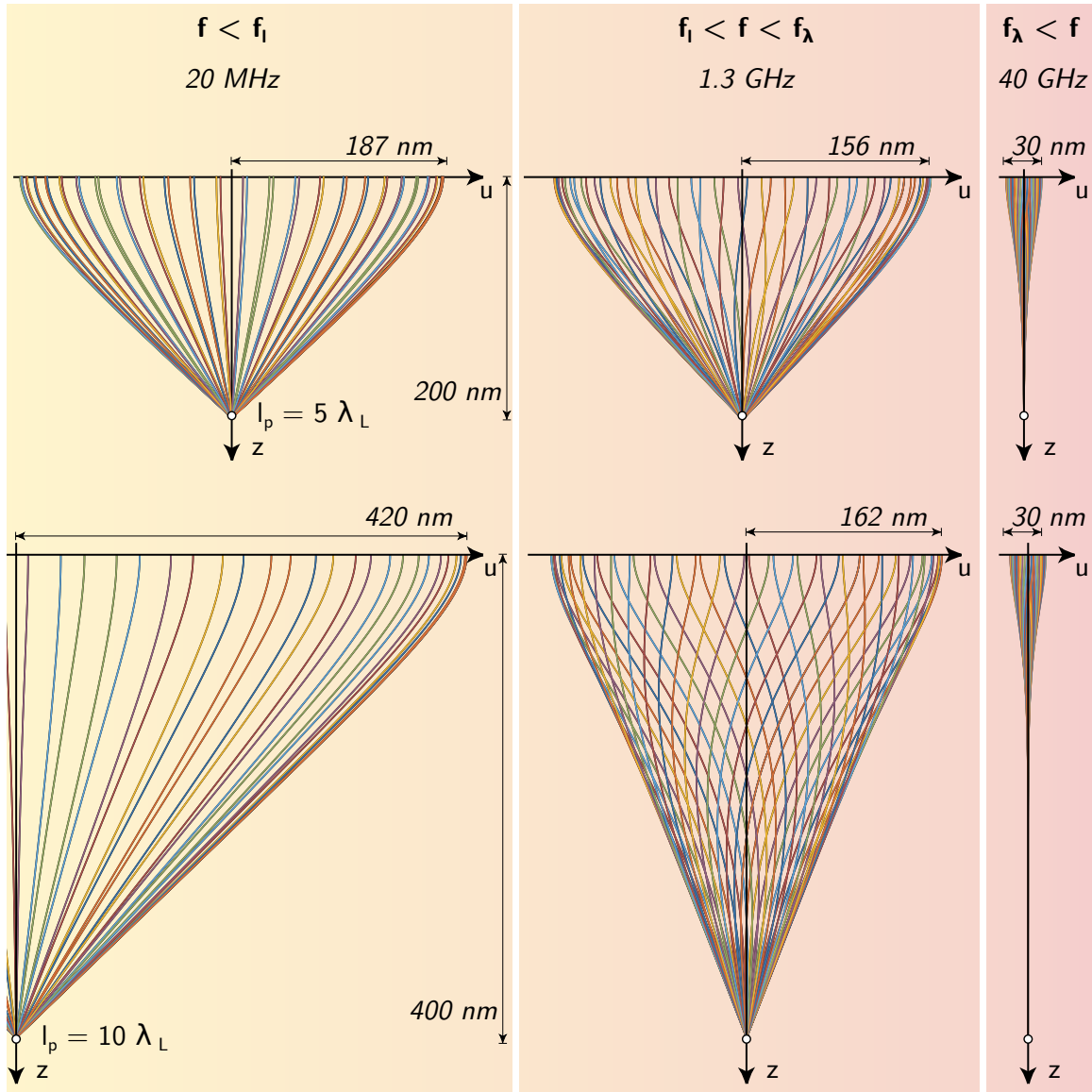


Figure 2.7: Oscillation of a flux line in superconducting niobium at $T \ll T_c$ with $B_p = 60 \text{ mT}$, $\lambda_L = \xi_{GL} = 40 \text{ nm}$, $\rho_n = 10^{-9} \Omega \text{ m}$ and $g = 1/2$. At low frequencies $f < f_l$, the whole flux line segment between the pinning center (white dot) and the surface (u axis) oscillates and the dissipated power P depends on f and l_p . At intermediate frequencies $f_l < f < f_\lambda$, the oscillation is localized in a layer of thickness $1/q_\omega$ and P depends only on f . At high frequencies $f_\lambda < f$, only the tips of the flux line oscillate and P becomes independent of both, f and l_p . For the given material parameters the critical frequencies f_l are 800 MHz (top row: $l_p = 5\lambda_L$) and 200 MHz (bottom row: $l_p = 10\lambda_L$), and $f_\lambda = 20 \text{ GHz}$ in both cases.

Calculation of Dissipated Power and Surface Resistance

The power dissipated by a flux line is calculated based on the obtained solution for u and we obtain:

$$P = \frac{H_p^2 \phi_0^2 (\sinh \sqrt{2\nu} - \sin \sqrt{2\nu}) \sqrt{\nu}}{2^{3/2} \eta l_p (\cosh \sqrt{2\nu} + \cos \sqrt{2\nu})} \quad (2.37)$$

where ν is the frequency f divided by a characteristic frequency f_l . Altogether, the calculations yield two characteristic frequencies, which separate three frequency ranges

$$f_l = g \rho_n \xi_{\text{GL}}^2 / 4\pi \mu_0 \lambda_L^2 l_p^2 \quad \text{and}$$

$$f_\lambda = g \rho_n \xi_{\text{GL}}^2 / 4\pi \mu_0 \lambda_L^4.$$

The dissipated power can be simplified according to the type of oscillation in the three frequency ranges:

$$P = \frac{16\pi^3 H_p^2 \lambda_L^4 \mu_0^2}{3\rho_n g^2 \xi_{\text{GL}}^2} l_p^3 f^2 \quad f \ll f_l, \quad (2.38)$$

$$P = \pi H_p^2 \lambda_L \xi_{\text{GL}} (2\pi \mu_0 \rho_n f / g)^{1/2} \quad f_l \ll f \ll f_\lambda, \quad (2.39)$$

$$P = \pi H_p^2 \xi_{\text{GL}}^2 \rho_n / 2\lambda_L \quad f_\lambda \ll f. \quad (2.40)$$

At low frequencies ($f < f_l$), the whole flux line segment between the pinning center and the surface oscillates. For $l_p = 10\lambda_L$ and parameters of clean niobium, f_l is at 200 MHz. With decreasing purity, f_l increases and for example at $l_p = 5\lambda_L$ it reaches 800 MHz. When f_l is exceeded, the oscillation of the flux line is mostly localized in a layer of thickness $1/q_\omega$, which is smaller than l_p but larger than λ_L . The losses become independent of l_p . At even high frequencies ($f_\lambda < f$), only the small tip of the flux line oscillates. The losses are now independent of f in addition to l_p . For clean niobium f_λ is at about 20 GHz.

The obtained equations can be used to estimate the additional surface resistance that is caused by trapped flux. To obtain the additional resistance, Reference [32] averages the dissipated power in Equation 2.37 over a statistical distribution of non-interacting vortex segments and yields

$$R_{\text{string}}(B_0) = \frac{B_0}{B_c} \left(\frac{\mu_0 \rho_n \omega}{2g} \right)^{1/2} \quad (2.41)$$

$$R_{\text{string}}(1 \mu\text{T}) = \frac{1 \mu\text{T}}{0.2 \text{T}} \left(\frac{4\pi 10^{-7} \frac{\text{N}}{\text{A}^2} \cdot 10^{-9} \Omega \text{ m} \cdot 2\pi \cdot 1.3 \text{ GHz}}{2 \cdot 1/2} \right)^{1/2}$$

$$= 16.0 \text{ n}\Omega. \quad (2.42)$$

for cavities with a resonance frequency of 1.3 GHz. Sometimes the resistance is approximated by taking the surface resistance in the normal state $(\mu_0\rho_n\omega/2)^{1/2}$ times the volume fraction of the flux line cores $B_0/2B_{c2}$ [3]. The additional resistance due to trapped flux is accordingly

$$R_{\text{fraction}}(B_0) = \frac{B_0}{2B_{c2}} \left(\frac{\mu_0\rho_n\omega}{2} \right)^{1/2} \quad (2.43)$$

$$\begin{aligned} R_{\text{fraction}}(1 \mu\text{T}) &= \frac{1 \mu\text{T}}{2 \cdot 0.4 \text{T}} \left(\frac{1}{2} 4\pi 10^{-7} \frac{\text{N}}{\text{A}^2} \cdot 10^{-9} \Omega \text{m} \cdot 2\pi \cdot 1.3 \text{ GHz} \right)^{1/2} \\ &= 2.8 \text{ n}\Omega. \end{aligned} \quad (2.44)$$

However, this simplified approach neglects the oscillation of the flux lines, which is included in the previously presented model. The revised equation predicts a multiple of the dissipation caused by the same amount of trapped flux for niobium cavities. For other material like Nb₃Sn the difference will be even larger.

Comparison to Experimental Findings

The findings of the theoretical model provide a strong ground to understand recent experimental results. It was reported that different surface treatments as the annealing with nitrogen or a low temperature (120°C) bake out increase the dissipated power for the same amount of trapped flux [33, 12]. Reference [12] systematically analyzed the sensitivity to trapped flux of niobium cavities with different mean free path values l . The variation in l was achieved by different cavity preparations, especially a change in material removal from the surface after nitrogen annealing. The least removal of 5 μm yielded the lowest l value of 4 nm while the most removal of 40 μm resulted in a mean free path of 213 nm. The sensitivity to trapped flux was measured and fitted using Equation 2.37. To obtain the dissipation as a function of mean free path, the penetration depth and coherence length were calculated as functions of l . Further, it was assumed that the number of scattering centers was larger than the number of pinning centers and that l_p depended linear on l .

As a result, a good agreement of theoretical prediction and measurement was found. Furthermore, l_p was approximated to be 75 times l . This number can be interpreted in terms of penetration depth. The shortest l measured in the experiments was 4 nm, which translates to $l_p \approx 8\lambda_L$. Taking the change in λ due to low purity into account (Equation 2.22), l_p is still more than twice the amount of λ . For cleaner material, with for example $l = 60 \text{ nm}$, l_p increased to over $100\lambda_L$. Furthermore, f_l can be estimated based on this numbers. A mean free path of 4 nm corresponds to

$f_l = 350$ MHz. All other cavities exhibited higher mean free paths and hence lower f_l values. Therefore, it can be concluded, that all tests were performed in a medium frequency range where the dissipation does not depend on l_p but on f . The study covered the whole range of mean free paths that are common in bulk SRF cavities, hence this result can be transferred to almost all bulk niobium cavities.

However, though the theoretical model fits qualitatively with recent experimental data, the predicted residual resistance due to trapped flux in Equation 2.42 overestimates the power dissipation for clean niobium. Experimental studies repeatedly found values closer to Equation 2.44. The reason for the discrepancy is not clear hence the quantitative comparisons in this thesis will use the experimentally determined rule of $3.5 \text{ n}\Omega$ per $1 \mu\text{T}$ [6].

2.3.4 Sources of Magnetic Field in the SRF Environment

Since already a few μT trapped magnetic flux can suffice to significantly increase the losses in SRF cavities, it is crucial to understand all sources of the magnetic field close to a cavity.

The Earth's Magnetic Field

Most prominent cause of ambient magnetic field is the earth's magnetic field. It varies with one's position on the globe. Some SRF test stands deploy compensation coils, which are tuned to create a field free environment within them. A second approach, which is the one followed at HZB, is applying magnetic shields. The shields consist of high permeability material that bundles the earth field in its walls and hence reduce the field in their midst. Usually, one shield is mounted close to the cryostat wall (outer shield) and a second one is mounted directly on the LHe tank of the cavity (inner shield).

The active compensation method has the drawback that one can only tune the coils to cancel the external field at a certain position and one has to be careful not to create an increased field at some other location. A shield does not have that downside. However, it shields best only when it is mounted as a sphere. Since cavities have in most cases a cylindrical geometry, the shielding efficacy will be reduced along the cavity axis. Furthermore, a shield has to have cut outs for the beam pipes and coupler, which further reduces its efficacy.

Magnetic Componentes

Some parts of the test setup may contain magnetic materials. Examples are several kinds of stainless steel and alloys. All non-austenitic steels are unfit for SRF applications. Further, RF cables can contain not suitable materials in connectors and sometimes non-magnetic components are mounted using magnetic bolts or tools that exhibit remanent magnetization and imprint some magnetization on initially non-magnetic parts. Special care has hence to be given to magnetic “hygiene” in the area of an SRF test stand or module.

Thermoelectric Currents

When a niobium cavity is cooled down to the operation temperature in a horizontal test stand, large temperature differences occur and by thermoelectric effect the temperature differences can cause currents and consequentially magnetic fields. Almost no investigations have so far been concentrated on the question how thermoelectrically generated magnetic field may compromise the RF performance of bulk niobium cavities. To gain a clear picture on that matter is one main goal of this thesis. The next sections will therefore summarize the existing literature on the topic, explain the basic principles of thermoelectricity and discuss the effect in the context of SRF.

2.4 Thermoelectric Currents

2.4.1 Thermoelectric Currents in the SRF Environment

In the 60th, the landmark experiments at Stanford transferred SRF technology from the lab to the first superconducting accelerator. The group of W.M. Fairbank, J.M. Pierce, H.A. Schwettman and P.B. Wilson addressed the central physical and technological issues. The experiments were performed with lead electroplated on copper cavities. They achieved Q_0 values of $5 \cdot 10^9$ at 1.85 K and maintained the Q_0 at fields approaching 20 mT, which corresponded to an accelerating gradient of approximately 5 MV m^{-1} . They proceeded with an extensive study of the residual resistance in the plated cavity. They sorted out cavities with visible causes for increased residual such as local flaws. Some defects on the surface were so large that they were actually visible to the unaided eye. The remaining cavities exhibited high Q values and the group concluded that the major source of the remaining residual resistance was trapped magnetic flux.

Thermoelectricity as a source of trapped flux and hence RF losses was first proposed in the PhD thesis of John Morley Pierce in 1967 [34]. In a study on shields that were fabricated out of lead plated copper, the group saw that a magnetic field appeared after the phase transition in areas that were previously well shielded. This study was not known at the beginning of the investigations presented in this thesis. At that time, the group concluded that thermoelectrically generated currents generated a magnetic field that got trapped during the phase transition. Since their SRF cavities were fabricated from the same material as the shields the group draw the conclusion that the effect would degrade cavities as well.

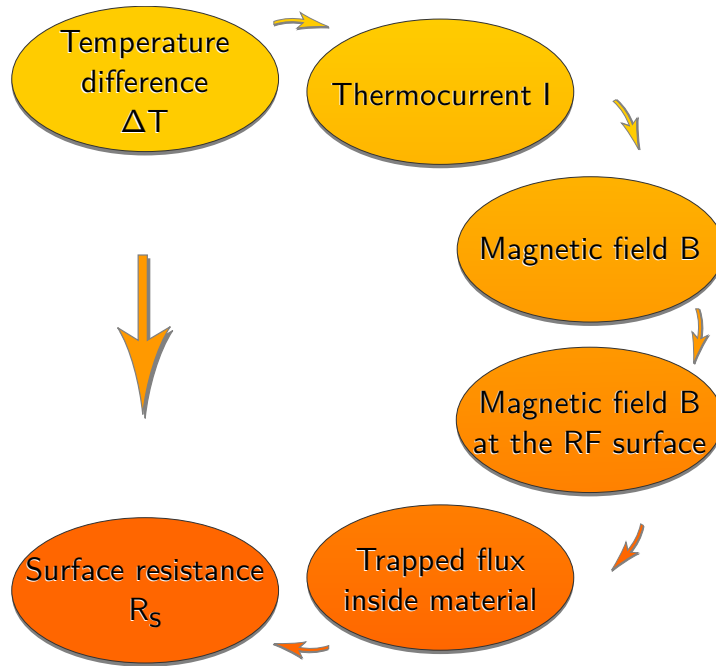
They evaluated data of zero field cooled cavities and had extensive private communication with other groups. All of them observed a lack of reproducibility in the residual losses. Cavities that had experienced identical surfaces preparation and handling still showed a large variation of residual resistance upon temperature cycling. Even in the same cavities, a variation in the order of a factor 2 or more was observed. By then, there was very little published on this topic. The overall conclusion was that there is a fairly strong indirect evidence that self-generated trapped flux due to thermoelectricity is the major source of residual losses in high- Q cavities. However, there was no direct evidence.

After the first observations with lead plated cavities [34, 35] other groups found a similar effect. In an environment where no trapped flux should occur, the residual resistance still showed flux induced losses. Reports are known from tin foils [36], more on lead plated copper [37] and reports in the first Nb₃Sn single and five cell cavities [38, 39].

The effect was understood as a local mechanism in a system consisting of films or compounds like the Pb on Cu, Nb on Cu or Nb₃Sn on Nb where the thermocurrents are generated at the film substrate interface. However, no study was dedicated to investigate the effect in detail or to approach the question in a systematic manner.

In the 90th, the thermocurrents were attributed exclusively to Nb₃Sn plated cavities [40] and when the interest of the community shifted to bulk Nb and Nb₃Sn research was discontinued the effect faded from the spotlight. In this work it will be shown that the effects can occur in bulk Nb cavities as well and even be rather pronounced. However, the impact seems to be in a different order of magnitude. It will be shown that residual resistance in the order of 10 n Ω needs temperature gradients of about 50 K while recent studies performed at CERN on coated cavities give similar resistance increases already with 1 K difference [41]. The high temperature gradients occur in bulk cavities due to the high cooldown rates that were introduced after the

Figure 2.8: Line of argument: The correlation of an increase in residual resistance and a temperature difference during the cooldown alone does not suffice to confirm the assumption that thermocurrents affect the RF performance. To prove the hypothesis we need to understand the thermocurrents, the generated magnetic field, especially at the RF surface and finally we must evaluate how much of the generated field gets trapped during the phase transition.



discovery of the Q disease. In the attempt to pass through the dangerous temperature range below 150 K as fast as possible, the side of the cavity that is close to the liquid helium inlet cools much faster than the opposing side. Here, thermoelectricity must be considered as a global effect in a system consisting of a cavity in its tank. In Chapter 3, it will be shown that the high temperature difference in the system correlates with increased RF losses. But thermoelectricity is only a suspect at first. To prove that it is indeed the cause of the increased losses each step on the line of argument must be traced as shown in Figure 2.8: The amount of generated current and the corresponding magnetic field need to be quantified. Next, it must be shown that the magnetic field is located and trapped at the RF surface because only there it will contribute to dissipation. At first glance one would not think so because the cavity-tank system exhibits toroidal symmetry and by Ampère's Law no magnetic field should reach in inner surface of the cavity. However, that symmetry is broken by additional temperature gradients. The estimation of the magnetic field at the RF surface will be addressed in Chapter 4. The final question that needs an answer is if the magnetic field gets trapped or expelled during phase transition. This topic is considerably large on its own hence only some specific aspects of it will be addressed Chapter 5.

2.4.2 The Thermoelectric Effect

The thermoelectric effect, or more specific the Seebeck effect, is the conversion of a temperature difference into an electric voltage. The effect is common and with a fairly simple model, the general idea of the Seebeck effect is captured. The model will be explained in the next paragraph, however, the description is oversimplified and leaves a good deal of open questions.

When a conductor is exposed to a temperature gradient, the charge carriers in the hot region have a higher energy and hence velocity than the ones in the cold region. Hence, they diffuse from hot to cold and a voltage establishes to counteract the charge separation. The magnitude of that voltage is characteristic for each material and is given by the property called thermopower or Seebeck coefficient S , measured in μV per K of temperature difference. S can be determined experimentally but only in a system of two materials. The reason is that any voltmeter has a fixed temperature and measures with leads, which connect it to the material of interest. If the tested material and the lead material are the same, the measured voltage at the voltmeter is zero because its two inputs are at the same temperature. If the leads are fabricated of a different material, the measured voltage will correspond to the difference of Seebeck coefficients of the tested material and the leads multiplied by the difference in temperature at the contacts. A few simple “keys” provide guidance when handling thermoelectric materials or in particular a thermocouple:

1. Two different metals are required to form a thermocouple.
2. No current flows in a thermocouple circuit made of similar materials just by the application of heat.
3. The size of the wire does not affect the output voltage.
4. The output voltage is independent of the temperature variations along its path.

Though this model helps with the general understanding, it cannot give a satisfying explanation for the fact that S is temperature dependent. It does not explain why some materials have negative S values or why S often has different signs for the same material at different temperatures. Furthermore, it invites misunderstanding on how the temperature distribution along material and leads must be designed to gain a reliable result. A comprehensive understanding of the Seebeck effect must derive from the electric and thermal transport properties of a metal.

Seebeck Voltage

One of the major textbooks on thermoelectricity by Blatt [42] focuses on the deduction of S from solid state theory. The deductions are out of the scope of this thesis but the introductory chapter of the book addresses the question of spatial voltage distribution, which is of importance. The notation that will be used to follow the reference is explained in Figure 2.9. Blatt derives the formula for the voltage tapped between points a and b as follows

$$\begin{aligned}
 \Delta V &= V_b - V_a = (V_b - V_c) + (V_c - V_d) + (V_d - V_a) \\
 &= \int_c^b dV + \int_d^c dV + \int_a^d dV \\
 &= - \int_c^b S_B(T) dT - \int_d^c S_A(T) dT - \int_a^d S_B(T) dT \\
 &= - \int_c^d S_B(T) dT - \int_d^c S_A(T) dT = + \int_d^c S_B(T) dT - \int_d^c S_A(T) dT \\
 &= \int_{T_1}^{T_2} (S_B(T) - S_A(T)) dT.
 \end{aligned} \tag{2.45}$$

Equation 2.45 is commonly used to evaluate the thermovoltage in an open system. The derivation does not assume that $S(T)$ is the same as $S(x)$. Under the reasonable assumptions that the Seebeck coefficients are continuous and that the temperature profiles are piecewise smooth, the terms can be handled as line integrals in a scalar field. Therefore it can be concluded that the integrated thermovoltage is path independent.

For applications this means that the temperature profiles $T(x)$ can take almost any shape without changing the resulting voltage (as long as the contact temperatures are kept). For most applications this is less important because they use temperature profiles, which are in good approximation linear and similar along materials A and B. In the SRF context however, very different temperature profiles must be considered because the two materials are the niobium of the cavity and the titanium of its tank. During the cooldown with LHe the temperature profiles of the two materials can be very different and far from linear. A quantitative analysis of the thermocurrent would be close to impossible without the path independence.

For visualization, Figure 2.10 shows three examples for different temperature profiles, which result in the same thermovoltage. In all cases, the profile in material A is chosen linear. The profile in material B is linear in case 1, quadratic in case 2 and a Gaussian peak in case 3. The second row shows the corresponding values of $S(T)$ at the respective x positions. Material properties are chosen to be those of

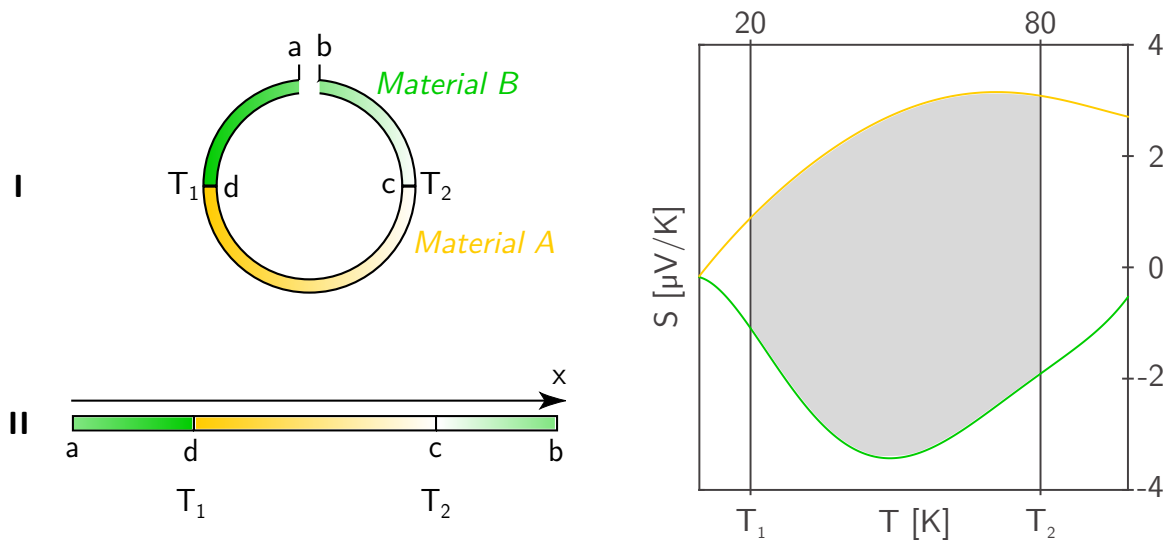


Figure 2.9: Sketch to explain Seebeck voltage: Picture I on the upper left is commonly used to visualize an open circuit of two materials, A and B, with contact temperatures T_1 and T_2 . The Seebeck voltage is tapped between a and b, which can be positioned at any point in the circuit. Below, pictures II shows a different depiction of the same situation. The spatial axis x is introduced. On the right hand side, two examples for the material parameter S are displayed as a function of temperature: Material A (yellow) was chosen to be niobium, material B (green) to be titanium (grade 2). The grey area between the curves corresponds to the resulting thermovoltage.

high purity niobium (material A) and grade 2 titanium (material B), for reference see Section 4.1. In the third row, the integrated voltage relative to a ground at position a is calculated. As expected for a line integral, the accumulated voltage, displayed as the dotted line in the third row, is the same in all cases: $311 \mu\text{V}$ for $T_1 = 20 \text{ K}$ and $T_2 = 80 \text{ K}$. Furthermore, it is equal to the value calculated with Equation 2.45 that corresponds to the grey area in Figure 2.9.

In addition, Figure 2.11 shows what would happen if material A was chosen to be superconducting ($S = 0$ at any temperature). Only material B contributes to the output voltage. For that reason superconducting leads are often used in measurements to determine the thermopower of other materials.

The figure also displays the case of material A and B being identical. It illustrates why the net voltage always vanishes in such a setup, even with different temperature profiles along materials A and B.

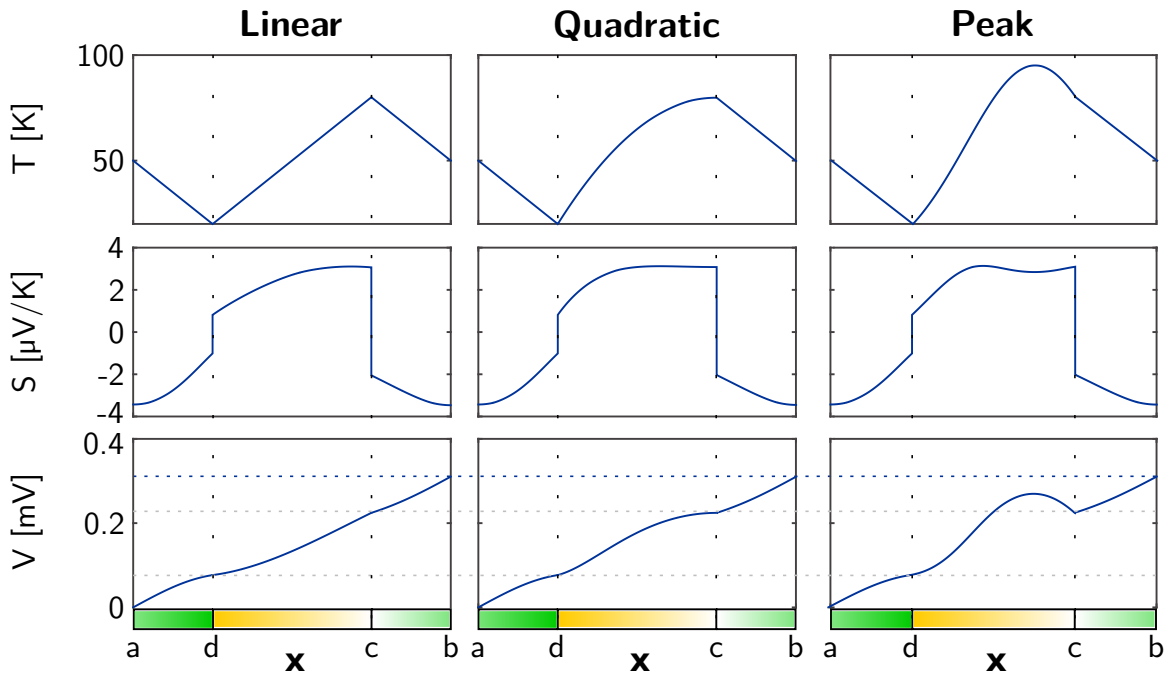
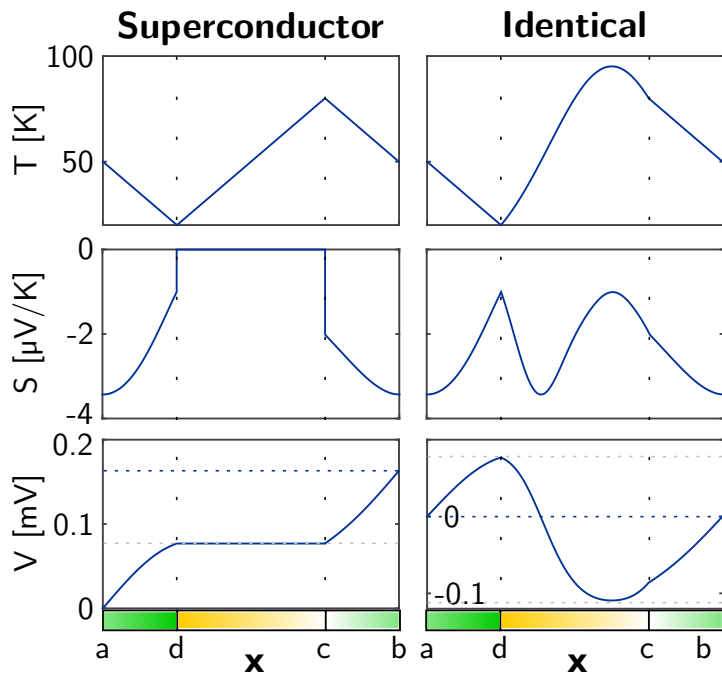


Figure 2.10: Seebeck voltage for different temperature profiles: The x coordinate is defined as shown in Figure 2.9. The upper row displays three different temperature profiles. Material A exhibit a linear temperature decrease in all three cases. Material B's temperature is increasing linearly in case 1, quadratically in case 2 and in the form of a Gaussian peak in case 3. Row 2 shows the corresponding values of $S(x)$. The third row gives information on the integrated voltage respective to a ground at position a. In all cases the finally accumulated thermovoltage is the same and the same as it would be calculated with Equation 2.45.

Figure 2.11: Seebeck voltage: The first row displays the temperature profiles. Row 2 shows the corresponding values of S . For the left column material A was chosen superconducting ($S = 0$), for the right column materials A and B were chosen to be the same. The third row gives information on the integrated voltage respective to a ground at position a.



Charge and Heat Current

The Seebeck effect itself describes only the generation of a voltage caused by a temperature difference and is just one aspect of the thermoelectric transport in a material. A more general form is given by the equations for charge and heat currents

$$\begin{aligned}\mathbf{J} &= \mathcal{L}_{11}\mathbf{E} + \mathcal{L}_{12}\nabla T, \\ \mathbf{Q} &= \mathcal{L}_{21}\mathbf{E} + \mathcal{L}_{22}\nabla T.\end{aligned}\tag{2.46}$$

The equations relate the two current densities \mathbf{J} (electrical current density) and \mathbf{Q} (heat current density) to the voltage and temperature gradients, which are reasonable parameters considering an experimental setup. The material properties, as the Seebeck coefficient, the thermal conductivity and the electrical conductivity, are hidden in the 3×3 tensors \mathcal{L}_{ij} . The derivation can be found in Appendix section A.

To show some examples for the thermocurrent in a closed circuit, we conducted numerical simulations. Two semicircles were joint, just as in the model in Figure 2.9. The circuit was closed. The parameter of interest was the current density \mathbf{J} in the system, which generated the magnetic field that potentially was trapped. S and σ were used as input parameters and set to various values to demonstrate how a change in the parameters influenced the current density in the closed loop. For simplification, both were chosen to be temperature independent and constant. All other material parameters were set identical in both materials. The results are presented in the table below. The first row gives a baseline for one set of parameters. In the following rows, the values that differ from the initial settings are marked purple.

Table 2.2: Thermocurrent density in a closed loop. Description in text.

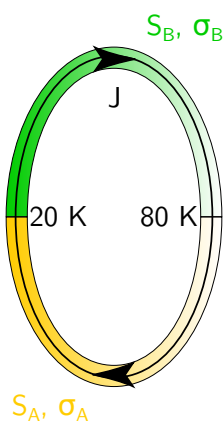
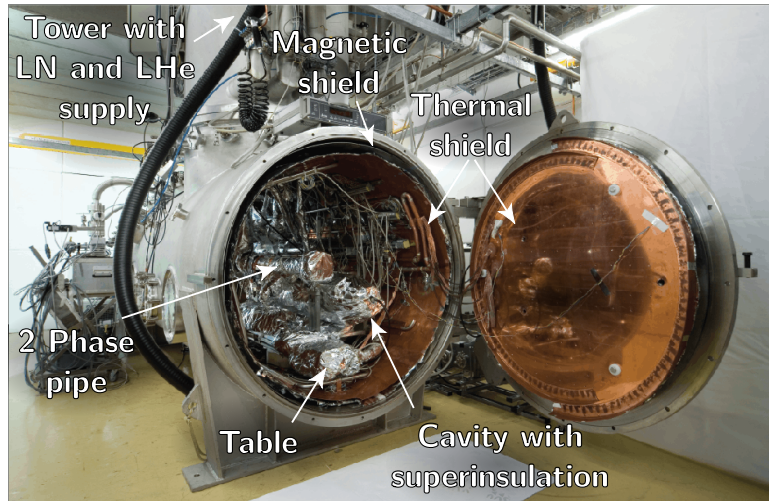
	Material A	Material B	\mathbf{J}
	$S_A = 2 \mu\text{V K}^{-1}$ $\sigma_A = 1 \cdot 10^7 \text{ S m}^{-1}$	$S_B = -2 \mu\text{V K}^{-1}$ $\sigma_B = 1 \cdot 10^7 \text{ S m}^{-1}$	405 A/m ²
	$S_A = 4 \mu\text{V K}^{-1}$ $\sigma_A = 1 \cdot 10^7 \text{ S m}^{-1}$	$S_B = 0 \mu\text{V K}^{-1}$ $\sigma_B = 1 \cdot 10^7 \text{ S m}^{-1}$	405 A/m ²
	$S_A = -2 \mu\text{V K}^{-1}$ $\sigma_A = 1 \cdot 10^7 \text{ S m}^{-1}$	$S_B = 2 \mu\text{V K}^{-1}$ $\sigma_B = 1 \cdot 10^7 \text{ S m}^{-1}$	-405 A/m ²
	$S_A = 2 \mu\text{V K}^{-1}$ $\sigma_A = 1 \cdot 10^7 \text{ S m}^{-1}$	$S_B = -2 \mu\text{V K}^{-1}$ $\sigma_B = 1 \cdot 10^3 \text{ S m}^{-1}$	0.08 A/m ²
	$S_A = 2 \mu\text{V K}^{-1}$ $\sigma_A = 1 \cdot 10^3 \text{ S m}^{-1}$	$S_B = -2 \mu\text{V K}^{-1}$ $\sigma_B = 1 \cdot 10^3 \text{ S m}^{-1}$	0.04 A/m ²

Figure 2.12:
The HoBiCaT cryostat for horizontal cavity tests at HZB (Foto courtesy FG-ISRF, HZB).



2.5 Experimental Methods

2.5.1 The HoBiCaT Cryostat

The experimental studies in this thesis were performed at the Horizontal bi-cavity test facility (HoBiCaT) at HZB [43]. Figure 2.12 shows the HoBiCaT cryostat with one open door. HoBiCaT's main purpose is cavity testing under accelerator-like conditions. The about 4 m long vacuum vessel contains a room temperature magnetic shield and a thermal shield at liquid nitrogen temperature. It can house two cavities at the same time. Each cavity that undergoes testing is welded into a tank that holds the superfluid helium.

Figure 2.13 shows a cavity in tank. The heat that is dissipated in the cavity is cooled away by the helium and transported through the chimney at the top of the tank into a two phase flow pipe. The temperature in the liquid phase is regulated by adjusting the pressure in the gas phase between 5 and 35 mbar corresponding to bath temperatures between 1.5 and 2.1 K. Several layers of superinsulation foil and a second magnetic shield are mounted directly to the LHe tank of each cavity. Thereby, the ambient magnetic field and static heat input into the helium are further reduced. The multilayer insulation also delays the heat input in case of a vacuum leak.

In addition to the cavities, smaller sample setups can be installed directly on the table that holds the cavities and that is cooled with 4.2 K helium. The samples are conduction cooled by copper straps.

Figure 2.8 in the previous section outlined the correlation between a high temperature difference in the cavity-tank system during cooldown and an increased surface resistance. It also showed all the interim steps that need to be understood to prove

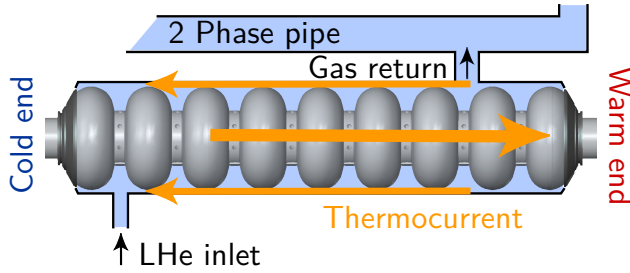


Figure 2.13: Nine-cell cavity in a horizontal test assembly.

the hypothesis that the increased losses are caused by thermocurrents, which elevate the trapped magnetic flux. The investigation of the effect requires a precise measurement of residual resistance, temperature and magnetic field. The following sections will outline the experimental techniques used to acquire the data on which the thermocurrent statement was based. The cavity performance measurement as well as the used temperature and magnetic field probes will be described.

2.5.2 Measurement of the Quality Factor and the Accelerating Field

The changes in cavity performance presented in this thesis are determined by evaluation of the figures of merit introduced in Section 2.1.2. The focus is on the surface resistance. R_s is calculated from the unloaded quality factor of the cavity and the geometry factor G according to Equation 2.6: $\langle R_s \rangle = G/Q_0$. The geometry factors used in this thesis are listed in Table 3.1 in Section 3.1. They are known from numerical simulations. Q_0 is measured by RF tests. A resonant mode of the cavity is excited by introducing RF power through an input coupler. Some of the power directed to the cavity (forward power P_f) is reflected (P_r), some is dissipated in the cavity walls (P_{diss}) and some power is transmitted through a pickup probe (P_t). During the test, the cavity is controlled and held on resonance by a phase-locked-loop, which is displayed and explained in Figure 2.14. The following sections will give an overview over the needed formulas to calculate Q_0 from RF data. For a detailed derivation see Reference [3].

CW Measurement

In a CW measurement the RF stays constantly turned on. The stored energy U in the cavity is stable over time ($dU/dt = 0$ and $U = U_0$). The three power values P_f , P_r and P_t are measured with directional couplers and power meters. The values are corrected for the cable attenuation. The quality factor resulting from the measurement does not correspond to Q_0 , the unloaded quality factor, as described in Equation 2.3 since

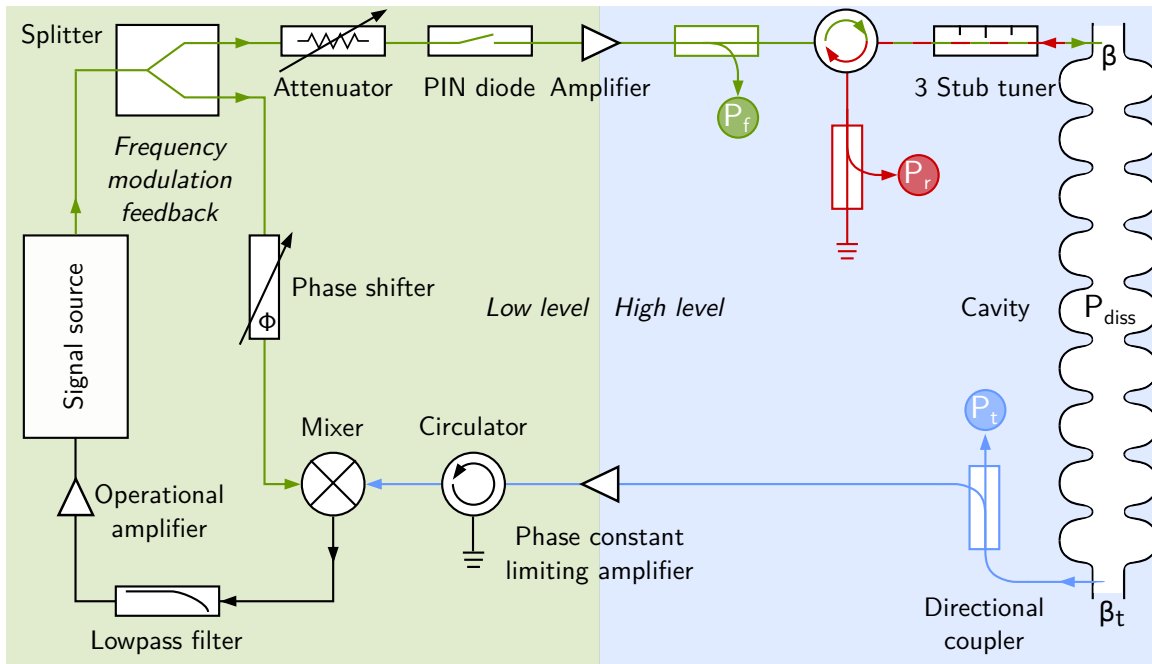


Figure 2.14: **RF measurement setup at HoBiCaT with phase-locked-loop:** The signal source (local reference oscillator) generates the 1.3 GHz signal that drives the cavity. After it is amplified, the forward power P_f (green) is measured via a directional coupler. The forward signal can be matched to the cavity with a 3 stub tuner after the circulator. The reflected signal, again, passes the circulator and is directed to a matched load in order to avoid reflection at the cables end. The reflected power P_r (red) is measured via a directional coupler. The transmitted power P_t (blue) is measured directly. A small fraction of it is attenuated. All amplitude modulations are eliminated and only the phase information is preserved. In the mixer the phase information is compared to the one of the signal source and the resulting phase error information is fed back to the signal source where the frequency is adjusted. A phase shifter is installed to optimize the frequency feedback loop. The PIN diode can be used to run in pulsed mode.

each cavity is equipped with two couplers. The measured quality factor relates to the loaded one $Q_L = \omega_0 U / P_{\text{tot}}$ where P_{tot} is the sum of the dissipated power inside the cavity and the power leaking out of both couplers. Q_0 is obtained from Q_L by evaluation of the coupling in a pulsed measurement.

Pulsed Measurement

The total power that is lost when the driving RF is turned off is the sum of the dissipated power and the power that leaks out the couplers $P_{\text{tot}} = P_{\text{diss}} + P_e + P_t$. When the power is turned off and the cavity is left to ring down the stored energy decays as

$$\frac{dU}{dt} = -P_{\text{tot}} \quad (2.47)$$

$$= -(P_{\text{diss}} + P_e + P_t) \quad (2.48)$$

where the loaded quality factor Q_L describes the decay of the stored energy and is given as

$$U = U_0 \exp\left(-\frac{\omega_0 t}{Q_L}\right) \quad (2.49)$$

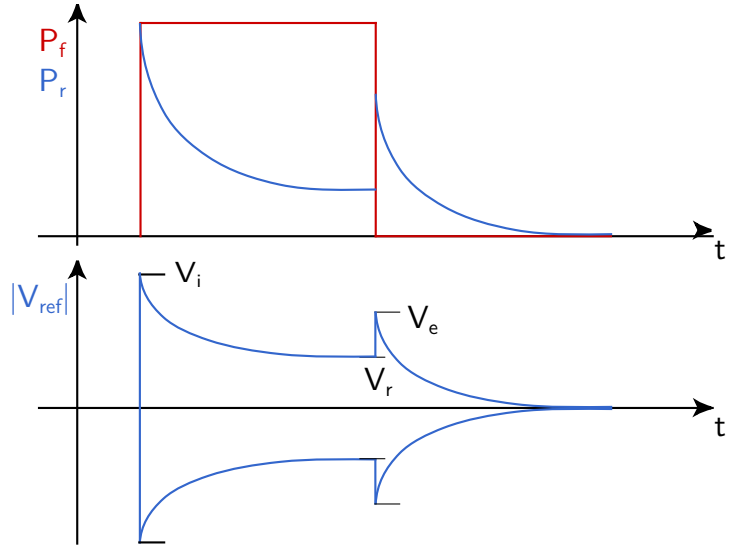
$$Q_L = \frac{\omega_0 U}{P_{\text{tot}}} = \frac{\omega_0}{\tau_L}. \quad (2.50)$$

The exponential decay time τ_L of the stored energy corresponds to the inverse Q_L and is measured in the reflected signal. The power balance can be written in terms of quality factors

$$\frac{1}{Q_L} = \frac{1}{Q_0} + \frac{1}{Q_e} + \frac{1}{Q_t} \quad (2.51)$$

where $\beta = Q_0/Q_e$ and $\beta_t = Q_0/Q_t$ define the coupling of the input and pick up coupler with respect to the field in the cavity. The pick up probe is usually adjusted to couple very weakly ($Q_t \gg Q_0$) and can therefore often be neglected in the following calculations. The coupling of the input coupler β is obtained from the trace of the reflected signal on the oscilloscope, which is displayed in Figure 2.15. When the RF is pulsed, the signal presents a peak on each switch. From the absolute height of both peaks (V_i and V_e) together with the steady state value (V_r), β can be calculated in three ways [3]. Since β is defined as always positive, the signs must be chosen accordingly.

Figure 2.15: Forward and reflected power during a pulsed measurement. In the bottom row, the trace of the reflected signal ($V_{\text{ref}}^2 = P_r$) on the oscilloscope provides the incident voltage (V_i), the reflected voltage (V_r) and the emitted voltage (V_e) for calculation of β .



$$\beta = \frac{V_e^2}{V_i^2 - V_r^2} \quad (2.52)$$

$$\beta = (2V_i/V_e - 1)^{-1} \quad (2.53)$$

$$\beta = \frac{1 \pm V_r/V_i}{1 \mp V_r/V_i} \quad (2.54)$$

All equations are equivalent. A fourth way is via the steady state power values in the CW measurement.

$$\beta = \frac{1 \pm \sqrt{P_r/P_f}}{1 \mp \sqrt{P_r/P_f}} \quad (2.55)$$

The accuracy of the four β s can vary between the equations depending on the value of β . One example is critical coupling with $\beta \approx 1$. It is easily identified in the oscilloscope trace because both peaks have the same height ($V_i = V_e$). A calculation based on the oscilloscope trace using Equation 2.53 will give an accurate result. The reflected power is almost zero. Hence, Equations 2.54 and 2.55 can give less accurate results because a number close to zero is divided by a comparatively large one and measurement error have a high influence on the result.

Other β values will cause different problems in the calculations, e.g. when $V_r \approx V_i$. Furthermore, potential cable calibration issues can impact the accuracy of β in the CW measurement and it must be considered that the PIN diode used for a pulsed measurement has a limited attenuation of 20 dB, which also influences the measurement. All in all, it is reasonable to use more than one equation during the measurement for crosschecking.

Acquisition of the Q versus E_{acc} Curve

A complete Q vs. E_{acc} curve is usually obtained by use of a calibration at low gradient. Nonlinear effects such as field emission have not yet set in. The decay curve after RF switch off follows the exponential decay and τ_L can be determined from the pulsed measurement of power versus time. The quality factor, the stored energy and the dissipated power are determined using τ_L and β from the pulsed measurement and CW value of P_f [3]

$$Q_0 = \omega_0 \tau_L (1 + \beta), \quad (2.56)$$

$$U = \frac{Q_0 P_{\text{diss}}}{\omega}, \quad (2.57)$$

$$\text{with } P_{\text{diss}} = \frac{4\beta}{(1 + \beta)^2} P_f. \quad (2.58)$$

The accelerating gradient is proportional to the square root of the stored energy. The constant of proportionality κ_E is determined by computer simulations

$$E_{\text{acc}} = \kappa_E \sqrt{U}. \quad (2.59)$$

The calibration uses the fact that Q_t does not change during the measurement and yields U/P_t and $E_{\text{acc}}/\sqrt{P_t}$. With this two constants, E_{acc} and Q_0 can be determined from the steady state power values and β

$$E_{\text{acc}} = \sqrt{P_t} \cdot \frac{E_{\text{acc}}}{\sqrt{P_t}}, \quad (2.60)$$

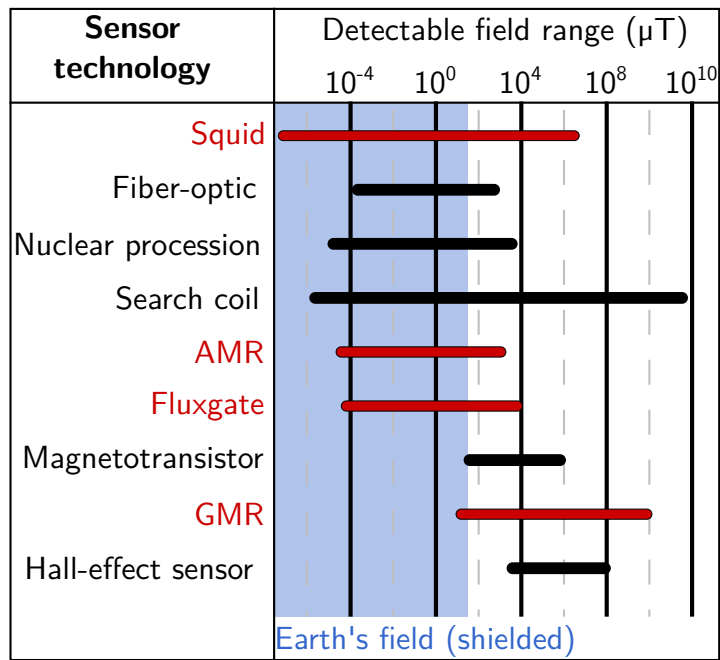
$$Q_0 = \frac{\omega_0}{P_{\text{diss}}} \cdot P_t \cdot \frac{U}{P_t}. \quad (2.61)$$

In case of the inset of non-ohmic losses at higher gradients, the decay will not be a simple exponential anymore and the measurement of τ_L gets complicated. The calibrations, however, stays valid and can be used instead of taking decay measurements.

2.5.3 Measurement of the Magnetic Field

The correlation of losses with locally increased magnetic field is only feasible with directly measured magnetic field data. The magnetic field probe of choice hence has to withstand the cryogenic environment without being compromised. The expected magnetic field is in the range of several 10 μT and a resolution down to the nT range is desirable. Reference [44] provides a comprehensive overview over the different technologies to measure magnetic fields and their range. Figure 2.16 displays an adapted figure of the reference where the range of some technologies is plotted. The ones considered for this thesis are marked red.

Figure 2.16: Detectable field range for several magnetic field sensing technologies. The red ones were considered for SRF tests. The Figure is adapted from Reference [44].



Selection of Suitable Probes

At first glance, a variety of sensors seem to be in line for the tests, however some limitations must be considered. For one, several technologies, especially for low fields like the *fiber-optic method* or *nuclear procession*, require large and/or expensive infrastructure or cannot be used at cryogenic temperatures. Hence, they are not applicable. Further, probes that are based on the *Hall effect* are very well understood and reliable. However, they are designed for higher fields and have not the resolution that we need to detect small changes in the magnetic field where it is desirable to resolve the nT range.

Search coils have a very large field range but they are based on Faraday’s law of induction and hence measure time varying fields or need to be moved to measure. The technology detects neither slowly changing fields nor DC fields.

Squids (superconducting quantum interference devices) are designed for very low magnetic fields since they rely on a quantum phenomenon. They require a cryogenic environment, which would already be provided in an SRF test. However, after discussion with colleagues from the University Jena (Institut für Festkörperphysik, AG Tieftemperaturphysik) it surfaced that Squids are not suitable because they are optimized for even lower magnetic fields than the range of interest in SRF research. Adapting the Squid technology for signals in the μT range would be complex and costly. We therefore refrained from this technology.

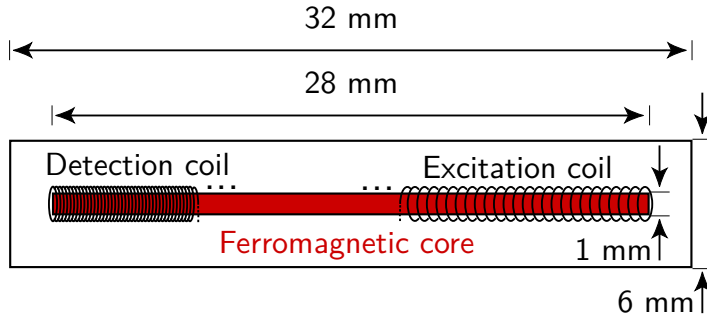


Figure 2.17: Cross section of a fluxgate magnetometer. The cylindrical ferromagnetic core (red) is surrounded by the excitation and the detection coil.

Giant magnetoresistive probes (GMR) utilize an effect observed in adjacent ferromagnetic layers. The electrical resistance exhibits a significant change in the electrical resistance depending on whether the magnetization of the layers are in a parallel or an antiparallel alignment. GMR technology is widely used in consumer electronics and affordable. Preliminary investigations at HZB with commercially available chips showed that they provide a sufficient resolution but not the required accuracy hence the approach was not further pursued.

Fluxgate Magnetometers

Fluxgate magnetometers (FG) with a resolution in the nT range are commercially available and they meet our requirements. The technology has proven fit for SRF research [45]. Every magnetometer consists of a thin, very soft ferromagnetic core with a low remanence that is surrounded by an excitation coil and a detection coil [46]. The setup is enclosed in a plastic shell. The dimensions of the shell and the ferromagnetic core are given in Figure 2.17.

An FG can measure the magnetic field in one spatial direction parallel to the core axis. The excitation coil creates an AC magnetic field that is oscillating with a frequency in the order of 10 kHz and with an amplitude in the order of 10 mT. The field drives the ferromagnetic core into saturation. The detection coil is exposed to the alternating field in the core and a voltage is induced [47].

In the absence of any external field, the detected field is equal and opposed to the excitation field. If an external field H_{ext} is present, the two signals differ. The magnetic field in the core is a superposition of the AC field and the external field H_{ext} . A harmonic decomposition of the induced voltage yields a linear dependence of the second harmonic's amplitude on H_{ext} . A detailed derivation is given in Appendix B. The FG's read out unit converts the transformed and filtered signal into a magnetic field value.

A FG provides a resolution of 1 nT and a precision of about 10 nT. The spatial resolution is given by the length of the core. The latter must be accounted for when the FG data is analyzed in a setup with an inhomogeneous magnetic field. One example is the superconducting phase transition. The FG will detect the change in magnetic field caused by the Meissner effect only as an averaged value over its length.

AMR

A TESLA-type nine-cell cavity has a length of about 1 m. Though a thermocurrent will flow in the whole setup giving rise to a global magnetic field, the local magnetic field will vary strongly due to e.g. the superconducting phase transition. A full understanding of all involved effects hence requires the measurement of all three spatial components of the magnetic field at as many positions as possible. Here, FGs reach their limit because of their size and price (about 1000 € per probe without read out). A potentially cheaper alternative are AMR probes that utilize the anisotropic magnetoresistive effect [44]. They are smaller than FGs, widely used and still have a good enough magnetic field resolution. AMRs usually come as SMD chips and are specified for operation down to -30°C . Within this thesis they were successfully tested at cryogenic temperatures and thus used in one cavity experiment. In the outlook section, a new diagnostics tool based on AMR technology will be proposed. The next sections will describe their functional principle in general. More details can be found in Appendix C.

The anisotropic magnetoresistive effect was first discovered in ferromagnetic materials. It was observed that the electrical resistance in such a material depends on the angle between the materials magnetization and the current flowing inside it. Nowadays, a magnetometer device based on AMR use thin films that change their resistance by a few percent in the presence of a magnetic field (usually sensitive up to $\approx 200\text{A m}^{-1}$). Each film consists of magnetic domains, which need to be aligned in the same direction. During fabrication, the films are deposited in a strong magnetic field and thereby the preferred orientation of the magnetization vector \mathbf{M} , the so-called “easy axis”, is set parallel to the length of the resistor. Later, shorting bars are positioned on the thin films at a 45° angle. Their resistance is very low while the AMR’s resistance is in the $\text{k}\Omega$ range. The current is forced to flow at a 45° angle to the easy axis. Figure 2.18 shows a AMR thin film with shorting bars, the easy axis and the sensitive axis. If an external magnetic field is applied perpendicular to the easy axis, \mathbf{M} will rotate. The angle between \mathbf{M} and the current will change leading to a change in resistance [44].

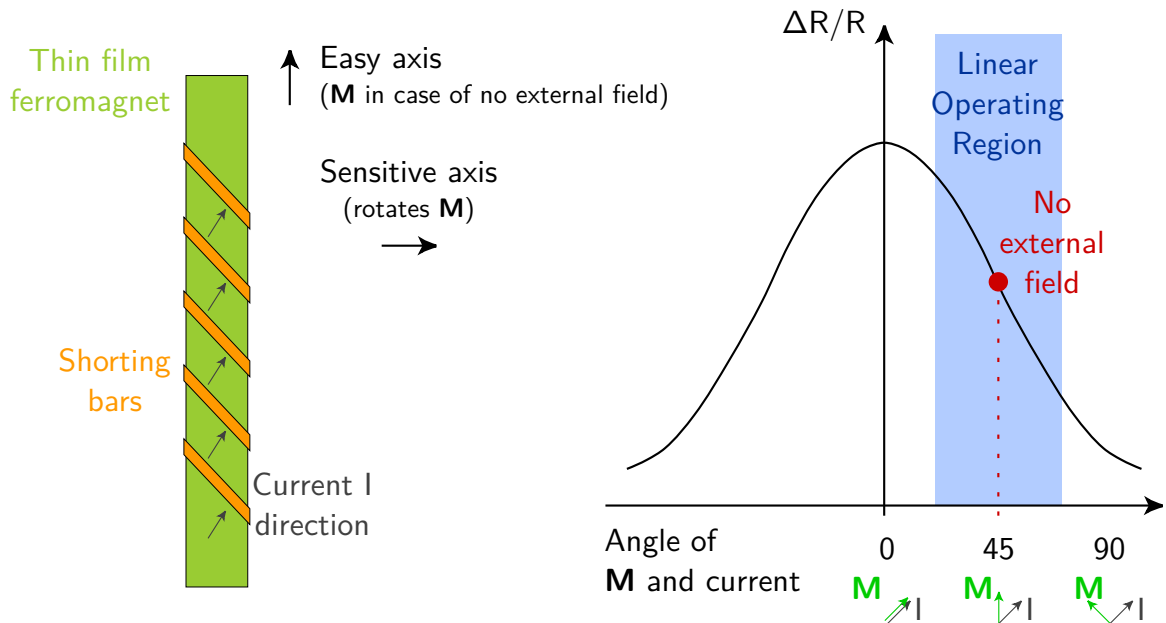


Figure 2.18: AMR sensor: Ferromagnetic thin film with 45° shorting bars. The magnetization vector \mathbf{M} is orientated along the easy axis for no external field. If a field is applied, \mathbf{M} is rotated. The Figure is adapted from Reference [44].

Figure 2.18 displays the change in resistance as a function of angle between magnetization and current. The resistance is maximum if the current and the magnetization vector are in parallel and minimum if they are perpendicular to each other. The shorting bars in each thin film force the current to flow 45° relative to the easy axis of the thin films where the change in resistance exhibits a linear region. With this setup, the external magnetic field component perpendicular to the easy axis (but in the plane of the thin films) can be measured because it rotates the magnetization vector \mathbf{M} and thereby in- or decreases the angle between \mathbf{M} and current.

AMR sensors are commercially available for just a few Euro up to several hundred Euro. Depending on the fabrication quality and the effort that is invested for the control and read out electronics, they should be able to reach the low nT range and detect magnetic field changes that are relevant for SRF research with an improved cost-benefit ratio compared to FGs. However, it must be kept in mind that AMRs are not specified for use at cryogenic temperatures. Appendix E will give first results of AMR sensors applied inside the HoBiCaT cryostat during operation.

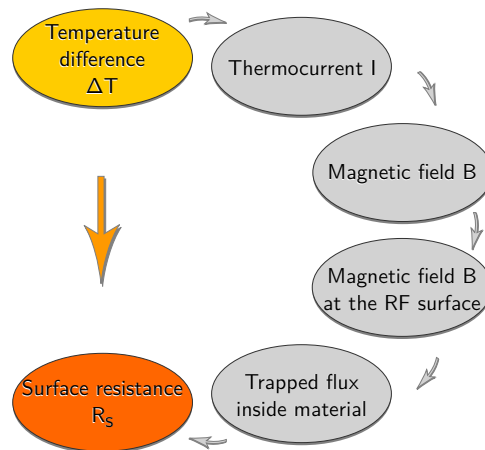
2.5.4 Measurement of the Temperature

A common sensor type for precise temperature measurement at cryogenic temperatures is the Cernox sensor (Cx). It is based on a four wire resistance measurement of a semiconductor with use of a calibration curve and has a mK resolution at low temperatures. At higher temperatures e.g. room temperature they are less accurate because their resistance is low.

The main challenge when using Cernox sensors in vacuum is to achieve a good connection between the sensor and the surface of a cavity, tank or sample. For the tests in this thesis, the sensors were bolted to a copper platelet. Thermal contact was improved with a thin Apiezon film applied between them. The platelet was afterwards glued to the surface with cryo compatible glue (e.g. Ecobond). In addition, pressure was applied to the platelet to improve the connection. The four leads of each sensor are thin and hence have a low heat input to begin with. They were intercepted at the LN shield and taped to the LHe tank to further minimize it.

Chapter 3

Evidence of Thermoelectric Loss Contribution in Cavity Tests



The research in this thesis was driven by an experimental finding that was presented in 2011 [14]: Large variations in the intrinsic quality factor of a nine-cell TESLA cavity were observed during an accelerator-like test in HoBiCaT. After the initial cooldown from room temperature, a good Q_0 value of $1.67 \cdot 10^{10}$ at 1.8 K and 4 MV m^{-1} was obtained. The very same cavity with identical coupler settings and RF calibration etc. improved during the cold run first to $2.7 \cdot 10^{10}$ and later even to $3.2 \cdot 10^{10}$ (at 1.8 K and 4 MV m^{-1}) only by warming it up above the transition temperature and cooling it down again with slightly modified cooling conditions.

Several causes for this astonishing behavior were considered and summarized in Reference [16]: A change in the efficacy of the magnetic shielding was measured and ruled out, as well as a change in surface adsorbates. It became apparent that the variation in Q_0 was caused by a variation in trapped magnetic flux. In samples, it had been demonstrated that thermoelectrically generated magnetic flux could get

Table 3.1: TESLA cavity design parameters [6] and simulated values for the used cavity (Courtesy Axel Neumann).

Accelerating mode	1.3 GHz
Design gradient E_{acc}	25 MV m ⁻¹
Iris diameter	70 mm
Length of one cell (midcup)	57.7 mm
Geometry factor (design value)	270 Ω
R/Q	1041 Ω
Geometry factor π mode	271.2 Ω
Geometry factor $1/9 \pi$ mode	271.5 Ω
Geometry factor $8/9 \pi$ mode	268.3 Ω

trapped in niobium during the phase transition into the superconducting state [48]. Hence an investigation of the potential thermoelectric contribution to the trapped magnetic flux inside a TESLA nine-cell cavity and thereby to its R_{res} was the next step.

The following paragraphs will first introduce TESLA cavities and their importance for accelerator physics. An explanation of the different cooldown schemes of HoBiCaT and the associated cooling conditions for a cavity will be given and, subsequently, two extensive studies will be presented that link the cooldown conditions with RF results for two different TESLA nine-cell cavities: One with a standard surface treatment (“BCS cavity”) and one that was nitrogen annealed (“N-doped cavity”).

3.1 The TESLA Cavity and Its Passband Modes

Starting in the 90s, the TESLA Collaboration worked on ways to make the SRF technology a competitive option for a 500 GeV center-of-mass energy superconducting linear collider. Its basic objective was to increase the cost effectiveness of the superconducting technology by at least one order of magnitude. The accelerating field could be increased from 5 MV m⁻¹ to about 25 MV m⁻¹ and the overall costs per unit length of the linac were reduced by using economical cavity production methods and a greatly simplified cryostat design. In 2000, the collaboration defined the design and surface treatments for a 1.3 GHz nine-cell cavity: the TESLA cavity [6]. Table 3.1 gives some design parameters and the simulated geometry factors.

The TESLA cavity has nine cells, which interact. The TM_{010} mode hence splits up in a passband of nine modes. Each mode has a different cell to cell phase shift, which is given in its name [49]. Figure 3.1 shows a sketch of the cavity and of the three passband modes that were measured in this thesis: The accelerating π mode with a cell to cell phase shift of π , the $1/9 \pi$ and $8/9 \pi$ modes with correspondingly

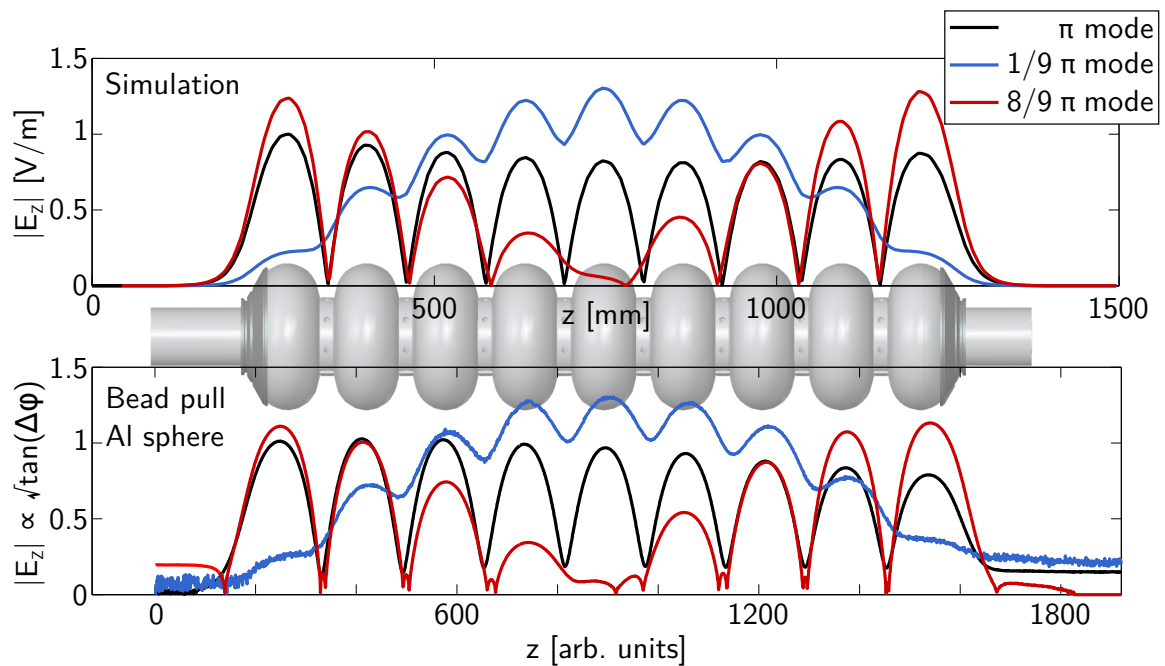


Figure 3.1: Field distributions of three used passband modes of the TESLA-type cavity: π mode, $1/9\pi$ mode and $8/9\pi$ mode. The upper graph shows the computed electric field with CST and the bottom graph displays the field measured with a bead pull setup using an Al sphere (Courtesy Axel Neumann and Adolfo Velez).

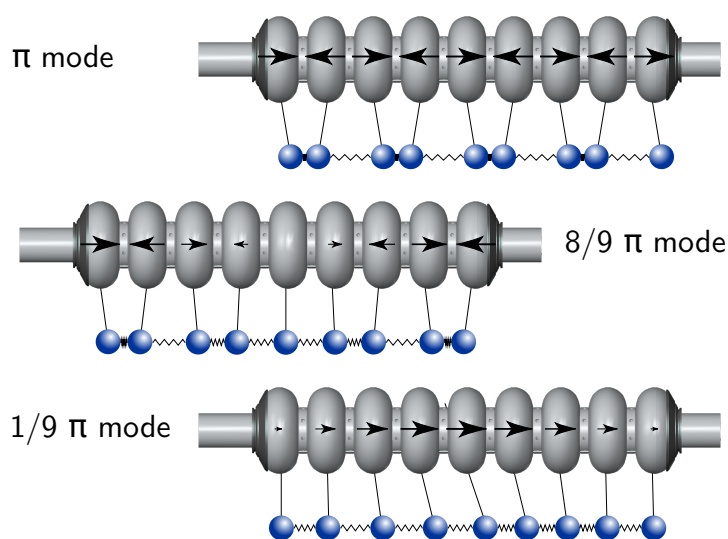
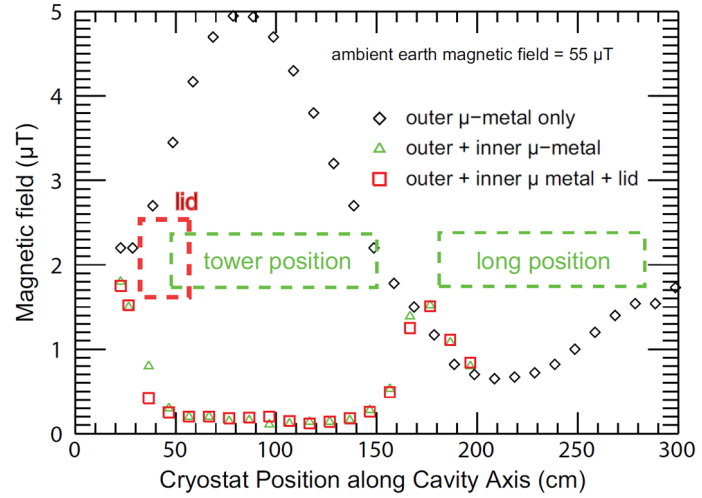


Figure 3.2: Field orientation in the π , $8/9\pi$ and $1/9\pi$ mode of a nine-cell cavity and the three modes in an analog system of nine coupled mechanical pendula.

Figure 3.3: Earth’s magnetic field inside the HoBiCaT cryostat from [43]. The black data points are taken with only the outer magnetic shield. The green markers are for outer shield combined with the inner shield and the red markers include the lids of the inner shield in addition (Courtesy Dr. Oliver Kugeler).



lower phase shifts. Figure 3.2 adds the orientation of the electric field to the magnitude information in Figure 3.1. Furthermore, the equivalent modes of nine coupled mechanical pendula are displayed for better understanding.

The use of three modes has the advantage that different parts of the cavity can be probed. In a measurement with the π mode, the surface resistance is averaged uniformly over the whole cavity. A measurement in the $1/9\pi$ averages mainly over the middle cells, while the $8/9\pi$ mode focuses on the end cells. Figure 3.3 shows the magnetic field along the HoBiCaT cryostat at the two cavity positions (“long” and “tower”). The shielding is less effective at the end cells of each cavity with respect to the middle cells. This could lead to an inhomogeneous distribution of trapped flux in the cavity with a higher level in the end cells. The measurement with three different passband modes provides a tool to differentiate between regions with different levels of trapped flux.

3.2 HoBiCaT Cooldown Schemes

The measurements in the three passband modes were repeatedly performed after the cavity experienced various cool down (CD) and warm up cycles. Figure 3.4 shows the setup of the cryoplant of HoBiCaT that fills the helium tank via two valves, the filling valve (FV) at the bottom left and the Joule-Thomson valve (JTV), which fills the tank from the top right via the 2 phase pipe. HoBiCaT provides three different cooling schemes for a cavity and each scheme yields characteristic spatial and temporal temperature gradients in the cavity-tank system. With decreasing temperature, the heat capacity and thermal conductivity of all materials decrease, too. Hence the

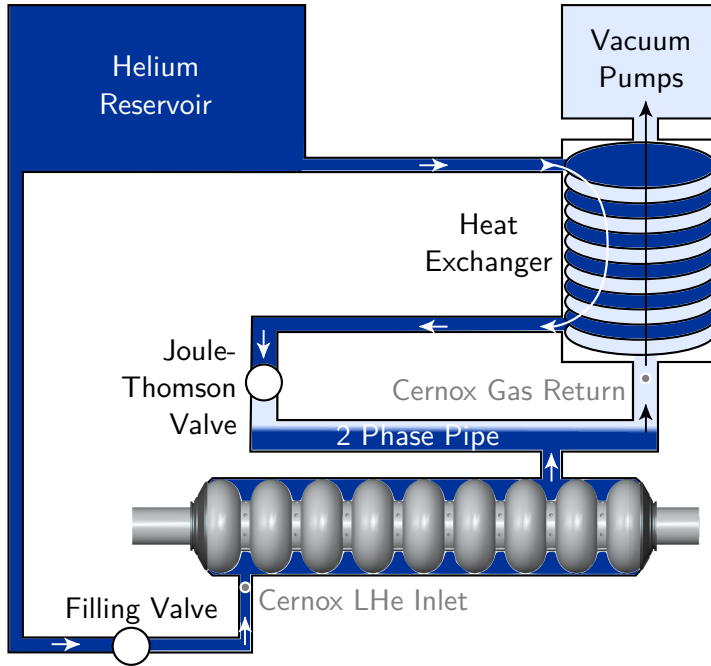


Figure 3.4: Cryoplant setup of HoBiCaT: The helium tank is filled via the filling valve and the Joule-Thomson Valve. The vacuum pumps allow for gas pressures between 5 and 35 mbar corresponding to bath temperatures between 1.5 and 2.1 K. The tank is mainly filled via the filling valve during the initial cooldown while it remains closed and the JT valve is used for filling during a thermal cycle leading to an inverted spatial temperature gradient.

thermal gradients at cryogenic temperatures can become much larger than expected from room temperature intuition.

During the *initial cooldown* (Figure 3.5a), mainly the FV at the bottom of the cavity is used for filling the tank with 4.2 K liquid helium. Hence the coldest spot is always close to the FV and there are high spatial temperature gradients both along the cavity and from the bottom to the top. The JTV is 25 % open as well to cool the heat exchanger effectively. The cavity itself is not cooled via that line.

A *thermal cycle* (Figures 3.5c and 3.5d) starts at 1.8 K. The cavity is warmed up to a temperature above T_c and subsequently cooled down again. During the process the FV remains closed. Only the JTV is used. As a first step, it is closed and heaters on the cavity are used to evaporate the helium in the tank and, if desired, to establish a temperature difference between the cavity ends. A Cernox sensor close to the LHe inlet in the bottom of the tank (Cx 5) measures a step-like change in temperature once the tank is empty (only shown in Figure 3.5d). In addition, the temperature of the evaporated gas is monitored with a Cernox sensor. Once the liquid helium is evaporated, the gas warms up quickly and this sensor exhibits a characteristic rise in temperature and can be used as an indicator for the state of the cryosystem. Now, the cavity is normal conducting everywhere. Once the desired temperature distribution in the system is reached, the JTV is opened again. Helium gas starts to flow through the system and cooling is restarted. As soon as the first liquid enters the tank, a drop in temperature is registered at Cx 5 (green) at the bottom of the tank. Over time, the

3. Evidence of Thermoelectric Loss Contribution in Cavity Tests

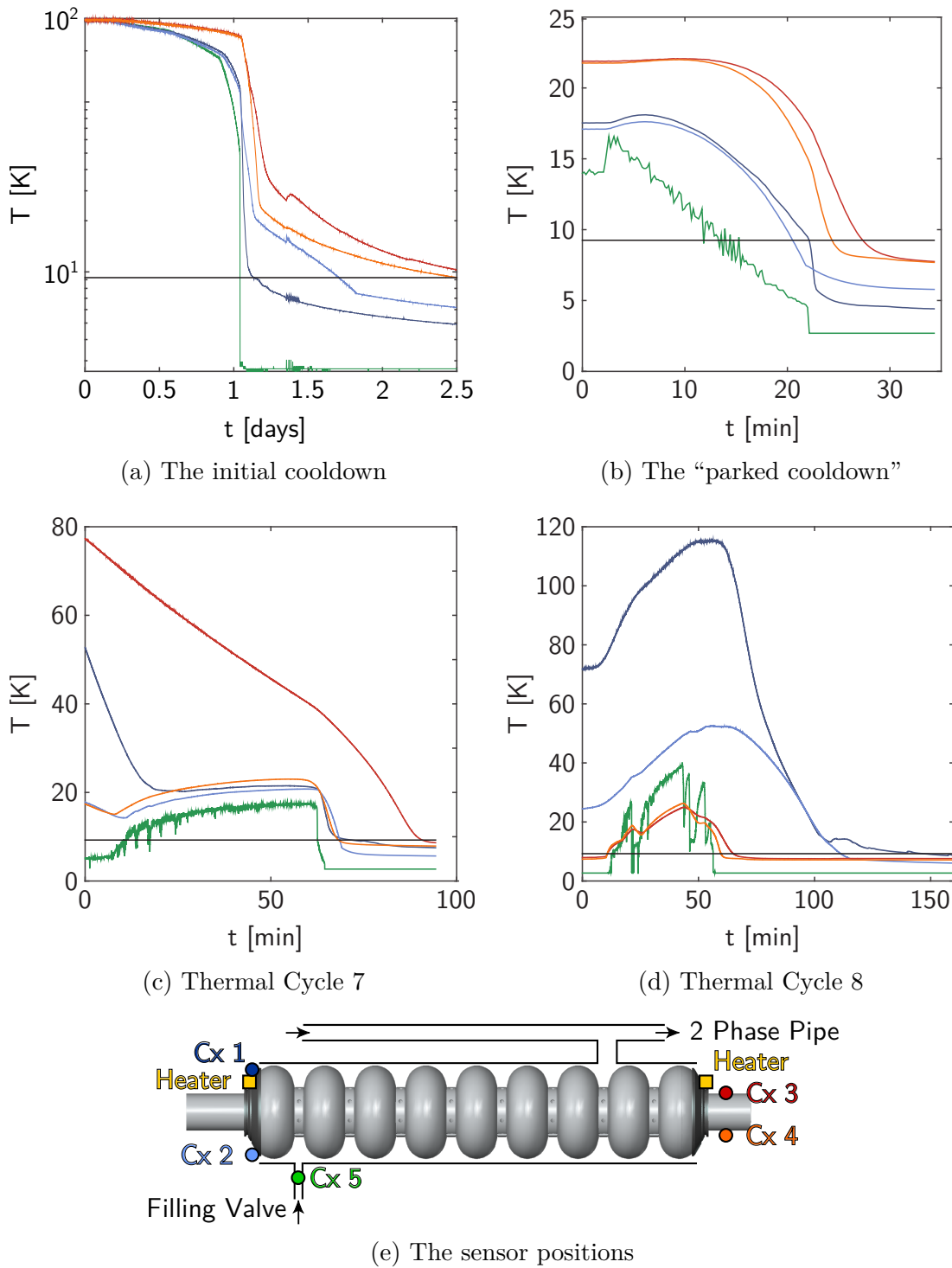


Figure 3.5: Temperatures during the different cooling schemes: (a) the initial cooldown from room temperature, (b) the cooldown from room temperature with parking at about 20 K, (c) a thermal cycle with a low temperature difference and (d) a thermal cycle with a high temperature difference. T_c of niobium is indicated as solid black line. (e) shows the positions of the Cernox sensors. The colors of the sensors correspond to the line colors in the plots.

cavity cools back to operating temperature. Since the helium is poured from the top right, a thermal cycle may lead to a reversed spatial temperature difference compared to the initial cooldown.

The third possible cooling scheme is a “*parked cooldown*” from room temperature (Figure 3.5b). It combines properties of both the initial cooldown and the thermal cycle. The cooling procedure of the initial cooldown is adapted to stop well before the superconducting phase transition. The cryoplant is balanced to maintain a constant temperature at the FV for 48 h. First, it is set to 30 K and then continuously lowered to 14 K. Both valves, the FV and the JTV, are used. After all temperature sensors are clearly in equilibrium the set point is lowered further towards 1.8 K and the cavity transitions with a small $\Delta T < 10$ K into the superconducting state.

3.3 The BCP Cavity

The first RF test results that will be presented in this thesis were obtained with a cavity that had received a heavy buffered chemical polishing (BCP) of about $150\ \mu\text{m}$ prior to a 2 h bake-out at $800\ ^\circ\text{C}$ to remove residual hydrogen. A light BCP etch in the order of $10\ \mu\text{m}$ followed the baking. The treatment was performed at DESY. It is similar to the standard treatment for TESLA cavities and comparable to the treatment of the 800 cavities for the European XFEL¹.

Before the helium tank was welded onto the cavity it was tested in a vertical assembly at DESY. Its quality factor was determined as $2 \cdot 10^{10}$ at 2 K in the π mode, which corresponds to a residual resistance of $1.2\ \text{n}\Omega$ based on the BCS parameters that were later determined in the horizontal test.

At HoBiCaT, the cavity was equipped with a TTF-3 input coupler [50]. The coupling during the RF cold tests was in most cases close to critical and always between 0.3 and 3.5, which results in an error margin of 10 % in Q_0 [51].

Altogether, one initial cooldown from room temperature, followed by 11 cycles, one parked cooldown from room temperature and another two cycles were performed within one run of the experiment. The temperatures in the cavity-tank system were monitored with five Cernox sensors. Their positions and typical readings were displayed in Figure 3.5. After each cooling procedure, Q_0 was measured versus temperature at a gradient of $4\ \text{MV m}^{-1}$ in the π mode. The $8/9\ \pi$ and the $1/9\ \pi$ mode were

¹ 400 cavities underwent $110\ \mu\text{m EP} + 800\ ^\circ\text{C annealing} + 40\ \mu\text{m EP}$. The other 400 cavities underwent $140\ \mu\text{m EP} + 800\ ^\circ\text{C annealing} + 10\ \mu\text{m BCP}$. EP stands for electropolishing.

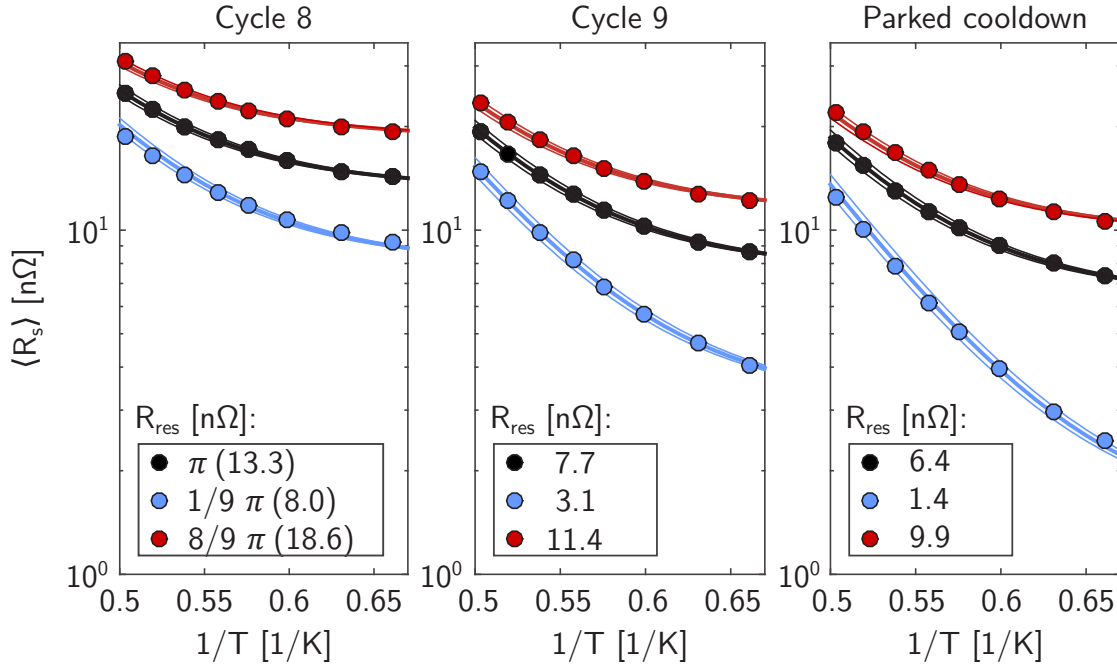


Figure 3.6: BCS fits of three measurements: Cycle 8 (highest ΔT during phase transition), Cycle 9 (medium ΔT) and the parked cooldown (lowest ΔT). The thick lines indicate the BCS fits. The thin lines indicate the range of fits that are covered by the uncertainty of a and b .

measured at the same peak field corresponding to 4 MV m^{-1} in the π mode. The residual resistance was extracted as will be explained in the next section.

3.3.1 The BCS and the Residual Resistance

The temperature-dependent BCS part of the surface resistance was extracted with the curve fitting described in Equation 2.21. For all measured modes and different cycles, the fit parameters a and b overlapped within the error margin. Thereby the fits confirmed that R_{BCS} remained constant independent of the cooling procedure. Overall parameters were calculated from a comprehensive fit on all data points. The result was found to be

$$a \cdot f^2 = (1.64 \pm 0.06) \cdot 10^{-4} \Omega \text{ K} \quad (3.1)$$

$$b \cdot T_c = (17.63 \pm 0.07) \text{ K}. \quad (3.2)$$

The values are in reasonable agreement with the expected values, which were explained in Section 2.2.3. The parameter $b = 1.9 T_c$ is just as expected for clean niobium. Based on the parameters for the BCS contribution, the residual resistance was extracted. Figure 3.6 provides examples for the curve fitting. In the Figure, the

Table 3.2: Examples of measured residual resistances of the three passband modes. The error of R_{res} can be estimated to 10% based on error propagation from the RF measurement [51]. Geometry factors are given in Table 3.1.

$R_{\text{BCS}} \approx 0.9 \text{ n}\Omega$ at 1.5 K	R_{res} [n Ω]		
	π mode	$8/9 \pi$ mode	$1/9 \pi$ mode
Initial cooldown	13.6	14.2	10.6
Thermal cycle 8 (high ΔT)	13.3	18.6	8.0
Parked cooldown	6.4	9.9	1.4
Thermal cycle 7 (low ΔT)	6.5	9.9	1.9

error bars of the RF measurement are within the symbol size. Table 3.2 compares some fit results in terms of R_{res} . After the separation of BCS and residual contribution, R_{res} was correlated with temperature data obtained during each cooldown to understand the thermoelectric generation of trapped flux.

3.3.2 Correlation of Residual Resistance and Cooling Parameters

The cavity had a length of more than 1 m and was equipped with only two temperature sensors at each end. Hence the search for an appropriate ΔT variable to correlate R_{res} with was challenging. With the focus on thermocurrents, it is reasonable to evaluate the temperatures of the two Nb-Ti junctions during the superconducting phase transition. However, this approach yields further questions.

1. When does the phase transition start?
2. When does the phase transition end?
3. Which temperature value is to be used for the calculation when each junction exhibits a non-uniform temperature profile?
4. What is the influence of other materials in the system (e.g. the NbTi helium vessel heads)?

These questions cannot be answered in detail due to the sparse temperature instrumentation. Nevertheless, some insight was gained by a measurement of the π mode bandwidth during one complete cycle. When the cavity turned normal conducting during the warm-up, the bandwidth suddenly increased and the same reversed during cooldown. The test allowed for a correlation of the superconducting transition with

the temperature data. The cavity went from normal to superconducting state within a window of less than a minute around the time when the first sensor at the ends read 9.25 K. Since the indicated temperature values did not change considerably during that minute, the start of phase transition was defined as the time when the first of the four temperature sensors crossed 9.25 K.

No RF test was performed after the cycle with the bandwidth measurement because the RF fields stored in the cavity could get trapped during phase transition, and thereby falsify the data set. For the same reason, no bandwidth measurement was performed during the initial and during the parked cooldown. Since also the beampipes, couplers etc. need to be cooled down in the vacuum during the initial cooldown, the phase transition could occur sooner than indicated by the Cernox sensors in this case.

An open question is also the influence of the helium vessel heads. They are fabricated from NbTi and provide the interface between the Nb cavity and the Ti tank. Assuming that the temperature difference between Ti-NbTi and NbTi-Nb junctions was much smaller than the difference between the two ends of the whole system, their impact was neglected. Finally, the difference from the bottom to the top must be considered. Since the bottom of the tank starts to collect the LHe first, the Ti-Nb (or Ti-NbTi-Nb) transition there will be colder than the transition at the top where also the heater is located.

Definition of the Temperature Difference

The thermocurrent value in the cavity-tank system corresponds to defined junction temperatures according to Section 2.4.2. However, neither the current nor the exact junction temperatures are known from the experiment as was previously discussed. Hence the RF data can not be correlated with either of them but only with an estimate of the joint temperatures, or their difference ΔT , based on the data of the Cernox sensors. Three different ways to define ΔT were used. An average value

$$\Delta T_{\text{av}} = \left| \frac{T_{\text{Cx1}} + T_{\text{Cx2}}}{2} - \frac{T_{\text{Cx3}} + T_{\text{Cx4}}}{2} \right|, \quad (3.3)$$

a minimum value

$$\Delta T_{\text{min}} = \begin{cases} \min(T_{\text{Cx1}}, T_{\text{Cx2}}) - 9.25 \text{ K} & \text{if Cx3 or Cx4 transitions first} \\ \min(T_{\text{Cx3}}, T_{\text{Cx4}}) - 9.25 \text{ K} & \text{if Cx1 or Cx2 transitions first} \end{cases} \quad (3.4)$$

or a maximum value

$$\Delta T_{\text{max}} = \max(T_{\text{Cx1}}, T_{\text{Cx2}}, T_{\text{Cx3}}, T_{\text{Cx4}}) - 9.25 \text{ K} \quad (3.5)$$

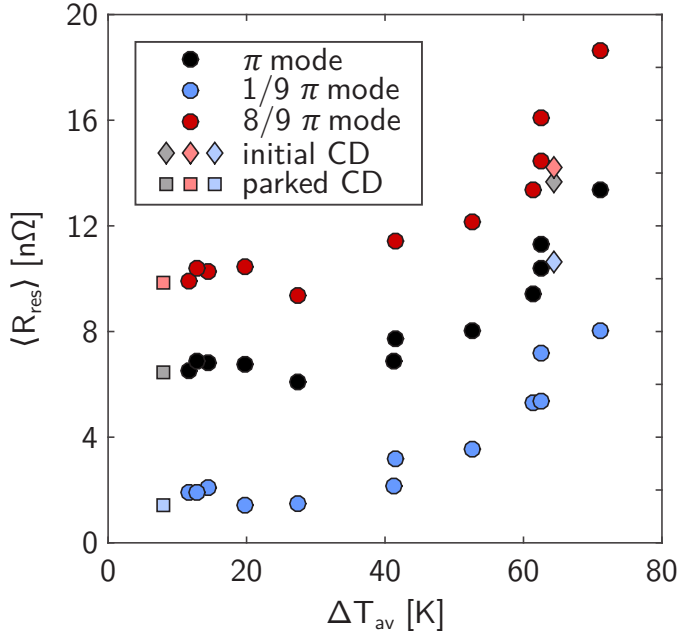


Figure 3.7: Average R_{res} measured in three passband modes as a function of the temperature difference along the cavity at the onset of superconducting phase transition.

when the first sensor reached T_c . The heat and charge currents and their driving force, the temperature gradient and the electric field, are directly linked via the equations for thermoelectricity (Equation 2.46). Hence the average temperature difference in Equation 3.3 is a good parameter to evaluate the average thermocurrent in the cavity-tank system at the onset of the phase transition. The estimated thermocurrent generates a magnetic field, which causes trapped flux and hence additional R_{res} . Figure 3.7 correlates ΔT_{av} for all cooldowns and cycles with the RF test results. Later, the other two ΔT estimations will also be correlated with the RF measurements. If all three ways to define ΔT lead to qualitatively similar results, the conclusions drawn from them are independent of the exact definition of ΔT , which means that the small number of temperature sensors does not prohibit to draw general conclusions for the whole system.

Figure 3.7 shows that phase transitions with lower temperature differences resulted in lower residual resistances. When ΔT_{av} was increased, R_{res} increased, too. In the best case, a residual resistance of $1.4 \text{ n}\Omega$ was achieved in the $1/9 \pi$ mode. This value is in good agreement with the vertical test result of $R_{\text{res}} = 1.2 \text{ n}\Omega$, which was reported in Section 3.3. Presumably, the residual losses are then dominated by the ambient magnetic field in HoBiCaT, which is about 0.2 to $0.5 \mu\text{T}$ (Figure 3.3) along the center cells causing a residual resistance of 0.7 to $1.75 \text{ n}\Omega$ [6]. Other, non-flux contributions may also add to the residual resistance.

The graphs of the three passband modes run parallel indicating that all nine cells,

or at least one half of the cavity since the modes are almost symmetric with respect to the mid plane (center of cell 5), are affected. The change in R_{res} appears to be a global effect consistent with the thermocurrent model. Furthermore, the $1/9\pi$ mode has a significantly reduced surface resistance compared to the two other modes while the residual resistance of the $8/9\pi$ mode is elevated. A possible cause is the increased ambient field in HoBiCaT near the end cells where the magnetic shielding is less effective.

Estimation of the ΔT Range

Figure 3.8 reproduces the data of Figure 3.7 with additional information. An error bar in ΔT was included. The minimum values for ΔT were calculated according to Equation 3.4, the maximum values according to Equation 3.5. Although the error bars are large, all nine $\langle R_{\text{res}} \rangle$ versus ΔT curves exhibit a similar behavior. To show that their characteristic shape is independent of the chosen definition of ΔT , it must be demonstrated that the curves are self-similar. Figure 3.9 shows the result of such an attempt where ΔT_{min} and ΔT_{max} were scaled with the factors $\Delta T = sc_{\text{min}} \cdot \Delta T_{\text{min}}$ and $\Delta T = sc_{\text{max}} \cdot \Delta T_{\text{max}}$ in order to obtain a common ΔT . ΔT_{av} was preserved $\Delta T = \Delta T_{\text{av}}$. Further, the R_{res} values were shifted by the offsets os_{π} , $os_{8/9\pi}$ and $os_{1/9\pi}$ for the respective modes. The offsets of the residual resistances were calculated as the mean of the values at low temperature differences where the thermoelectric impact was negligible ($\Delta T_{\text{av}} < 20$ K) yielding

$$os_{1/9\pi} = 1.76 \text{ n}\Omega, \quad os_{\pi} = 6.69 \text{ n}\Omega \quad \text{and} \quad os_{8/9\pi} = 10.19 \text{ n}\Omega.$$

The definition of the scaling factors was less straight forward. First, the relative deviations of ΔT_{min} and ΔT_{max} with respect to ΔT_{av} for each data point were calculated. Then, the average relative deviation was determined once for ΔT_{min} and once for ΔT_{max} . Here, the median was chosen over the mean to diminish the influence of outliers. Finally, all ΔT_{min} values were upscaled by the obtained factor of sc_{min} and all ΔT_{max} values were downscaled by the obtained factor of sc_{max} . The calculation can be summarized in two equations:

$$sc_{\text{min}} = 1 + \text{Median} \left(\frac{\Delta T_{\text{av}} - \Delta T_{\text{min}}}{\Delta T_{\text{min}}} \right) = 1.92,$$

$$sc_{\text{max}} = 1 - \text{Median} \left(\frac{\Delta T_{\text{av}} - \Delta T_{\text{max}}}{\Delta T_{\text{max}}} \right) = 0.64.$$

The resulting Figure 3.9 shows that the characteristic shape identified in Figure

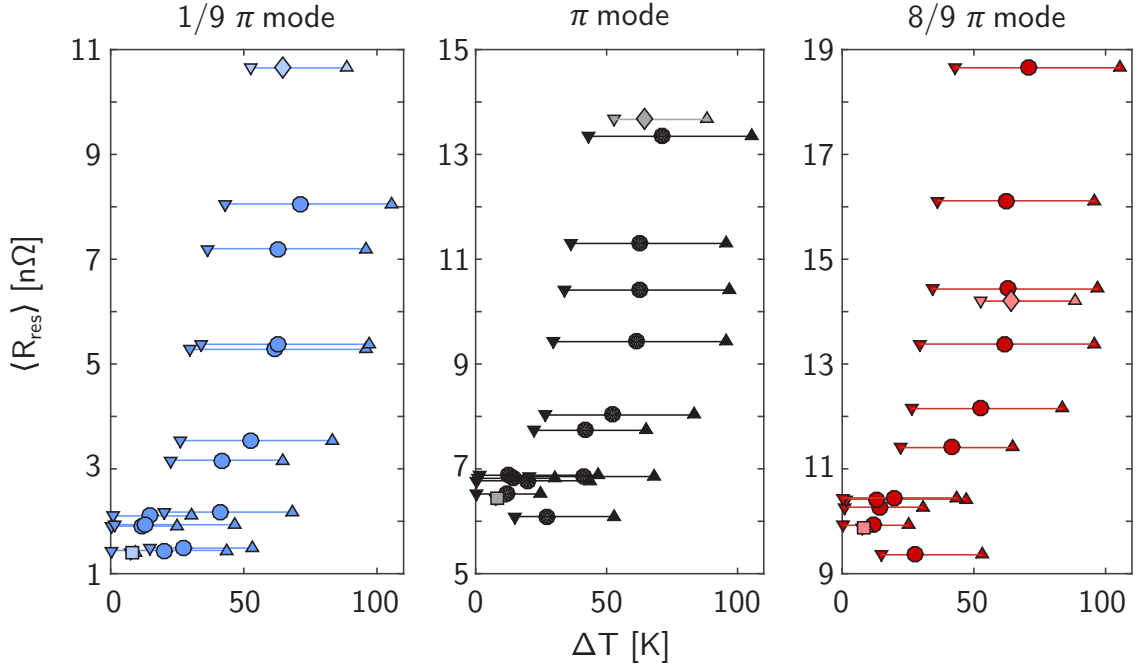


Figure 3.8: Residual resistance measured in the three passband modes as a function of ΔT_{av} (round marks), ΔT_{min} (downward-pointing triangle) and ΔT_{max} (upward-pointing triangle).

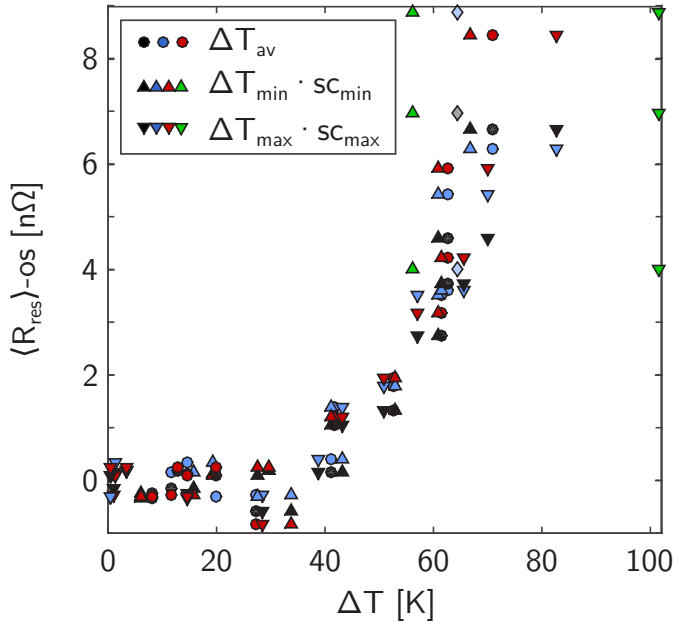


Figure 3.9: Shifted residual resistance values versus scaled temperature differences.

Annotation: The scaling factors for ΔT_{min} and ΔT_{max} were not successful for the initial CD. The six data points (R_{res} after initial CD in three modes vs. $\Delta T_{\text{min}} \cdot sc_{\text{min}}$ and $\Delta T_{\text{max}} \cdot sc_{\text{max}}$) deviate from the rest of the curve and are highlighted green.

3.7 does not depend on the chosen definition of ΔT , which is an important conclusion. Only the scaled data points obtained after the initial cooldown (green markers) deviate strongly from the curve. The scaling factors $s_{c_{\min}}$ and $s_{c_{\max}}$ do not yield reasonable results for this six points. The most likely cause of the deviation is the different cooling scheme of initial cooldown and thermal cycle. Thereby, the temperature distributions differed too much and the scaling factors, which were obtained mainly based on the data from the thermal cycles, fail on the initial cooldown. The non-scaled data points, however, fit within the curve.

We can conclude that the exact amount of thermocurrent in the system, which caused the extra losses, can not be obtained from the measurements. However, several qualitative statements can be made: All curves feature an almost constant resistance for low ΔT s (below 40 K). In the medium range (around 40 K), the resistance starts to increase. It seems that a new effect sets in. From that point on, the resistance is constantly increasing with temperature difference. The increase is probably caused by a thermoelectric contribution. If we assume that the temperature (and hence magnetic field) distributions are similar for all cycles, the shape of the curves should therefore resemble the underlying driving force, which is the thermopower of the involved materials. As will be shown later, the temperature dependence of the thermopower does indeed fit with the here presented RF data. For now, the discussion will end with this statement. It will be resumed later in Section 4.2.

3.3.3 Spatial Distribution of the Losses

The final section on the BCP cavity concerns the spatial distribution of the additional losses. Information on it can be gained by comparing the results for the different modes directly to each other. In Figure 3.10, the average residual resistances of the $1/9\pi$ and $8/9\pi$ modes is plotted versus the one of the π mode. A linear dependency is visible though the initial cooldown data point for the $8/9\pi$ mode does not fit into it. This might be explained by the fact that the cooling dynamics of the initial cooldown differ significantly from those of all other cooldowns. This can lead to a different, non-uniform spatial distribution of trapped flux. The data suggests, that less flux is trapped in the end cells after the initial cooldown compared to the thermal cycles with similar ΔT values.

Leaving out the $8/9\pi$ mode data point of the initial cooldown, two linear fits were applied to the two graphs in Figure 3.10. The resulting slopes are 1.0 ($1/9\pi$ mode) and 1.2 ($8/9\pi$ mode), which is also close to 1. This means that the thermocurrent does not just affect a small part of the cavity but more or less all cells. The result is

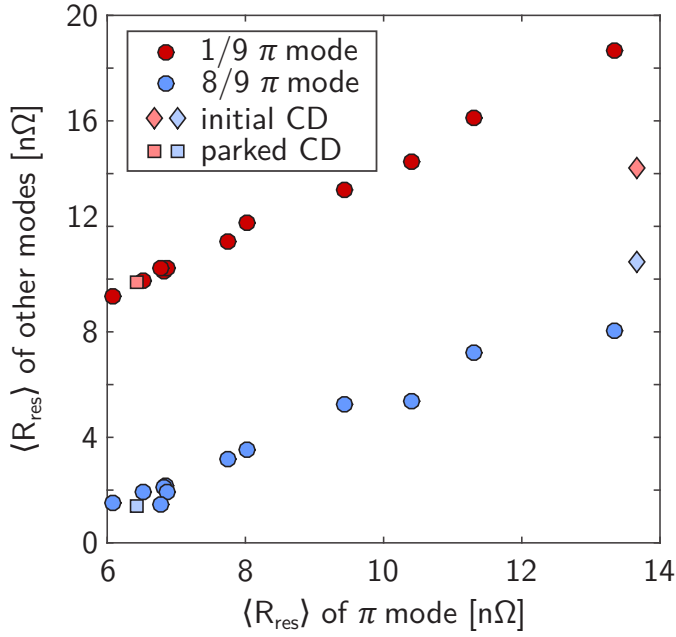


Figure 3.10: R_{res} for the $1/9\pi$ mode and $8/9\pi$ mode as a function of R_{res} obtained for the π mode.

as expected since the thermocurrent is present over the whole length of the cavity and the associated trapped magnetic flux hence adds some residual resistance to all cells. However, it must be taken into consideration that the modes are almost symmetric with respect to the middle plane (mid of cell 5). Hence, it cannot be stated if the additional losses are evenly distributed over the whole length of the cavity or only over half of it purely from the RF data. A linear increase of trapped flux over the length of the cavity, for example, would also lead to a slope of 1 in Figure 3.10. Additional experimental data, which resolves the issue, will be presented in Section 4.4.3.

Finally, the offset of the two curves must be addressed. The data shows that the longitudinal distribution of the residual losses is not uniform. The end cells exhibited higher dissipation compared to the middle cells. A likely explanation is the, already discussed, less effective magnetic shielding of the earth's magnetic field at the end cells. The increased ambient field is independent of the thermocurrents and hence consistent with the offset in Figure 3.10.

3.4 The N-Doped Cavity

In the basic principles chapter, Section 2.3.3, the losses caused by trapped flux were introduced together with a theoretical description. Equation 2.39 gave the dissipated power for the frequency range that is of interest here. It was briefly marked that the losses depend on several material parameters such as the penetration depth and the normal state resistivity. Recent experiments have shown that especially bulk niobium cavities with a reduced mean free path exhibit elevated dissipation from trapped flux [12]. That includes all cavities that were annealed with nitrogen to reduced their BCS losses, so-called N-doped cavities. The impact of thermocurrents on doped cavities must therefore be carefully analyzed.

This chapter presents a study similar to the one presented in Chapter 3.3 but conducted with an N-doped TESLA nine-cell cavity. The cavity was treated with a nitrogen doping technique at Fermilab ². In addition to the different treatment, the tank was also different. Helium inlet and the chimney to the two phase pipe were on the same sides. While this does not affect the RF surface, it does change the temperature distribution during cooldown and hence the magnetic flux generated by the thermoelectric effect. Furthermore, the cavity was equipped with a fixed input coupler at $Q_e \approx 3 \cdot 10^{10}$. The fixed coupling was problematic because the RF setup could not be optimized for a change in Q_0 . For quality factors that were significantly lower than $3 \cdot 10^{10}$, β became very small and hence the error in the RF measurement increased [51]. Further, a measurement in the $1/9\pi$ mode was not possible because the coupling was too weak.

In the π and $8/9\pi$ mode, the Q_0 of N-doped cavities exhibits a different dependence on E_{acc} compared to non-doped cavities. The Q_0 vs. E_{acc} curve of the BCP cavity in Section 3.3 was almost constant at low gradients and dropped quickly at the onset of field emission at higher gradients. The doped cavity, however, showed an increase of Q_0 with E_{acc} up to about 8 MV m^{-1} before it was decreasing again. The measurement was stopped at 19 MV m^{-1} to avoid a quench. This values were measured with lowest obtained residual resistance. The strong dependence of Q_0 on E_{acc} is caused by a change in the BCS resistance due to the doping [52]. For cycles, which resulted in elevated residual losses, the maximum vanished because R_{res} became the dominating term. Since this thesis investigates residual resistance, the data for the

²The used recipe was 60 min nitrogen annealing at 800°C with final $10 \mu\text{m}$ BCP. A comparison with Reference [12] suggests that this treatment should lead to a mean free path of about 30 nm with an increased sensitivity to trapped flux of $\approx 30 \text{ n}\Omega/\mu\text{T}$.

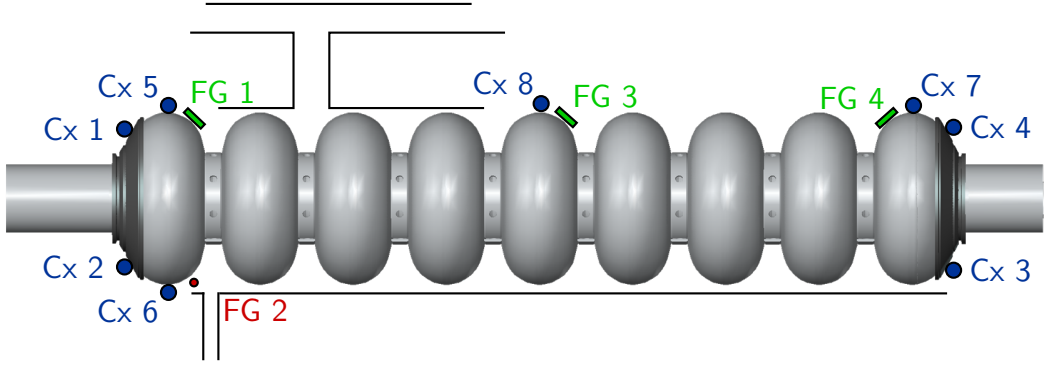


Figure 3.11: Positions of the temperature and magnetic field sensors.

π mode was obtained at a gradient of 8 MV m^{-1} where R_{BCS} had its minimum. The same was done for the $8/9\pi$ mode.

3.4.1 The BCS and the Residual Resistance

The extraction of the residual resistance was similar to Section 3.3. The annealing changed the surface layer of the niobium and the scattering characteristics in the now much dirtier material. The BCS parameters in the previously introduced fit function for the surface resistance as a function of temperature must be interpreted with special care, which is discussed in Reference [52]. For the extraction of the residual resistance, however, the function can still be used. The following fit parameters were obtained

$$\begin{aligned}
 a_{\pi} \cdot f^2 &= (1.25 \pm 0.21) \cdot 10^{-4} \Omega \text{ K}, \\
 b_{\pi} \cdot T_c &= (18.43 \pm 0.34) \text{ K}, \\
 a_{8/9\pi} \cdot f^2 &= (1.91 \pm 0.65) \cdot 10^{-4} \Omega \text{ K}, \\
 b_{8/9\pi} \cdot T_c &= (19.49 \pm 0.68) \text{ K}.
 \end{aligned}$$

In contrast to the BCP cavity, no general parameters for both modes were defined. The reason is that the doping procedure could yield a slight variation in the material parameters over the length of the cavity and hence different results for a and b can be obtained depending on the field distribution of each mode. As a result of the separate fits, the number of data points per BCS fit was smaller than for the BCP cavity and the error bars on a and b increased accordingly.

3.4.2 Correlation of Residual Resistance and Cooling Parameters

The temperature sensors on the tank were positioned as they were on the BCP cavity but five additional sensors were placed inside the tank on the cavity cells 1, 5 and 9. Further, four fluxgates (FGs) were mounted, one with azimuthal orientation and three along the cavity axis with a tilt corresponding to the cavity curvature. The positions are shown in Figure 3.11. The setup allowed to correlate the RF performance with the temperature distribution along the system as well as with the magnetic field inside the tank.

The cooldown and thermal cycles were executed similar to the previous test. The resulting R_{res} versus ΔT curve is shown in Figure 3.12. Again, ΔT was defined as the mean value according to Equation 3.3. The results agree qualitatively with the results of the BCP cavity. The characteristic shape discussed above appears again: At low ΔT values, the surface resistance is almost constant. In the $8/9\pi$ mode, R_{res} increases slightly for lower ΔT values. The doped cavity and the BCP cavity perform comparably. The best obtained R_{res} values in the π mode are almost identical for both cavities (6.4 n Ω for BCS cavity and 6.5 n Ω for N-doped cavity). For the $8/9\pi$ mode, the doped cavity achieves an optimum of 8.3 n Ω , which is even lower than the best value of the BCP cavity (9.9 n Ω).

At a medium difference around 40 K, the resistance starts to increase. Again, it seems that a new effect sets in. From that point on, the resistance is constantly increasing with temperature difference. This increase is more pronounced compared to the BCP cavity. While the additional residual resistance due to thermocurrents was a about 10 n Ω in the BCP cavity tests, the thermocurrent contribution in the N-doped cavity is about 20 n Ω , which is twice as much. This results confirms the assumption that the increased R_{res} originates from trapped flux whose impact is greater in doped cavities. The same ΔT in the two cavities should generate a similar amount of magnetic field. The power dissipated in the doped cavity, however, is increased due to the reduced mean free path and the associated high sensitivity to trapped flux.

The second plot in Figure 3.12 shows the residual resistance in the $8/9\pi$ mode versus the one of the π mode. A linear regression yields a slope of 1.1. The linear dependence (with a slope close to 1) was already found in the tests with the BCP cavity and reappears here.

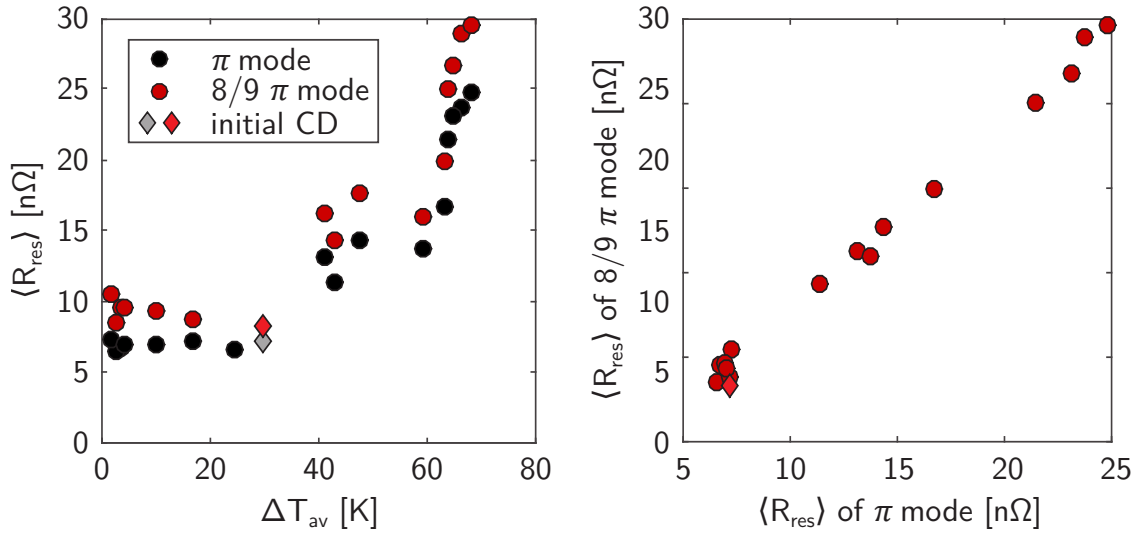


Figure 3.12: Residual resistance measured in two passband modes as a function of the temperature difference along the cavity in an N-doped cavity.

3.4.3 Correlation of Residual Resistance and Directly Measured Magnetic Field

The magnetic field diagnostics inside the tank of the doped cavity allowed for additional analysis of the system. The uppermost panel of Figure 3.13 displays the temperature over time measured at the cavity and at the tank during the initial cooldown and during Cycle 12. The middle panels show the average temperature difference, which is the driving force of the thermocurrent. The bottom panels display the data of the fluxgates. The sensors, which were oriented along the cavity, read only low values corresponding to the shielded earth's magnetic field. When the material close to the sensor transitioned, a step-like change in magnetic field caused by the Meissner effect was visible. Fluxgate 2 (FG2), however, was oriented in a suitable direction to pick up the azimuthal fields from the thermocurrents.

In the data of the initial cooldown, it is nicely visible how a magnetic field of up to $18 \mu\text{T}$ was generated by thermoelectric effect. The average temperature difference decreased with time and so did the magnetic field, which was driven by it.

The data of the thermal cycles was less easy to interpret. During all cycles, FG 2 picked up an increase in magnetic field due to thermocurrents but, in addition, also a peak prior to the superconducting phase transition. The peak occurred within a minute before the transition, while the temperature difference over the system remained almost constant, as displayed in Figure 3.13 for Cycle 12. The peak did therefore not correspond to a change in temperature difference.

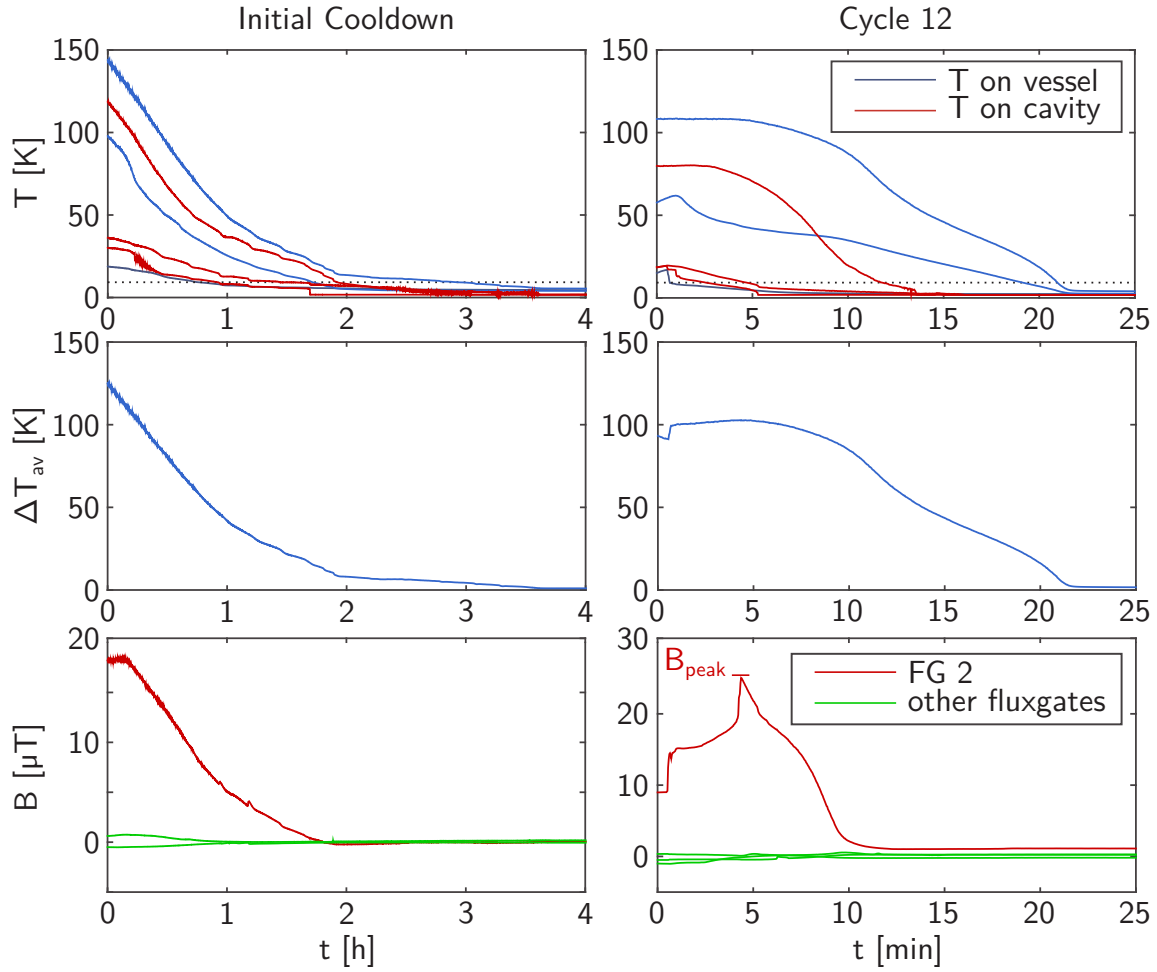


Figure 3.13: Temperature and magnetic field data during the cooldown and Cycle 12.

However, as Figure 3.14 shows, the height of this magnetic field peak B_{peak} was clearly correlated with the residual resistance. A linear regression was performed on the data set based on Equation 2.41, which states that the surface resistance caused by trapped flux increases linear with magnetic field. Data points, which were obtained after cycles with low temperature differences, were excluded from the fit. Their B_{peak} values were well below $1 \mu\text{T}$ and no thermoelectric loss contribution was expected for those cycles. The measured magnetic field mainly originated from the shielded earth magnetic field and the peak was caused by the associated flux expulsion during the sc phase transition. This is a completely different effect than the peak observed for high ΔT values.

The linear regression yields a slope of $0.78 \text{ n}\Omega/\mu\text{T}$. This number is very specific for the position and orientation of FG2 and can therefore not be compared to experimental findings of other groups and experiments (like the typically used rule of thumb

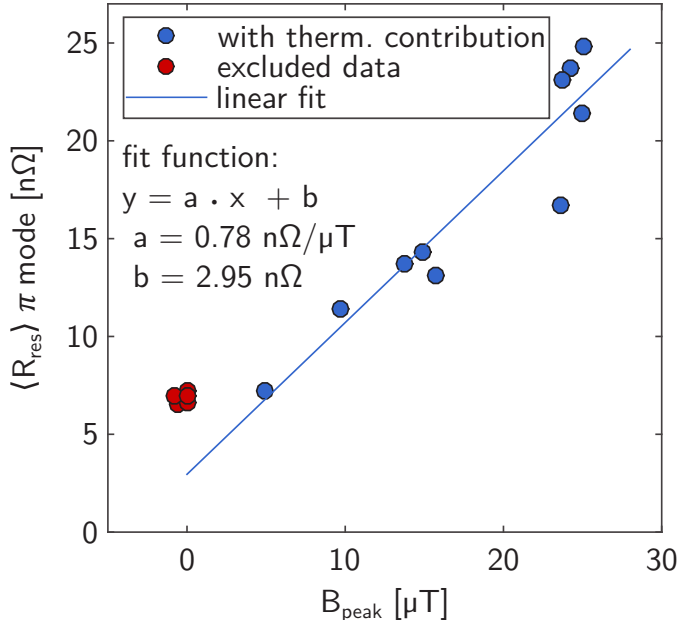


Figure 3.14: Residual resistance as a function of the peak magnetic field. The red data points were excluded from the fit. The parameters b and c account for the fact that, with out thermoelectric contribution, neither the ambient magnetic field nor R_{res} was zero.

that $1 \mu\text{T}$ of trapped flux causes $3.5 \text{ n}\Omega$ additional residual resistance). However, the fit shows that the linear relation between magnetic field and surface resistance given in theory (Equation 2.41) applies to the system and therefore it is the first, though weak, direct link between temperature difference, magnetic field and RF losses.

Finally, the origin of the peak must be discussed. As mentioned above, it was not caused by a change in temperature difference. Since it coincided with the sc phase transition, the peak in magnetic field was likely caused by the appearance of areas with zero DC resistance close to FG2. The thermoelectric current was drawn into the newly established superconducting path and a high current density was reached. The magnetic field was focused correspondingly and FG2 measured an increase in magnetic field. Once the superconducting area grew, the current density decreased and the measured value dropped again. Simulations that substantiate this model will be shown in Section 4.3.2.

The statements based on the here presented data are not very strong because the probes measured only the local magnetic field. A general understanding of the thermocurrent distribution and change can scarcely be gained. Therefore, the subsequent chapter will address simulations that can yield a more complete picture.

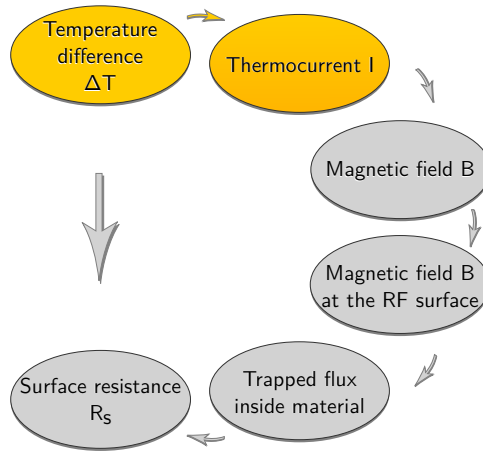
Chapter 4

Estimate of Thermoelectrically Generated Magnetic Field

The experimental findings presented in the previous chapter suggest a reversible contribution that causes additional residual resistance. The next sections test the thermocurrent hypothesis presented in Section 2.4 as possible explanation for the observed variation in R_{res} .

The most important material properties in this context are the electrical resistivity and the thermopower. We show that S for our system is in the order of a few $\mu\text{V K}^{-1}$, which is enough to generate a magnetic field of several μT at the RF surface. This field is sufficient to explain the previously presented changes in surface resistance. Numerical simulations of the cavity-tank system allow for a quantitative analysis of the thermocurrents and the generated magnetic fields and in particular the field distribution. Temperature-dependent material properties are used to yield reliable numbers on the amount of magnetic flux, which is to be expected on the RF surface.

4.1 The Thermopower



The thermopower S , also known as Seebeck coefficient, was introduced in Section 2.4. In short, it is the material property that measures the magnitude of a generated thermoelectric voltage in response to a temperature difference across a material. It depends on the carrier occupation of the electronic band structure and hence changes with temperature.

4.1.1 The Thermopower in Literature

In the scope of this chapter, the thermopower of niobium and titanium below 100 K is of interest. The data known from literature is limited due to several reasons. The most common application of the thermoelectric effect is the thermocouple, a device for measuring temperature. Also of relevance are devices that use the reverse thermoelectric effect and convert heat back into electrical power (thermoelectric coolers or generators). The ability of a given material to efficiently produce thermoelectric power is proportional to the Seebeck coefficient squared and hence a high S is desirable. There are materials with S values of several hundred $\mu\text{V K}^{-1}$ and even silicon has an S of more than $400 \mu\text{V K}^{-1}$. The thermopower of niobium and titanium is below $10 \mu\text{V K}^{-1}$.

Furthermore, most applications use the materials in a region where S is proportional to the temperature. These linear regions usually occur at high temperatures. For titanium, it starts at 400 K. The linear region of niobium is between 600 K and 1400 K. All in all, the interest in niobium or titanium with their comparatively low thermopowers, especially at cryogenic temperatures, was little [42].

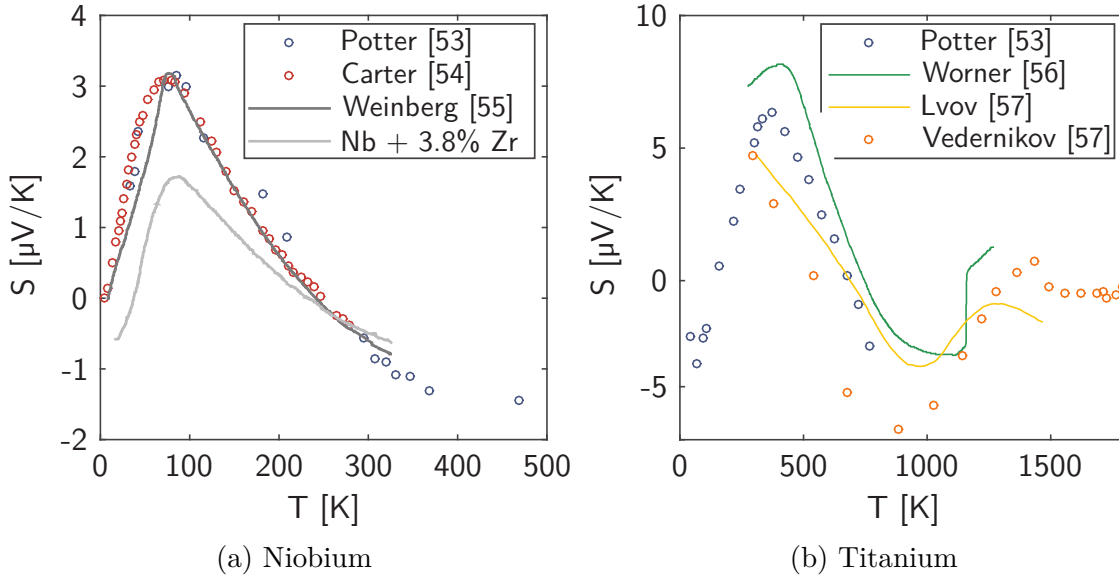


Figure 4.1: Literature values for the thermopower of Nb and Ti: a) Values for niobium given in References [53, 54, 55]. The light grey line is the data for a niobium-zirconium alloy from Reference [55]. The measurement of Reference [54] was performed on 99.99% pure Nb. b) Values for titanium extracted from References [53, 56, 57].

The literature data we were able to find is summarized in Figure 4.1. One of the first studies on transition metals was performed by Potter in 1944 [53]. However, the publication gives no information on the sample purity or crystal structure. Later studies provide at least a purity, like the value of 99.99% in Reference [54]. A study performed by Weinberg et. al. [55] presented data on niobium-zirconium alloys and lead to the conclusion that the purity of the material can influence the thermopower under certain conditions. The niobium data of References [53, 54, 55] is summarized and reproduced in Figure 4.1a.

Most of the data for titanium was measured at high temperatures. Combining the available literature, a general impression on the data below room temperature can be gained. However, a large scatter remains and only the data of Potter gives values below 250 K [53, 56, 57]. The literature data is summarized and reproduced in Figure 4.1b.

In conclusion, the available literature did not give solid enough information for the numerical simulations of the cavity-tank system. Hence it became inevitable to perform independent measurements of the thermopower of niobium and titanium below room temperature.

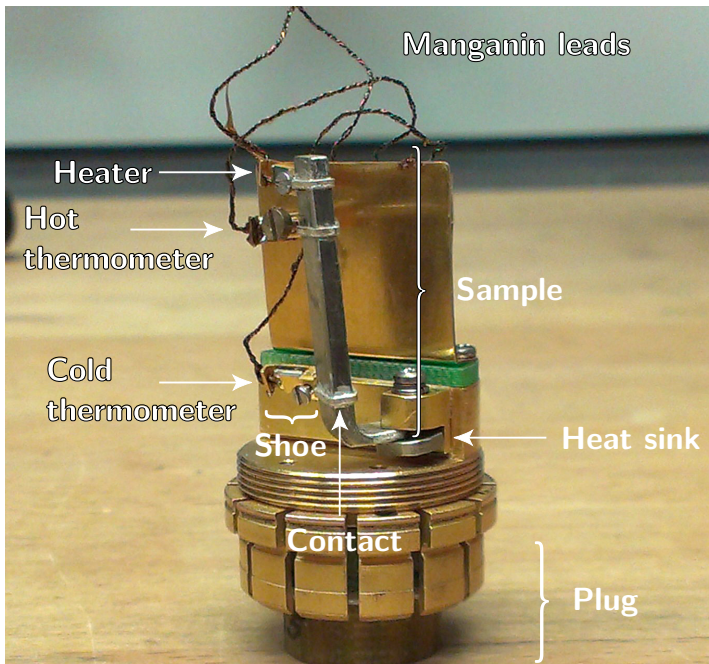


Figure 4.2: A PPMS sample, size $2\text{ mm} \times 5\text{ mm} \times 30\text{ mm}$, mounted to the thermal transport option. Three contacts, one for the heater and two for the thermometers are glued to the sample with silver epoxy. The heater imposes a temperature gradient on the sample, which is measured by the thermometers. An additional pin at the thermometers reads the voltage that is generated by the thermoelectric effect. The plug connects the wires to the read out electronics.

4.1.2 The Thermopower Measurement Setup (PPMS)

The group for experimental infrastructure at HZB is equipped with a commercial system for the evaluation of material properties at low temperatures. The system is called Physical Properties Measurement System (PPMS) and was fabricated by Quantum Design¹. It is designed to perform automated measurements at variable temperature and ambient magnetic field. The system consists of a cryostat and a high vacuum sample chamber where different sample plugs can be inserted. Quantum Design provides a plug for thermal transport measurements, the so-called thermal transport option², which allows high precision measurements of the thermopower, the thermal conductivity and the electrical resistivity over a wide temperature range. Figure 4.2 shows a photo of the thermal transport option with an installed niobium sample. Several niobium and titanium samples with different purities and dimensions were tested. The next sections briefly describe the software that comes with the system and the underlying data analysis. More detailed information on the hard- and software can be obtained the PPMS thermal transport option manual [58].

¹www.qdusa.com/sitedocs/productBrochures/1070-002.pdf

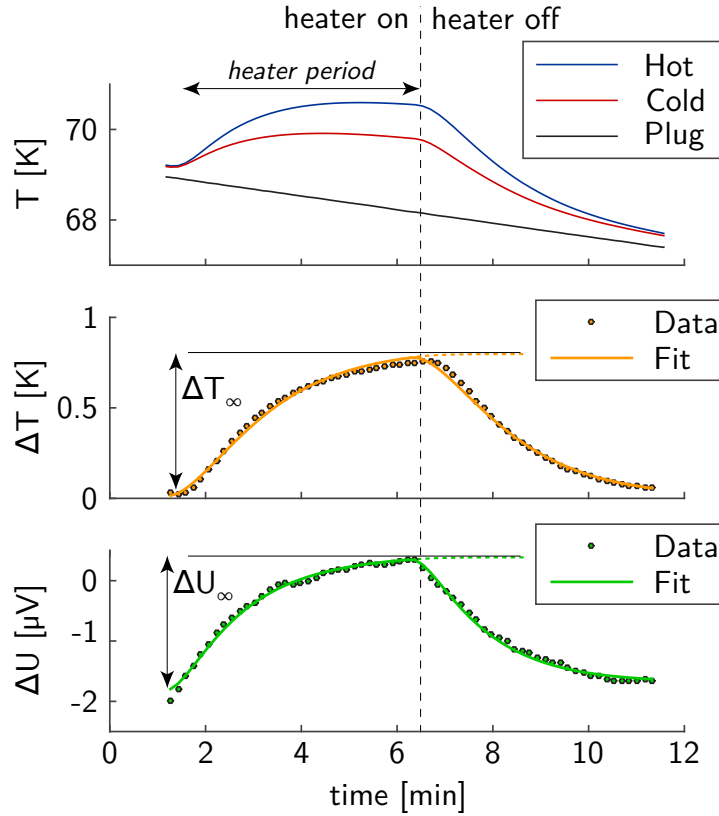
²http://www.qdusa.com/sitedocs/productBrochures/tto_rev7-06.pdf

Figure 4.3: PPMS temperature and voltage response to a heater pulse at the hot and the cold thermometer.

Top panel: Time trace of the thermometers during one heat pulse. The plug temperature was measured with an additional thermometer

Middle panel: Temperature difference ΔT across the sample with the estimate of the asymptotic differential ΔT_∞ .

Bottom panel: Seebeck voltage response with the respective differential ΔU_∞ .



4.1.3 Software and Data Analysis

The measurement software that controlled the test and analyses the data on the fly was included in the PPMS system. The output file contained the time stamp, sample temperature and the material properties, in the case of the thermal transport option thermopower, thermal conductivity and electrical resistivity.

The system set a power and period for the heater. The thermometers recorded the temperatures and the voltages at the two contacts during the heating time and during the subsequent cool down period. The data was fitted based on an empirical formula [58]. Figure 4.3 displays a typical example for temperature and voltage signals together with the fit functions. The modeled curves yielded the asymptotic temperature and voltage drop, ΔT_∞ and ΔU_∞ . The thermopower was calculated from these extrapolated values.

The system corrected for the Seebeck voltage that occurred on the manganin leads, which connected the thermometers to the connector plug. The leads had a thermopower that was referenced to be $\approx 1 \mu\text{V K}^{-1}$ or smaller at any temperature. This value was considered small compared to most thermoelectric materials but for niobium and titanium it was in the order of the measurement value.

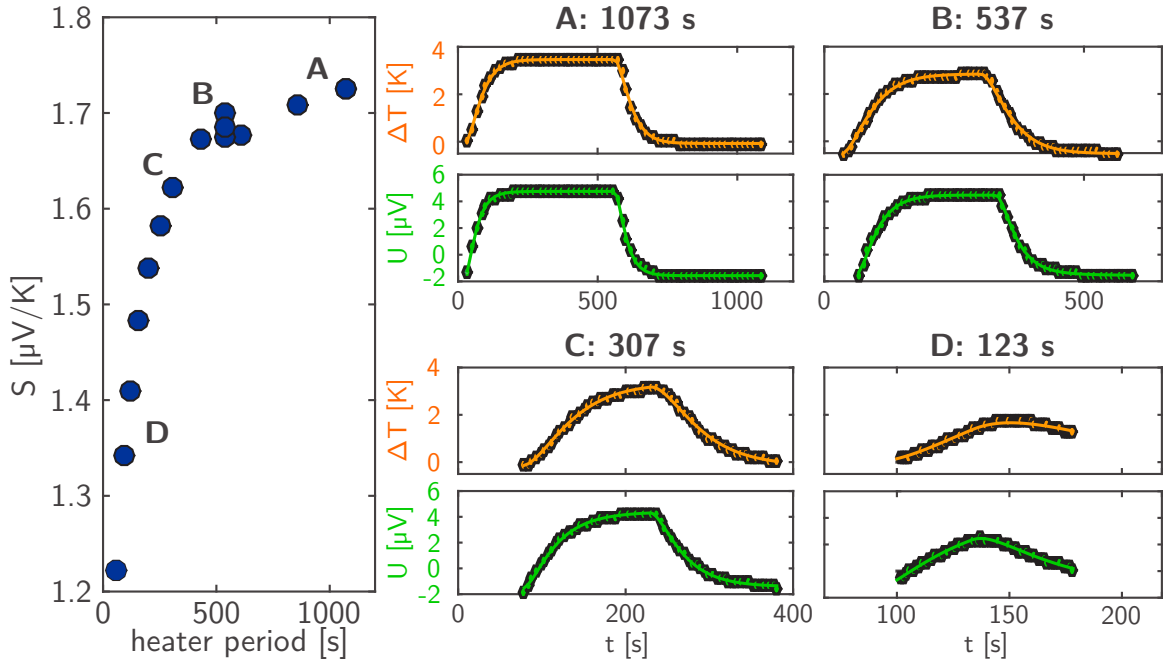
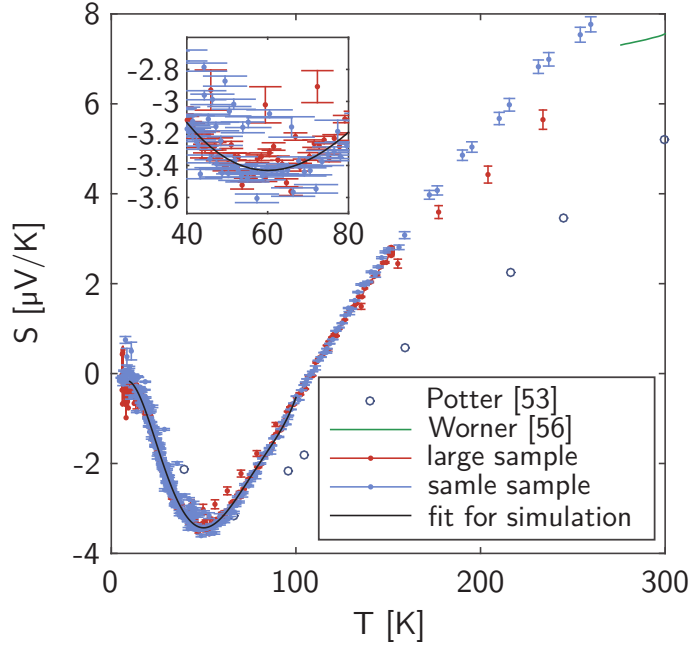


Figure 4.4: PPMS data for a niobium sample at 150 K for four different heater periods A to D. The left panel shows the thermopower S as a function of the heater period. The right panels show the underlying temperature and voltage data.

During a PPMS test, the sample cooled to a predefined temperature with a given cooling rate (e.g. to 50 K with 0.5 K min^{-1}) while the material parameters were continuously measured. The PPMS software automatically adjusted the heater power and the heating period to optimize the fits. Several tests indicated that a well chosen combination of heater power and heating period was essential for a result.

Figure 4.4 shows data, which was acquired with a constant heater power and various heater periods for a niobium sample at 150 K. The fit parameters ΔT_∞ and ΔU_∞ were well defined for the heating period of 1430 s (maximum period provided by the system). When the period was reduced, the measured thermopower decreases. There was no underlying physical explanation for the effect hence it was concluded that the reduction was an artifact of the measurement. It emerged that the shorter periods changed the shape of the temperature and voltage pulses. Figure 4.4 shows that the fits are still acceptable, even for short heater pulses. Yet, it is reasonable to assume that the errors on ΔT_∞ and ΔU_∞ , are increased for shorter pulses. Probably one or even both parameters were systematically over- or underestimated. The origin of the effect was not unmistakably identified because of the proprietary software, which did not allow access to every step of the calculation. Several tests however reproduced the up to 30% reduction of measured thermopower for too short pulses.

Figure 4.5: The thermopower of the titanium samples with 10.51 mm^2 cross section (large sample), 4.58 mm^2 cross section and the literature data of references [53, 56]. The black line shows a polynomial fit of the data that was later used for numerical simulations.



Thus only results obtained with long enough heater periods are presented hereafter. The needed minimum heater period to achieve a sufficient curve was about 800 s for the here shown example (Figure 4.4) and decreased towards lower temperatures due to the reduction in heat capacity.

4.1.4 Results

Titanium

The PPMS measurements on titanium were performed on two samples:

- “large”: 10.5 mm^2 cross section ($\approx 2 \times 5 \text{ mm}^2$), 30 mm total length, grade 2
- “small”: 4.6 mm^2 cross section ($2 \times 2.3 \text{ mm}^2$), 30 mm total length, grade 2

Figure 4.5 shows the measured thermopower S as a function of temperature. The samples were cooled and warmed up several times while the thermopower was continuously measured. The acquired data shows reasonable accordance with the literature given the fact that Reference [53] does not provide details on which type of titanium was used. Furthermore, it must be stressed that no literature values below 40 K were available to compare the measurements to. The experimental data between 10 K and 100 K was fitted with a polynomial to generate a material data file that was later used in the numerical simulations. Table D.1 in the Appendix presents the resulting numbers.

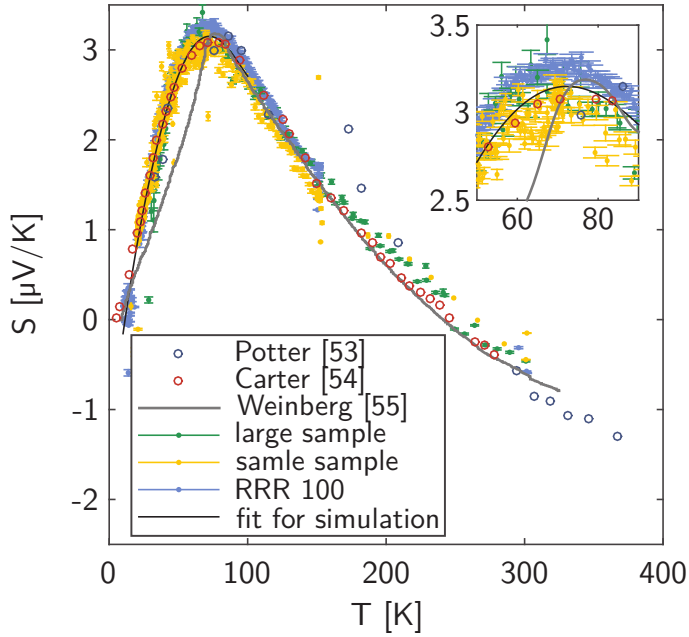


Figure 4.6: The thermopower S of the three niobium samples with 10.51 mm^2 cross section and RRR300 (large sample), 4.58 mm^2 cross section and RRR300 (small sample) and 1 mm^2 cross section and RRR100 together with literature data of References [53, 54, 55]. The black line shows the polynomial fit that was later used for numerical simulations.

Niobium

The PPMS measurements on niobium were performed similar to the titanium tests and on three samples:

- “large”: 10.5 mm^2 cross section ($\approx 2 \times 5 \text{ mm}^2$), 30 mm total length, RRR300 material provided by Heraeus
- “small”: 4.6 mm^2 cross section ($2 \times 2.3 \text{ mm}^2$), 30 mm total length, RRR300 material provided by Heraeus
- “RRR100”: 1 mm^2 cross section ($1 \times 1 \text{ mm}^2$), 15 mm total length, RRR100, sample provided by CERN

The acquired data is presented in Figure 4.6. It is in good agreement with the literature, especially with the data of Carter et. al. in Reference [54]. The experimental data between 10 K and 100 K was also fitted and the numbers are available in Table D.1 in the Appendix.

4.2 The Thermovoltage as a Function of Temperature

With the newly found material data, a previously paused discussion can be resumed. In Section 3.3.2, the additional surface resistance caused by thermocurrents was discussed as a function of temperature difference along the cavity-tank system. A characteristic shape was found in Figure 3.9 for the BCS cavity and was reproduced in Figure 3.12 for the N-doped cavity. Assuming that the resistance increase is caused by thermocurrents, the origin of the shape must lie in the temperature dependence of the thermopower, which is now known.

Based on Equation 2.45, the integral over the thermopower values can be calculated. It is bounded by the lower limit, which is fixed to $T_c = 9.25$ K, and the upper limit T_2 , which increases with ΔT . Figure 4.7 shows the result of the integration together with the experimental data of Figure 3.9. As was discussed above, the definition of ΔT in the experiment did not influence the shape of the curve significantly.

Based on the argument that ΔT from the experiments can be scaled without compromising the physics, the two abscissa in Figure 4.7 were set in a way that the thermovoltage matched the data. The increase in surface resistance is in reasonable agreement with integral over the thermopower. At low ΔT values, however, the curves separate. This can be explained by sources of residual resistance other than thermoelectrically generated trapped flux, which amounted to ≈ 5 n Ω (in the π mode) and dominate in that region. We can conclude that the increase in surface resistance found in the experiments can be attributed to the underlying temperature dependence of the thermopower values.

Furthermore, the results fit with the measurements of Eichhorn et. al who found a similar increase of R_{res} with temperature difference but for smaller ΔT values [59].

However, one aspect, which is not included here, is the temperature dependence of the thermal conductivity. The trapped flux is generated by the current in the system and not the voltage. A higher T_2 coincides with a locally increased resistance and hence a lower current (and magnetic field). This is not regarded in Figure 4.7. Further information on its influence can be gained from numerical simulations, which include both temperature-dependent properties, the thermovoltage and the thermal conductivity.

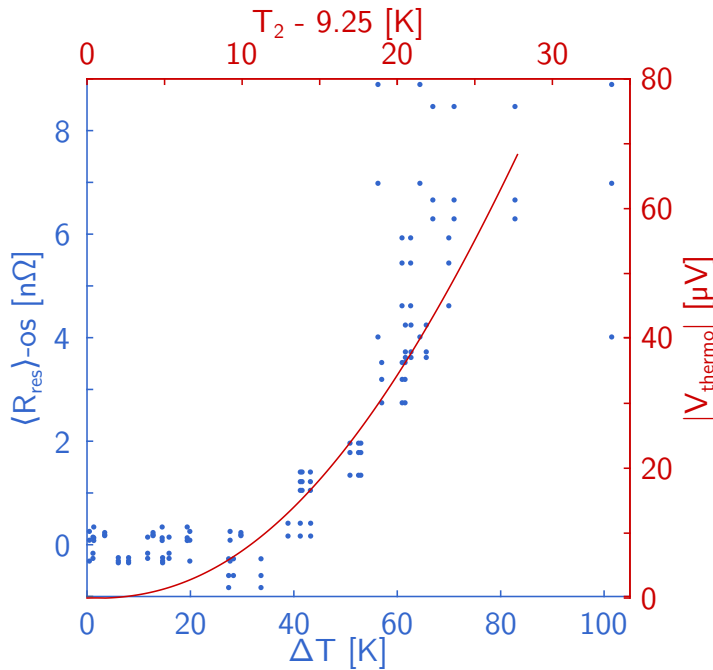
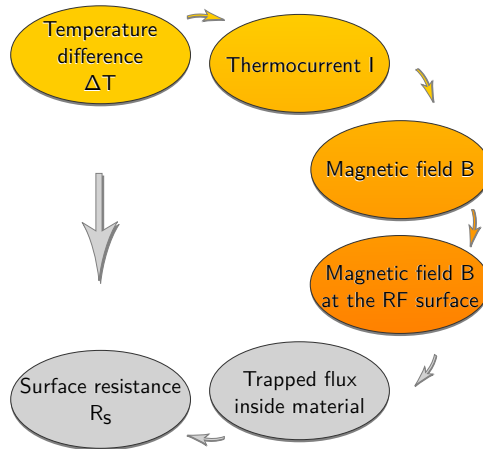


Figure 4.7: The experimental data of Figure 3.9 with the integrated thermovoltage that was calculated based on Equation 2.45 and the material data in Section 4.1.4.

4.3 The Thermocurrent and Its Magnetic Field



The PPMS measurements and the thermovoltage calculation in the previous section yielded thermopower values in the order of a few $\mu\text{V K}^{-1}$, at most about $50 \mu\text{V}$ for high temperature differences. On first glance, that might not seem significant. However, the low resistance of the system due to the large cross sections of the cavity and the tank combined with the high temperature differences during a rapid cooldown may result in noticeable thermocurrents. Their amount can be calculated based on the thermoelectric transport equations presented in Section 2.4.2. The system of coupled differential equations must be solved including the temperature-dependent material parameters. Furthermore, the spatial distribution of the thermocurrent is

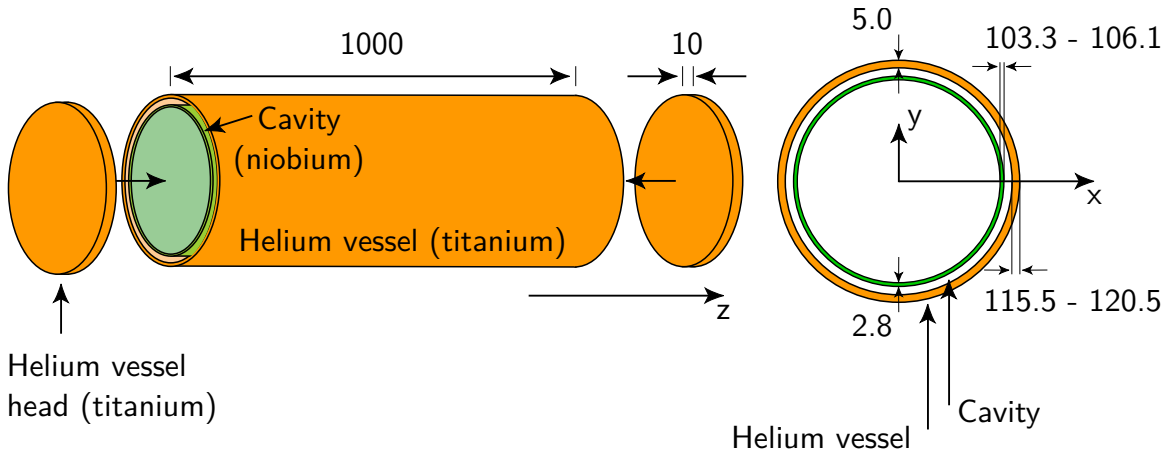


Figure 4.8: Simplified geometry for numerical simulations. All dimensions are in mm. The green inner cylinder represents the cavity and was defined as niobium. The orange parts that represent the tank were defined as titanium.

important because it determines the spatial distribution of the magnetic field. Due to these different contributions to the problem, a numerical approach was chosen over an analytical. The cavity-tank system was implemented in the code Comsol to understand the amplitude of the thermocurrents and the geometry of the associated magnetic field. The simulations were performed in two steps. First, the setup was simplified to a set of coaxial cylinders in order to single out the thermoelectric effect in the coaxial geometry of cavity and tank. Second, further influences as for example the magnetic shielding and the exact cavity geometry were included to generate reliable numeric values that can be compared to the experiments.

4.3.1 Thermocurrent: Simulation of Two Coaxial Cylinders

For a start, the cavity with was replaced by a hollow cylinder. A second cylinder representing the titanium tank was coaxially placed around it and the system was closed with disks on both ends. This simplified model together with its dimensioning is shown in Figure 4.8. The inner cylinder, which represents the cavity, had the typical cavity wall thickness of 2.8 mm and the outer cylinder with the two end plates resembled the helium vessel and vessel heads. They were defined as titanium with a thickness of 5 mm (vessel) or 10 mm (vessel heads). The 1 m length of both cylinders was chosen as the approximate length of a TESLA cavity. The space between the cylinders was filled with helium gas for heat transfer. The model exhibited perfect cylindrical symmetry.

For the numerical simulation, temperature-dependent material properties were

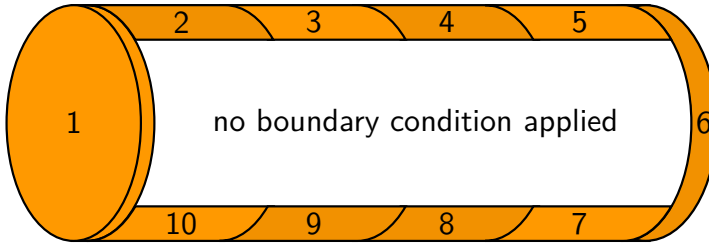


Figure 4.9: The different areas on the outside of the tank, on which thermal boundaries could be applied in the Comsol simulations. No fixed boundary conditions were applied to the rest of the setup.

needed. The literature data for the temperature-dependent electrical conductivities and heat capacities is given in References [3, 60, 61]. The thermal conductivity was set constant to improve the convergence of the simulations. Based on the References [60, 61, 62], $\kappa_{\text{Nb}} = 50 \text{ W m}^{-1} \text{ K}^{-1}$ and $\kappa_{\text{Ti}} = 22 \text{ W m}^{-1} \text{ K}^{-1}$ were chosen as approximations.

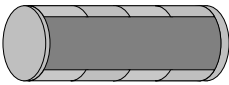
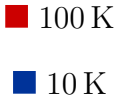

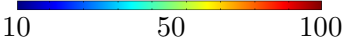
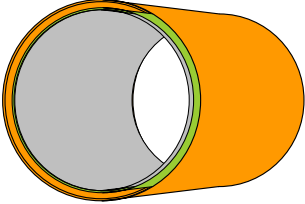


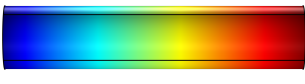
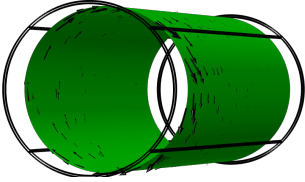

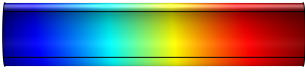
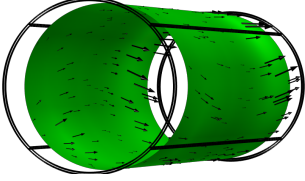
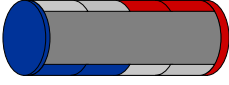
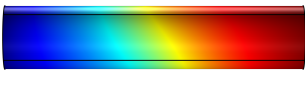
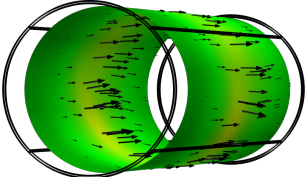

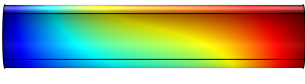
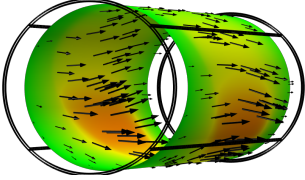

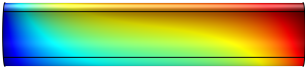
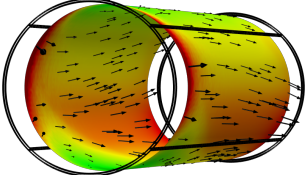
The simulations were performed as five separate studies. In each study, different temperature boundary conditions were applied with an increasing degree of temperature asymmetry. For that purpose, ten areas were defined on the outer surface of the tank as shown in Figure 4.9. Each area could either be assigned a fixed temperature or left undefined as the rest of the setup. Thereby, the temperature asymmetry from the experimental situation was simulated. Table 4.1 shows the number of the study in the first column and the boundary conditions that were applied to the tank in the second column. Column three displays the resulting temperature distribution in the cavity wall and column four shows the magnetic field at the RF surface.

The thermoelectric current that flowed in the system was defined by the material properties and the temperatures of the joints of the two metals. The joints were the areas 1 and 6 shown in Figure 4.9. For all simulations, area 1 was set to 10 K and area 6 was set to 100 K. Hence the driving force was the same for all simulations and only the asymmetry changed. In Study 1, the isothermals were perpendicular to the cylinder axis. The resulting current distribution was cylindrically symmetric and the magnetic field on the RF surface was zero and exhibited a rapid increase inside and beyond the cavity wall. The field had only an azimuthal component. The situation is as expected from Ampère’s Law. In the Studies 2 to 6, the areas 2 – 5 and 7 – 10 were assigned fixed temperatures as well, leading to asymmetric temperature distributions. Since the electrical resistance in turn depends on temperature, the electrical symmetry was broken.

Table 4.1 displays cuts in the xz plane of the temperature distributions inside the cylinders. The increasing asymmetry imprinted on the tank tilted and distorted the isotherms in the inner cylinder and created a top-bottom temperature gradient in addition to the left-right gradient. Furthermore, the table shows the solution for

4. Estimate of Thermoelectrically Generated Magnetic Field

Table 4.1: Results of the simulations: Second column displays the given boundary conditions at the outer surface of the outer cylinder. The third column shows the temperature in the wall of the inner cylinder and the fourth column shows the resulting magnetic field at the RF surface. The small figures in the top row display the angles of view for the temperature and the magnetic field distribution. The grey cylinder in the picture of the magnetic field indicates the RF surface.

Study	Boundaries outside	T [K] distribution along "cavity"	B [μ T] distribution at RF surface
	 	 	 
1			
2			
3			
4			
5			

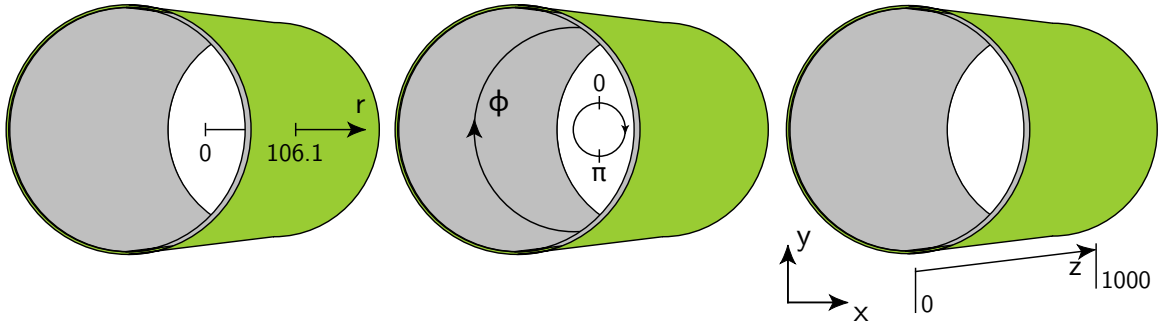


Figure 4.10: Coordinates for exporting the magnetic field distribution.

the magnetic field inside the cylinders close to the RF surface. The RF surface was at a radius of $r = 103.3$ mm. Since the numerical simulation employed a limited number of mesh cells, the field calculated directly at $r = 103.3$ mm could correspond to the field inside the cylinder or inside its wall. The magnetic field was therefore exported at $r = 102$ mm to prevent falsified data due to meshing. The arrows in the figures display the direction of the magnetic field at $r = 102$ mm and the arrow size is proportional to the field strength.

For further and more quantitative analysis, the magnetic field was exported. Figure 4.10 shows the used cylindrical coordinates. Figure 4.11 displays the absolute magnetic field in r direction at $z = 500$ mm and $\phi = \pi/2$ as a cut through the two cylinders. In the symmetric case, the magnetic field is only present between the cylinders and inside the cylinder walls. No field penetrates the inside of the inner cylinders or reaches beyond the outer wall of the tank. The field reaches its maximum at the outer surface of the inner cylinder. From there, it decreases in both directions until it reaches zero at the inner surface of the inner cylinder and the outer surface of the outer cylinder. For Studies 2 to 5, the increasing asymmetry of the current density leads to an increased magnetic field inside the cylinders and especially at the RF surface. If this field gets trapped during superconducting phase transition, it increases RF dissipation as was observed in the experiments.

The right hand side of Figure 4.11 shows the magnetic field at $z = 500$ mm and a fixed radius inside the vacuum space ($r = 102$ mm) versus the angle ϕ . It exhibits minima at the top and bottom of the system ($\phi = 0$ and $\phi = \pi$) but is non zero everywhere. These positions correspond to the regions of fixed boundary temperatures that cover a $\pi/2$ angle at the top and bottom of the outer cylinder surface.

Figure 4.12 shows the magnetic field along the z axis at $r = 102$ mm and $\phi = \pi/2$. It also displays the temperature difference between top and bottom of the inner

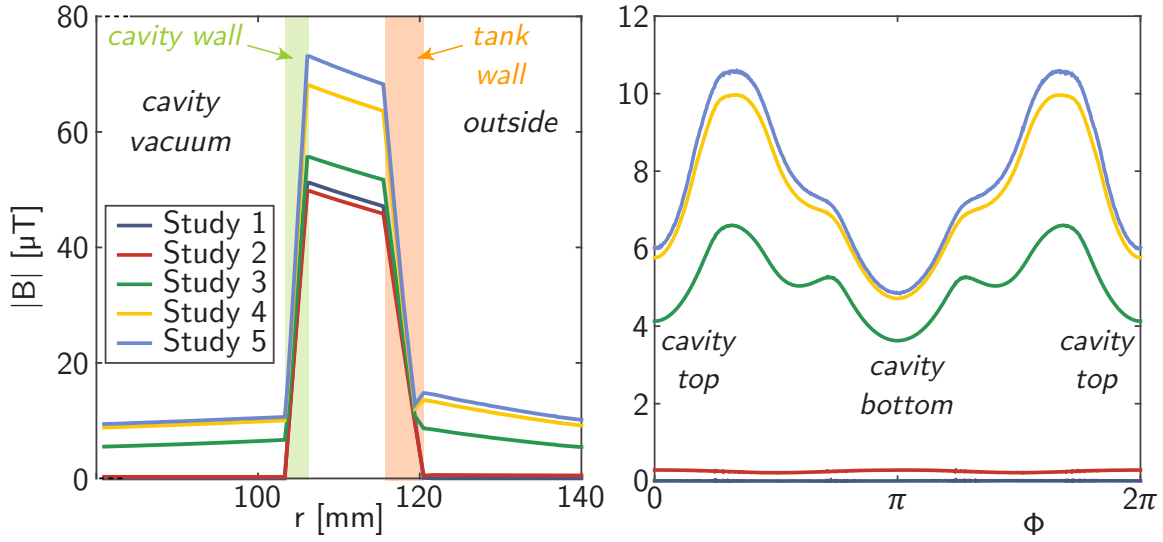


Figure 4.11: The absolute magnetic field at $z = 500$ mm and $\phi = \pi/2$ in r direction and at $r = 102$ mm in ϕ direction. The green bar indicates the wall of the inner cylinder and the orange bar represents the wall of the outer cylinder.

cylinder. The magnetic field exhibits sharp peaks around $z = 0$ and $z = 1000$ that are due to the edges in the geometry. Between the peaks, the magnetic field distribution resembles the top-bottom temperature difference for all 5 studies. It can be concluded that the bottom-top gradient determines the degree of asymmetry in the system and hence the magnetic field in the interior. From the orientation of the magnetic field that is shown in form of arrows in Table 4.1 it follows that the magnetic field is oriented orthogonal to the top-bottom gradient of the temperature in the cylindrical system.

The simulations illustrate that a non-symmetric temperature distribution leads to a nonzero magnetic field on the RF surface. The highest fields are obtained where the temperature difference between top and bottom part are largest. In Study 5, this effect leads to a more or less constant magnetic flux along the cylinder while in Study 3, where the temperature gradient from bottom to top is less distinct, the magnetic field increases towards the center of the cylinders ($z = 500$ mm). In the experiment, the highest degree of broken symmetry is obtained when the first superconducting path through the cavity establishes below 9.25 K. This corresponds to an extreme example of Study 5 where the DC resistance of the bottom part of the inner cylinder drops to zero while the rest of the cavity is still normal conducting and hence the thermocurrent is forced into the superconducting region.

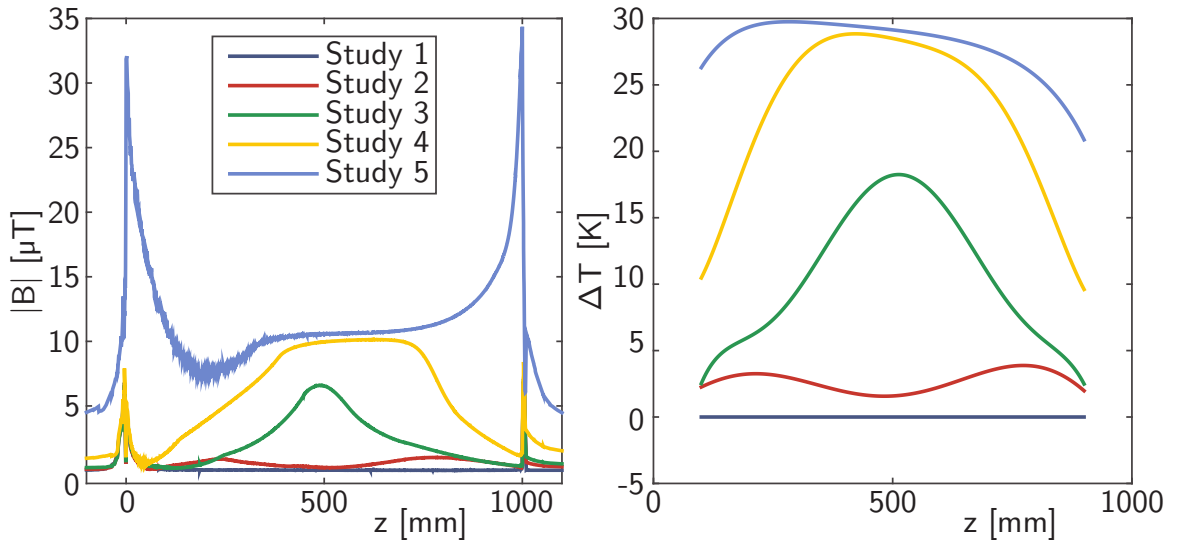


Figure 4.12: The absolute magnetic field at $r = 102\text{ mm}$ and $\phi = \pi/2$ in z direction and the top-bottom temperature difference in the inner cylinder wall along z .

4.3.2 Thermocurrent: Simulation of the Cavity Geometry

Following the two cylinder simulations that provided a general insight in the thermocurrents in a coaxial system, the simulation was expanded to the TESLA nine-cell cavity geometry. In addition to the correct cell shape, the magnetic shielding around the tank was implemented. Couplers, tuner and small features like brackets etc. were however left out because they increase the number of mesh cells and the computation time without influencing thermoelectric results. The bellow that compensates length differences between tank and cavity was omitted as well. But it had to be accounted for in a different manner because it was fabricated from a thin titanium sheet and its electrical resistance equaled the resistance of the tank. Hence it increased the resistance of the overall system considerably and limited the thermocurrent as was discussed by Crawford [63]. In addition, the helium vessel heads were fabricated from NbTi, not Ti as was assumed in the two cylinder simulations. The material properties of NbTi differ from Ti and are sensitive to the Nb/Ti stoichiometry. Literature data on the NbTi used in SRF cavities is rare and therefore it was refrained from implementing the material in the simulations. Nevertheless, both, the bellow and the vessel heads, increase the DC resistance of the system and thus decrease the thermocurrent. However, their resistivity could not be measured directly and experimental data was employed to account for that in the Comsol model.

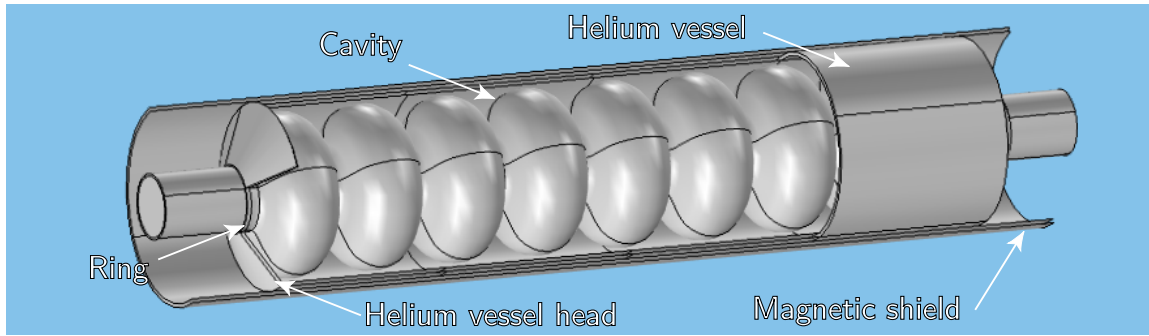


Figure 4.13: Comsol model of the cavity in the tank with adjusted resistance and magnetic shielding.

Adjustment of Electrical Resistivity

Section 3.4 presented data on a cavity that was equipped with magnetic field diagnostics between the tank and the cavity. An equal cavity with similar diagnostics was tested in a vertical test stand at Fermilab [64]. A cooldown in a vertical test achieved an almost perfect symmetric temperature distribution with only a temperature gradient along the cavity and no gradient across. Accordingly, the magnetic field had only an azimuthal component. In contrast to cases with broken symmetry, the symmetric situation is easy to reproduce in the simulations. The temperatures of the helium vessel heads, as well as the magnetic field in the azimuthal direction at the top of one cell are known from the experiment. This information can be used to estimate the resistance for the model until the magnetic field in the simulation equals the value from the experiment. A small ring was inserted at the junction of cavity and tank. The electrical resistivity of titanium was assigned to it and scaled to adjust the overall resistance of the system. The temperature dependence was preserved. All other material parameters were set as titanium values. The complete geometry of the simulations is shown in Figure 4.13.

In the first simulation of the cavity, the resistivity of the ring was set to the value of titanium and temperatures of the joints to 10 K and 100 K according to the experimental data from the vertical test [64]. At cell 5, the corresponding magnetic field value of $20.0 \mu\text{T}$ was measured. The simulated value at the same position was $35.6 \mu\text{T}$. In the subsequent simulations the resistivity of the ring was increased until the simulated value matched the measurement. Thereby, the resistance contribution of the bellow and the NbTi vessel heads were accounted.

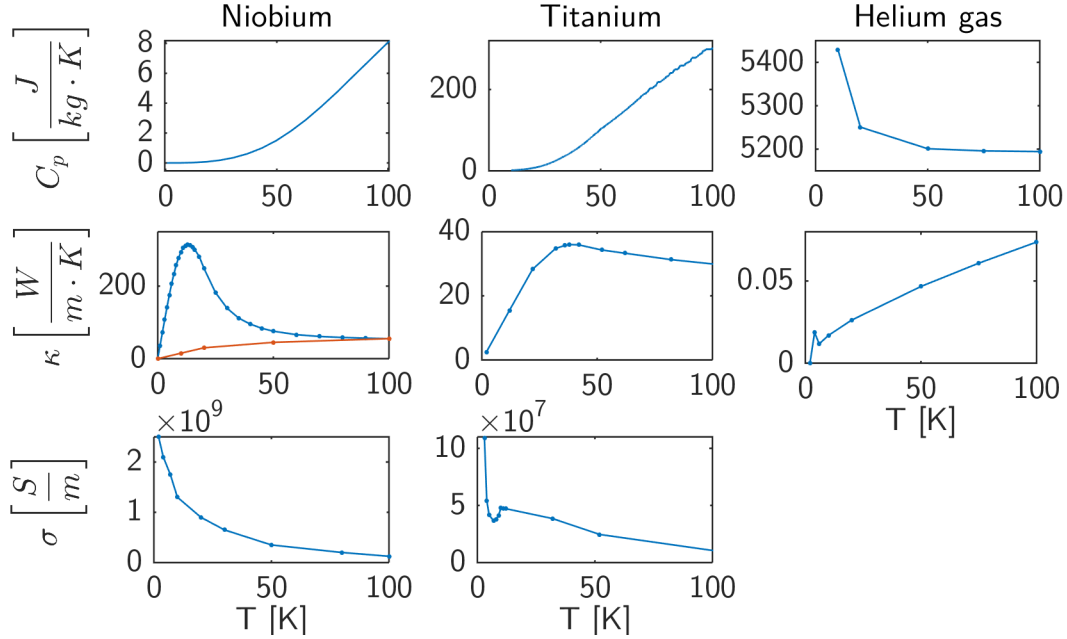


Figure 4.14: Heat capacity C_p , thermal conductivity κ and electrical conductivity σ data with interpolations for $RRR = 300$ niobium, grade 2 titanium and gaseous helium at normal pressure used for the Comsol simulations. The red curve in the thermal conductivity of niobium indicates the $RRR = 50$.

Material Properties

The material properties of titanium, niobium and helium were taken from the References [3, 60, 61, 62]. Figure 4.14 provides an overview over the used material properties. The thermal conductivity was also set temperature dependent. High purity niobium exhibits a maximum below 50 K, which caused problems with the convergence of the simulations. Hence the curve of $RRR = 50$ was chosen for the thermal conductivity. This might locally alter the resulting temperature distribution. However, all important conclusions are later drawn from the direct comparison of temperature distribution to magnetic field distribution where the thermal conductivity plays no role anymore.

Asymmetric Temperature Distributions

After the electrical resistance was adjusted, studies similar to the two cylinder studies were performed. The areas of the tank were defined and boundary conditions were applied in the same way as shown in Figure 4.9. Figure 4.15 shows the result obtained for Study 5 temperature boundaries with maximum asymmetry. The distributions of temperature and magnetic field are comparable to the results of the two cylinder

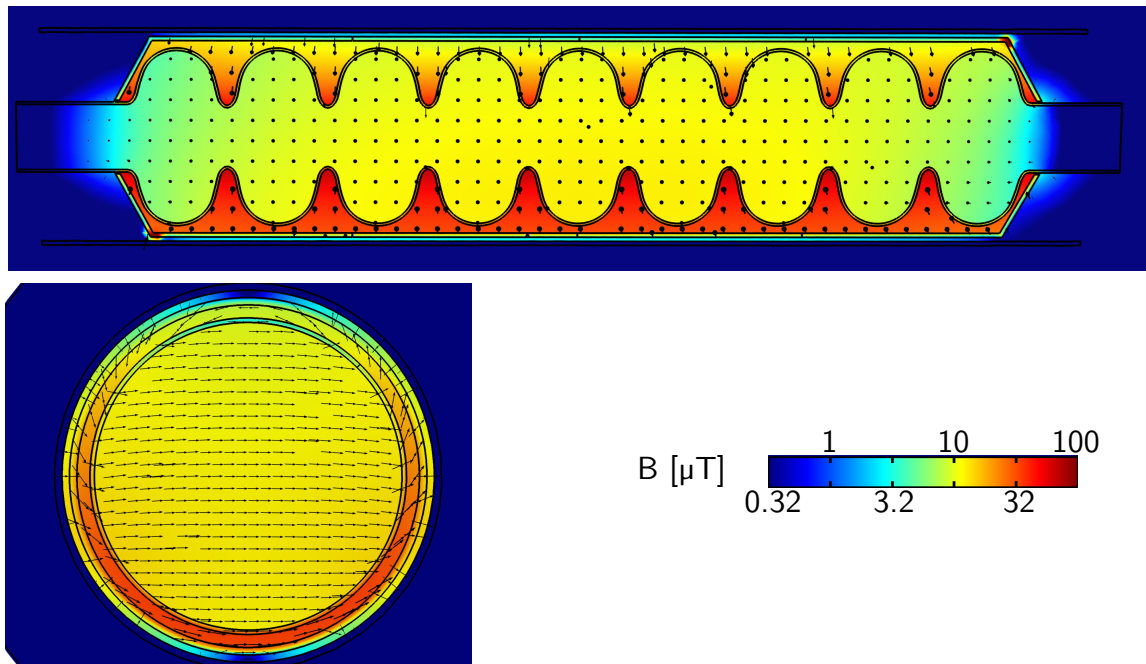


Figure 4.15: Magnetic field inside cavity and tank in a logarithmic scale for Study 5 temperature boundaries. The black arrows indicate the magnetic field vectors that point into and out of the paper in the top figure and from left to right in the bottom figure.

simulations but now, the amount of magnetic field can be analyzed. Furthermore, the magnetic field is more homogeneous due to the magnetic shielding. Since the vessel heads are set to a constant temperature, the asymmetry and hence magnetic field in cells 1 and 9 are reduced. In the cells 2 to 8, the magnetic field inside the cavity ranges from $8\ \mu\text{T}$ to $14\ \mu\text{T}$. The maximum in each cell is at the bottom and the field decreases towards the top. This result has the correct magnitude to explain the increased residual resistance in the RF tests. The magnetic field inside the cavity is orientated orthogonal to the bottom to top gradient. Figure 4.16 shows the radially exported field values cut across cells 1, 3 and 5. While the field inside the cavity shows comparatively little variation in the different graphs, the field between cavity and tank reaches significantly higher values closer to the iris than closer to the equator. Furthermore, the field in the bottom of the tank is increased compared to the field in its top.

To this point, the simulations yielded promising results. Thus, they can be used to investigate the system even further. The highest degree of asymmetry occurs during phase transition when a superconducting spot establishes and subsequently grows.

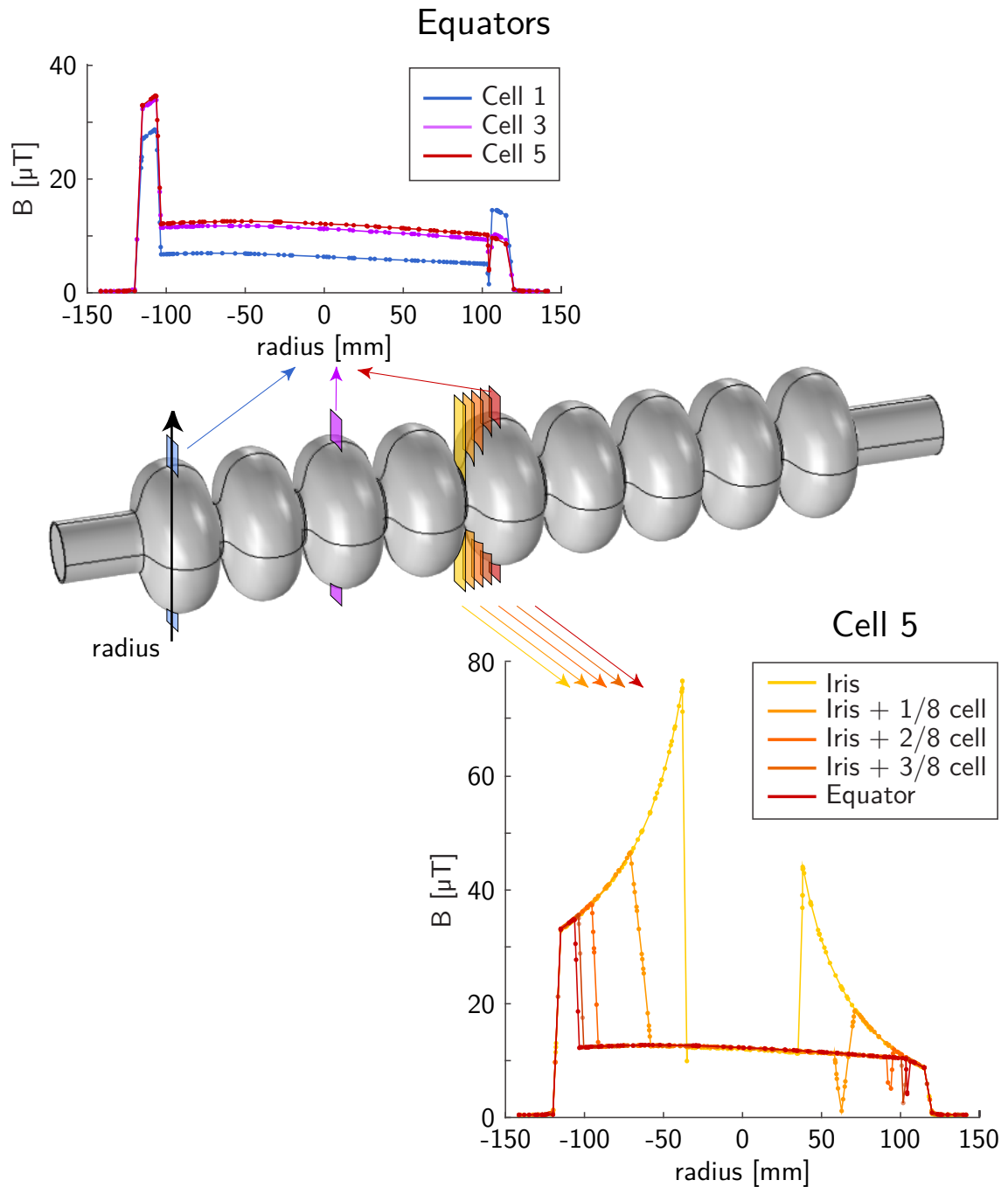


Figure 4.16: Simulated magnetic field across the cavity (bottom to top) for temperature distribution 5 at different positions in cells 1, 3 and 5. The drops in magnetic field in the bottom right plot around $r = 60$ mm and $r = 100$ mm are artifacts from the export caused by the shape of the cavity wall which is almost parallel to the export axis at this locations.

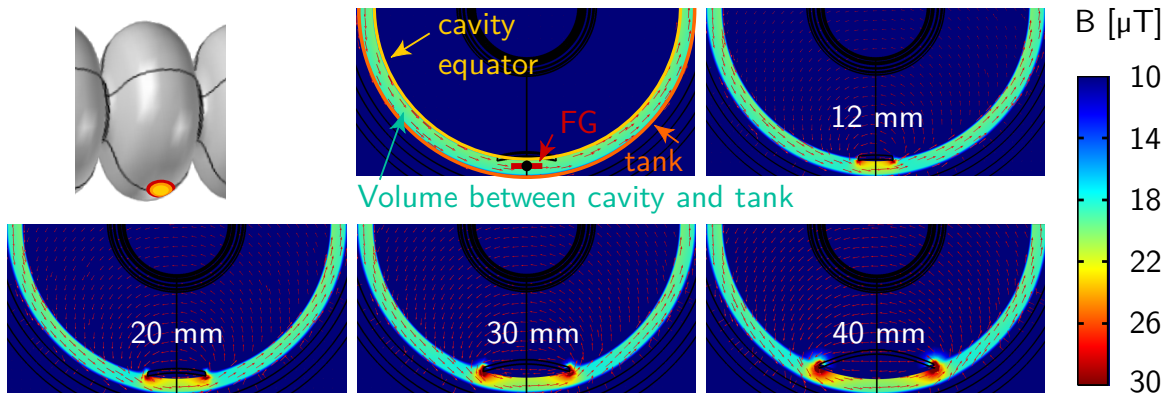


Figure 4.17: Magnetic field distribution around a growing superconducting spot at an equator. The yellow circle indicates the cavity equator, the orange circle the tank, the red rectangle a fluxgate that measures the thermocurrent and the black dot on top of the FG the “FG position” used for evaluation of the simulations and comparison with measurements.

Simulation of a Growing Superconducting Area

The superconducting phase transition is the pivotal moment during the cooldown of an SRF cavity. At this instance, it is decided how much flux gets trapped inside the material. In Section 3.4, direct measurements of the magnetic field between cavity and tank during phase transition were presented. It was shown that a peak occurred in the magnetic field during the phase transition and that the height of this peak was correlated with the RF dissipation. In the now following sections, simulations will be presented that give more insight in the processes during transition and hence allow for a more profound interpretation of the experiment data.

In the simulations, the superconducting material was implemented in form of niobium with modified properties. The electrical conductivity was increased by a factor of 10^3 and μ_r was set to 10^{-6} to simulate (almost) vanishing DC resistance and perfect diamagnetism. The thermal properties were not changed. The goal of the simulations was to investigate the influence of the localized appearance of superconductivity independently of other sources of asymmetry. Hence, a setup was created to separate the effect based on the temperature distribution of Study 1, which provided the same driving force for the thermoelectric current as in all other simulations but without embedded asymmetry. A defined round area at the bottom of the equator of cell 5 was set to the modified niobium properties to simulate the superconducting spot without manipulating the temperature distribution. Thereby, the superconducting area was not below the transition temperature, which did not matter because the conductivity was increased by definition. This setup allowed

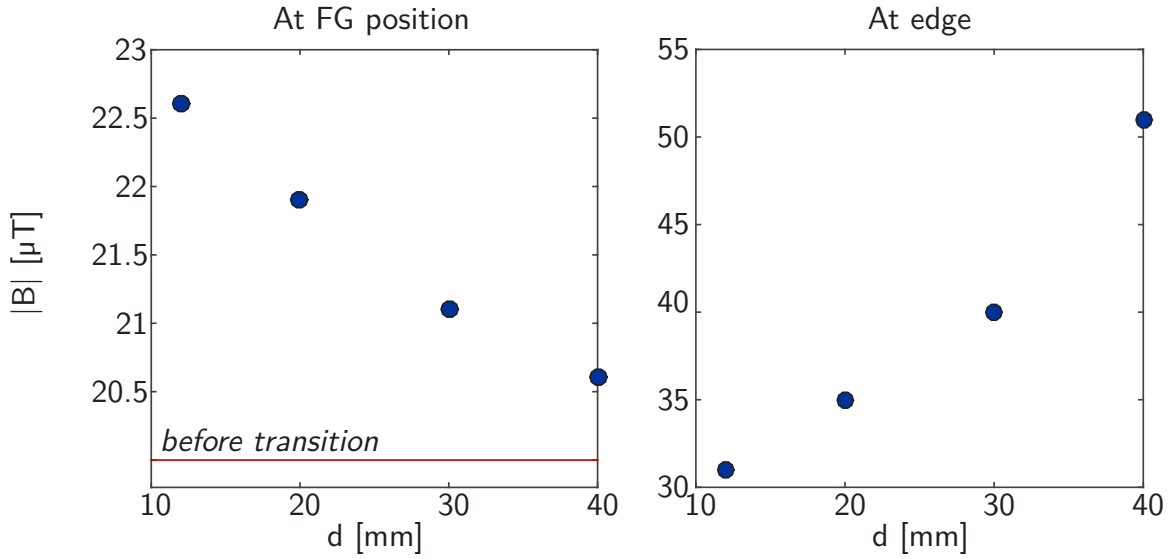


Figure 4.18: Magnetic field of a growing superconducting spot at the position of the black dot in Figure 4.17 (FG) and the maximum field at the edge of the spot.

an estimate of the field distribution after the onset of phase transition without the necessity of implementing a complicated temperature distribution.

Figure 4.17 shows the results of the simulations. The numbers give the diameter of the spot and the black dot in the first plot gives the “FG position” at which the magnetic field values were compared. In the symmetric case, the field value was $20 \mu\text{T}$. For the smallest spot (12 mm), the field increased to $22.6 \mu\text{T}$. At the edge of the superconducting area, the field even reached a value of $31 \mu\text{T}$. With increasing spot size, the magnetic field at the FG position decreased towards the value of the symmetric case. The field at the edge increased due to the Meissner effect. The data is displayed in Figure 4.18. The left plot in the figure can be compared to the magnetic field data of the experiments in Section 3.4. Figure 3.13 showed the signal of the magnetic field probe inside the tank below a cavity equator during thermal cycle 12. The maximum temperature difference between the Nb-Ti joints established after the cooldown had started. An almost constant magnetic field value of $15.2 \mu\text{T}$ was reached in the tank. When the cavity was further cooled, the temperature difference slowly decreased but the magnetic field exhibited a peak before it also decreased. The peak is shown in Figure 4.19 together with the peaks that occurred during two similar cycles. The feature was generic and very reproducible for any thermal cycle with a significant ΔT along the cavity-tank system. Furthermore, its amplitude was directly linked to the RF dissipation as was shown in Figure 3.14, which indicated that the peak was a measure of the amount of thermocurrent in the system.

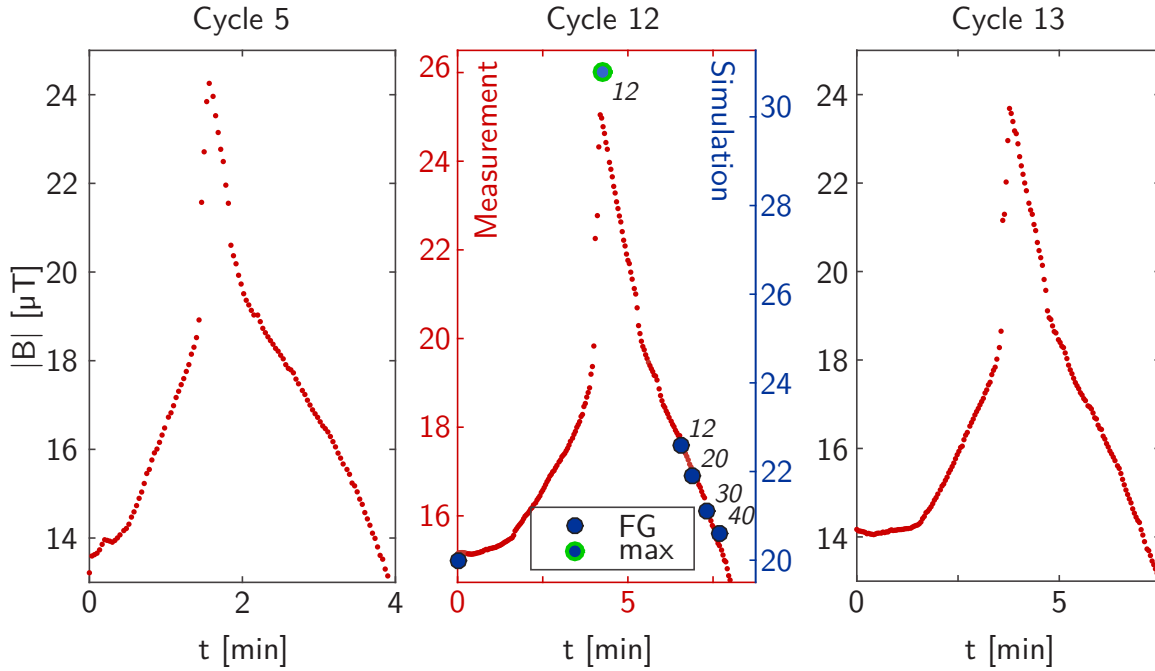


Figure 4.19: Generic magnetic field peak in the measurements together with simulated magnetic field values. The blue circles indicate the field at the FG position for the different diameters of the growing superconducting area. The diameters are given in millimeters as italic black numbers. In addition, the maximum field calculated at the edge of a 12 mm superconducting area is plotted in green.

Based on the presented simulations, the experimental findings can now be explained. The middle panel in Figure 4.19 shows the FG data of Cycle 12 together with magnetic field values that were extracted from the simulations of the growing superconducting area. The spreads of both ordinates were set equivalent but the limits were shifted in a way that the measured value before the peak coincided with the simulated value of the symmetric simulation.

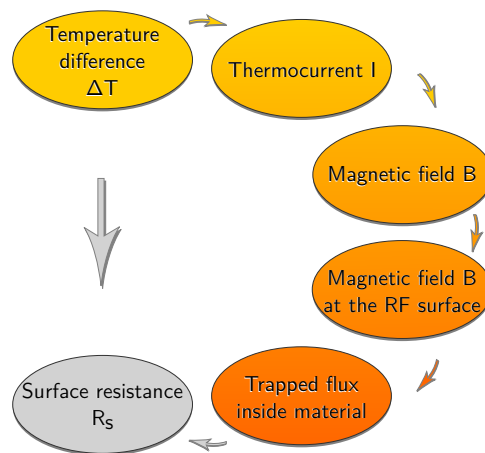
Figure 4.17 showed how the magnetic field present in the symmetric case gets enhanced once a superconducting area establishes. It is maximal at the edge of the area where the phase front is located. The maximum value, computed for the smallest area size of $d = 12$ mm, was added to Figure 4.19 as an estimation of the peak height. This simulated point corresponded to the experimental situation when the phase front was closest to the FG and accordingly the measured field peaked. Furthermore, the simulated values of $d = 20, 30, 40$ mm were plotted equidistantly into the figure to describe the reduction in measured field when the phase front was advancing and hence its distance to the FG was increasing. The simulations and the data agreed qualitatively very well, though it must be remarked that the simulated points have no

direct relation to the x axis. In addition, the measured field in the experiments was not dropping back to the value obtained before transition but decreases further. This decay may be caused by the reduction of the joint temperatures during the proceeding cooldown, which lead to a decrease in the overall amount of thermocurrent and will be discussed at a later point.

Based on the results of the simulations, the correlation of RF dissipation with peak magnetic field in the experiment (Figure 3.14) can be understood. The change in peak height between different cycles, if measured at the same position and for similar temperature distributions, corresponds to the change in overall amount of thermocurrent in the system. The more current is flowing, the higher is the resulting peak in magnetic field during transition and vice versa.

Further simulations of the thermocurrents in the cavity-tank system that are in agreement with the here presented results were performed at Cornell university and can be found in Reference [59].

4.4 Direct Measurement of the Magnetic Field at the RF Surface



The simulations in the previous sections provided insights in the overall thermoelectric effect in the cavity-tank system and some results were compared to the fluxgate data obtained in a cavity test. However, the magnitude and orientation of the magnetic field *inside* the cavity, which are also known from the simulations, could not be compared to experimental data so far. The final step in the thermocurrent analysis is therefore an experiment that attempts a direct measurement of the magnetic field during cooldown as well as of the trapped flux inside a TESLA nine-cell cavity at the

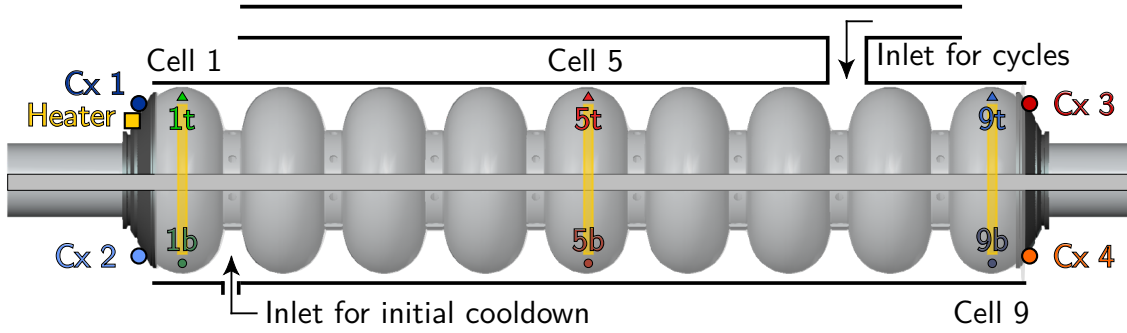


Figure 4.20: Positions of the six fluxgates for the direct measurement of the magnetic field inside the cavity. The triangles indicate the FGs in the top of the cells and the bullets indicate the FGs in the bottom.

RF surface. The cavity for the test was provided by DESY. Obviously, no RF test could be performed while probes were inside the cavity.

Setup

Four temperature sensors were mounted on the helium vessel heads at the same positions as in the previous experiment on the nitrogen annealed cavity (Figure 3.11). In addition, six fluxgate magnetometers were positioned inside cells 1, 5 and 9 at the equators in perpendicular orientation with respect to the cavity axis. The positions of the sensors are shown in Figure 4.20. For better orientation in the data, the sensors were color and marker coded: triangles for FGs in the top, circles for FGs in the bottom; green for FGs in cell 1, red for cell 5 and blue for cell 9. The cooldown and thermal cycles were performed similar to the previous cavity tests to reproduce the cooling conditions.

4.4.1 Change in Magnetic Field During a Cycle

The setup can be used track the change in magnetic field during warm up and cool down. The six FGs were read out by four read out units hence only four probes could be read simultaneously. Figure 4.21 displays the temperatures on the tank and the magnetic field values inside the cavity for FG 1 to 4 during thermal Cycle 4. In addition, Figure 4.22 shows the magnetic field data during the cool down period of Cycles 5 and 8. The temperature differences at the onset of superconducting phase transition during the three cooldowns were comparable with $\Delta T_{av} = 55$ K for Cycle 4, $\Delta T_{av} = 67$ K for Cycle 5 and $\Delta T_{av} = 65$ K for Cycle 8.

In the beginning of each cycle, the LHe was evaporated. The temperatures increased slightly but no change in magnetic field occurred. Once the tank was empty,

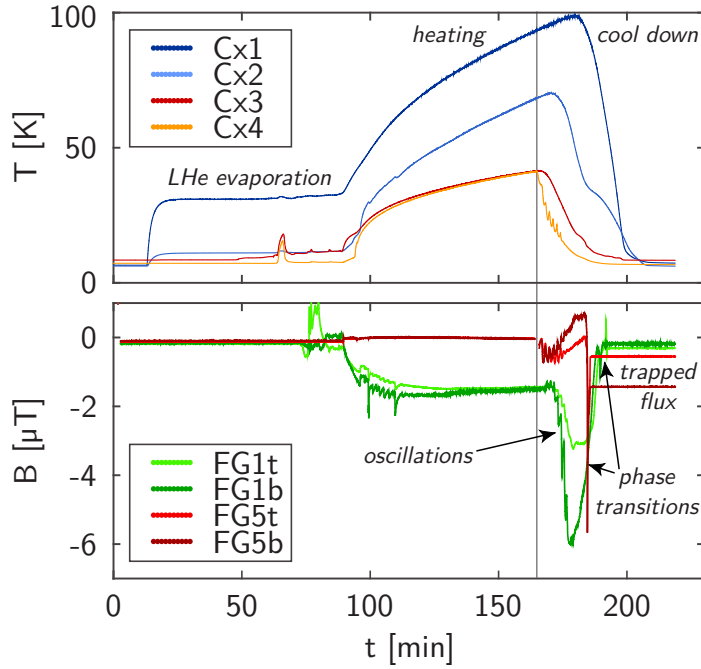


Figure 4.21: Temperatures on the tank and magnetic field values inside the cavity during Cycle 4 (with $\Delta T_{\text{av}} = 55$ K). The vertical black line indicates the moment when the cooldown started.

all plots show a small increase in magnetic field due to thermoelectric current during the heating period. The signal was most distinct in cell 1 where the FGs reached about $2 \mu\text{T}$. The field values were, however, low compared to the values, which were measured in the space between cavity and tank in the previous test. In Section 3.4, it was shown that the magnetic field in the tank reached about $15 \mu\text{T}$ for similar conditions. These numbers indicate that the heating created an almost symmetric temperature distribution, which resulted in a high thermoelectrically generated magnetic field in the tank but almost no field inside the cavity. The situation changed drastically once the cooldown started. Now, a strong asymmetry was introduced and the magnetic field inside the cavity rapidly increased. FG1b in cell 1 reached a maximum in absolute field of $6 \mu\text{T}$. The thermoelectric field was less pronounced in the other cells though it amounted to 1 to $2 \mu\text{T}$ there as well. The reason for that is the heater that upheld the temperature difference and was positioned off center hence an additional asymmetry was created that was largest close to the heater, which was in cell 1. Since the FGs inside the cavity registered only asymmetric induced magnetic field, the measured field before the phase transition was maximum in cell 1 and smaller in cells 5 and 9. This, however, changed during phase transition. Cell 9 transitions first and exhibits the highest amount of flux trapped after the transitions.

Before the different levels of trapped flux will be discussed further, one detail of the presented B vs. t curves shall be discussed. The plots show oscillations that occurred in the beginning of the cool down period in each graph. The features were

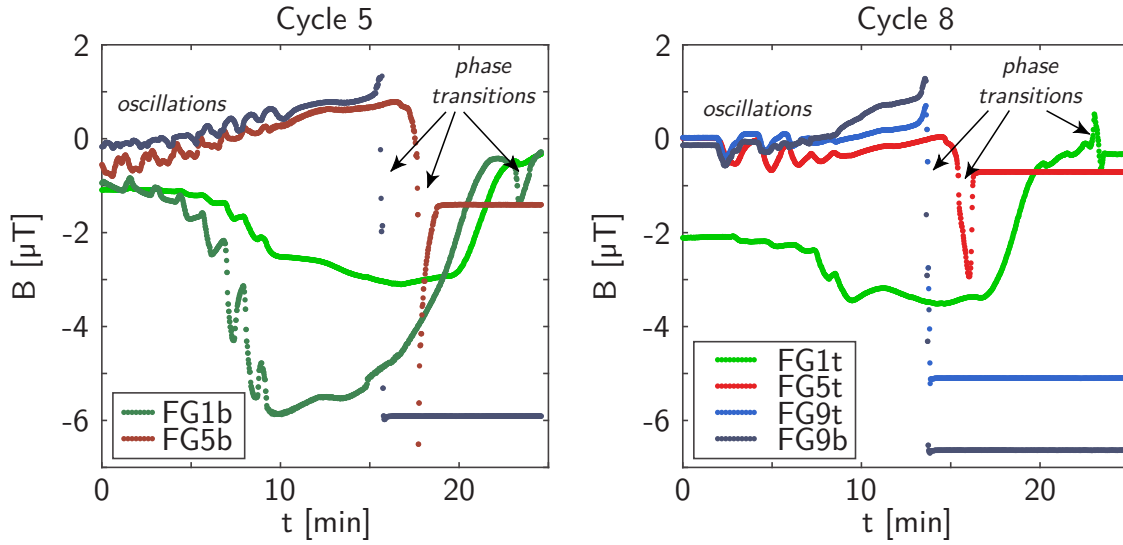


Figure 4.22: Change in magnetic field during Cycles 5 (with $\Delta T_{av} = 67$ K) and 8 (with $\Delta T_{av} = 65$ K). The blue FGs are in cell 9, the red in cell 5, the green in cell 1. A light color indicates probes in the top of the cell and a dark shade in the bottom.

caused by instabilities in the cryoplant during the start of the cooldown. At the time, the cavity was still warming up but the tank and LHe lines were already cooling down. Once they were cooled down enough, LHe reached the still warm tank. It quickly evaporated there creating a drop in temperature at the bottom and cold gas that spread to the cavity and caused an asymmetry in the thermocurrent. In addition, the pressure in the system increased. The regulation of the pumps counteracted and the helium flow was reduced. The process repeated until the temperature at the bottom of the tank was close enough to 4.2 K and the system stabilized. The oscillations were also observed in the gas temperatures in the cryosystem and in the measured magnetic field.

The described oscillations did not influence the level of trapped flux but they were used to correlate the data of different sensors. Appendix E shows a comparison of the magnetic field measured with fluxgates and with AMR sensors, which were also positions inside the cavity.

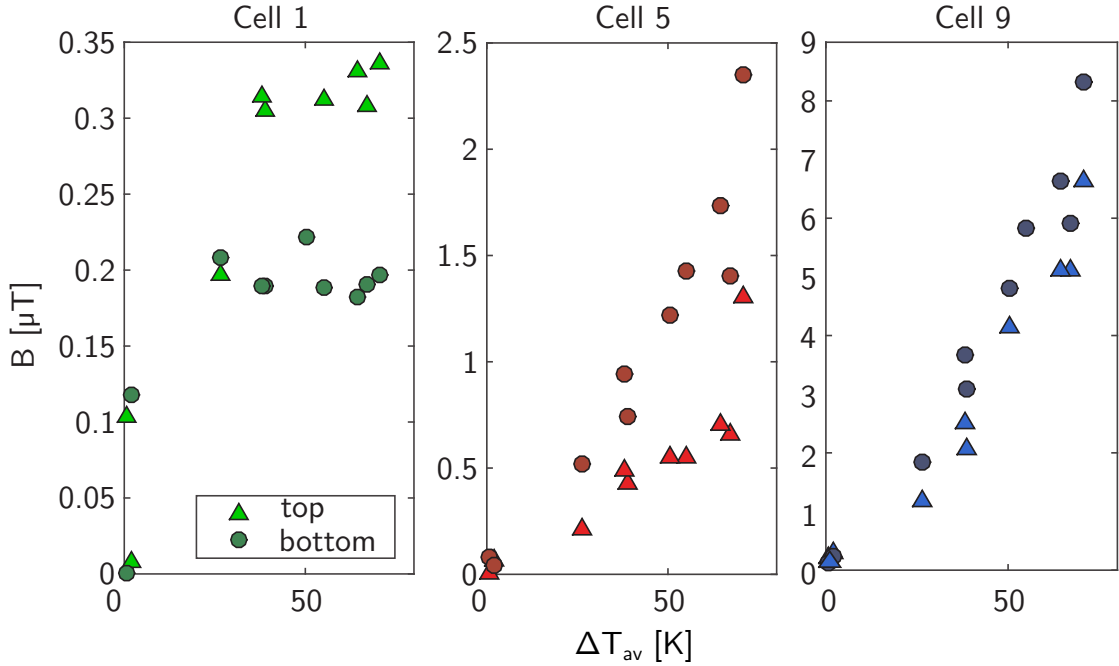


Figure 4.23: Direct measurement of the trapped magnetic flux inside the cavity by six fluxgates. The triangles correspond to the FGs in the top of each cell and the bullets to the FGs in the bottom (see Figure 4.20).

4.4.2 Phase Transition and Trapped Flux

In addition to the oscillations, the Figures 4.21 and 4.22 show peaks and step-like changes once the niobium close to each FG transitioned into the sc state. Thereafter, the magnetic field measured by each FG was stable. After each cycle ended, this level of trapped flux was evaluated. Figure 4.23 shows the result as a function of the average temperature difference at the onset of phase transition ΔT_{av} (as described in Section 3.3.2) for the thermal cycles. The data of the initial cooldown is not displayed and will be discussed later.

Four conclusions can be drawn from the data. First, the most flux in the spatial direction of the FGs was trapped in the cell that transitions first. During all cycles with a ΔT_{av} larger than 20 K, FG9b showed the transition first, only 2 to 3 seconds later followed by FG9t, which was closest to the chimney. The maximum values of trapped flux were $8.3 \mu\text{T}$ at the bottom of cell 9 and $6.6 \mu\text{T}$ at the top. In Cycle 4, as one example, we see that cell 5 transitioned roughly 2 min later. Here, the bottom transitioned half a minute earlier than the top and the probes exhibited lower values of trapped flux with a maximum of $2.4 \mu\text{T}$ at the bottom and $1.3 \mu\text{T}$ at the top. Finally, cell 1 transitioned about 8 min after cell 9, again bottom first. The trapped flux was below $0.35 \mu\text{T}$ after all cycles. While the transition expanded from cell 9 to cell 1,

the temperature difference between the niobium-titanium joints decreased. Hence, the thermocurrent in the system decreased also, which explains the lower levels of trapped flux in cells 5 and 1.

Second, the amount of trapped flux increased with ΔT_{av} , which was as expected. A higher temperature difference generates a higher thermocurrent and hence a higher magnetic field. The data shows that the trapped flux increased accordingly.

Third, the probes registered more trapped flux in the bottom of the cells than in the top. The increase with ΔT_{av} was thus less steep in the top. The simulations (Figure 4.16) had already shown that the field at the bottom is expected to be larger than at the top of each cell, which originated from the lower temperature and hence lower DC resistance at the bottom of the cavity prior to the phase transition. However, the transition itself and the delay between the transitions of bottom and top in cells 1 and 5 can also influence the level of trapped flux.

Fourth, the magnitude of trapped flux is sufficient to explain the increased residual losses in the RF test. In order to compare the direct measurement of the trapped flux to the RF results, the distribution of trapped flux over the whole cavity must be estimated based in the data from cells 1, 5 and 9. The RF test in Sections 3.3 and 3.4 (Figure 3.10 and Figure 3.12) indicated that the residual resistance increased by the same amount in all three tested passband modes. Each mode had a specific RF field distribution and hence yielded an average surface resistance were the cells were weighted accordingly. The modes are (almost) symmetric hence the RF test results can be explained by several magnetic field distributions. The easiest one assumes that the trapped flux is constant over all cells or over half the cavity. However, this assumption does not fit with the results of the direct measurement, which favors a non-constant distribution of trapped flux. Two distributions, which would fit with the direct measurement are a linear or a quadratic increase over the length of the cavity. Figure 4.24 shows conceivable distributions of trapped magnetic flux in all nine cells, which were calculated based on the data for cells 1, 5 and 9. Only the data for Cycle 2, the cycle with the highest level of trapped flux, is shown as an example. For comparison, another two distributions are displayed were the trapped flux is focused only in the middle of the cavity or only at its end.

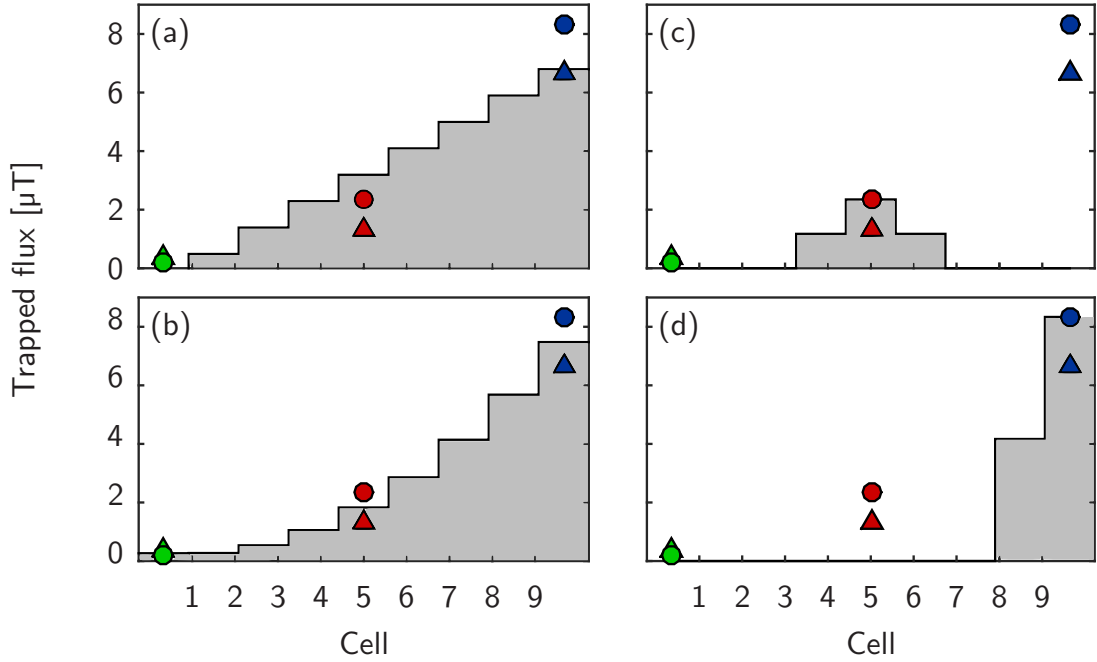


Figure 4.24: Directly measured trapped flux in cells 1, 5 and 9 together with conceivable distributions of trapped magnetic flux in all nine cells for Cycle 2. (a) linear and (b) quadratic increase from fit of the data. For comparison, (c) and (d) assume that the trapped flux is focused in the middle or at one end of the cavity.

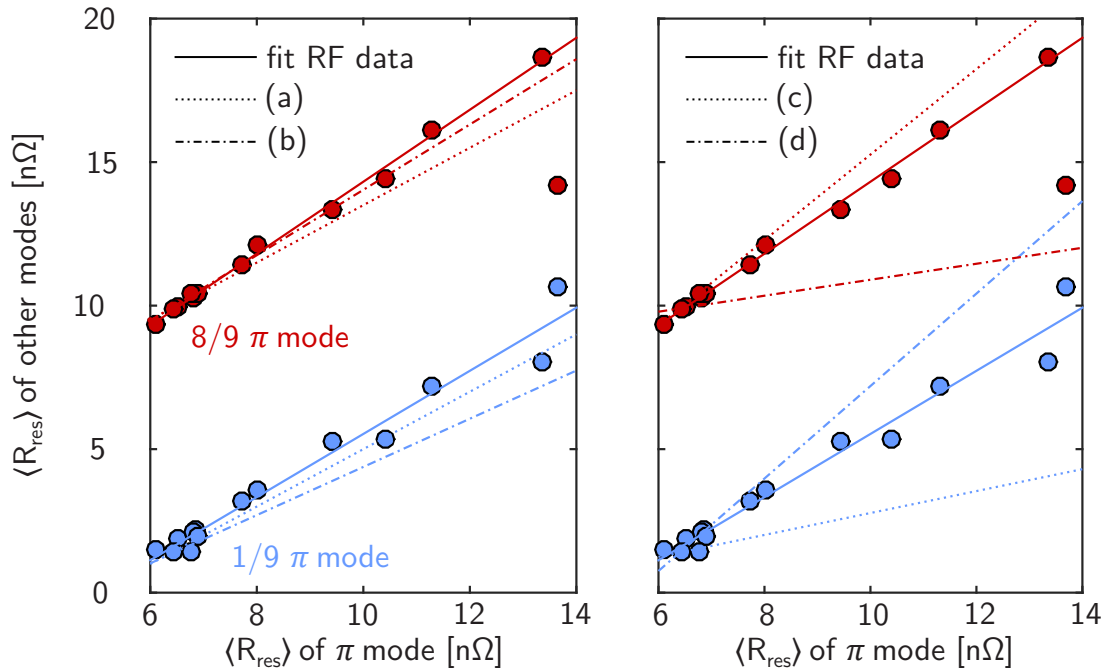


Figure 4.25: RF data from Figure 3.10 compared to conceivable distributions of trapped flux (a) linear, (b) quadratic, (c) focused in the middle, (d) focused in one end.

4.4.3 Comparison to RF Data

The obtained distributions can now be compared to the RF data. Figure 4.25 reproduces the RF data from previous tests where the residual resistances of the $1/9\pi$ and $8/9\pi$ mode were compared to the one of the π mode. In addition, the linear fits of the two curves are displayed. For the $8/9\pi$ mode, the initial cooldown did not fit with the thermal cycles and was hence excluded from the fit. The right plot in Figure 4.25 shows clearly that trapped flux, which is localized in just a small part of the cavity would not explain the RF data. The left plot shows that the curve for the $1/9\pi$ mode is reproduced best if a linear profile of trapped flux is assumed. For the $8/9\pi$ mode, the quadratic profile fits best. As a result we can conclude that neither distribution can reproduce the RF data. However, a linear or quadratic increase give reasonable approximations and most likely the actual profile is somewhere in between the two.

The maximum trapped flux was obtained after Cycle 2. Averaged over the whole cavity, the trapped flux here amounts to $3.2\mu\text{T}$ in all three modes for a linear profile, which corresponds to $11.2\text{n}\Omega$ additional surface resistance. For the quadratic profile, the values are $2.3\mu\text{T} \hat{=} 8.1\text{n}\Omega$ ($1/9\pi$ mode), $2.7\mu\text{T} \hat{=} 9.5\text{n}\Omega$ (π mode) and $3.0\mu\text{T} \hat{=} 10.5\text{n}\Omega$ ($8/9\pi$ mode). The RF tests resulted in additional surface resistance of $9.2\text{n}\Omega$ ($1/9\pi$ mode), $7.2\text{n}\Omega$ (π mode) and $8.7\text{n}\Omega$ ($8/9\pi$ mode) for the highest R_{res} compared to the lowest one. This is a remarkable accordance given the 10% errorbar on the RF data and the limitations of the direct measurement, which will be discussed in the next paragraph.

The FGs measured only one spatial direction at only six locations. The simulations showed that the trapped flux is likely to point in a direction that is orthogonal to the temperature gradient that causes the asymmetry in the system. The cooldown of the cavity with helium gas and liquid proceeds chaotically to some degree. Hence the orientation of the asymmetry can change and with it the orientation of the magnetic field and the resulting trapped flux. Furthermore, the interpolation of the trapped flux in all cells based on the data of six probes contains some error. In particular, it is unknown how the trapped flux is distributed in just one cell between the bottom and the top.

Finally, the initial cooldown results were not discussed so far. Here, the largest value was measured in cell 5 with $3.8\mu\text{T}$, followed by cell 1 with $0.3\mu\text{T}$ and cell 9 with $0.1\mu\text{T}$ - a very different distribution of trapped flux compared to the thermal cycles. This is another indication that the cooling dynamics during the initial cooldown differ significantly from the cycles, which was already observed in the RF tests.

4.4.4 Comparison to Simulations

The measured distribution of trapped flux can not only be compared to the RF data but also to the simulations in Section 4.3.2. So far, only the resulting magnetic field for a temperature difference of 90 K was presented (Figures 4.15 and 4.16). Now, the simulations were repeated for a different temperature difference.

The maximum trapped flux was measured for $\Delta T = 70.7$ K with $8.3 \mu\text{T}$ at the bottom and $6.6 \mu\text{T}$ at the top of cell 9. A simulation of similar conditions resulted in magnetic field values of $7.9 \mu\text{T}$ (bottom) and $6.7 \mu\text{T}$ (top), which is a reasonable agreement.

4.5 Discussion: Thermocurrents in SRF Cavities

We showed that the trapped magnetic flux due to thermocurrents is distributed over the whole length of the cavity and that it is increasing from almost no trapped flux in cell 1 to the maximum in cell 9, when cell 9 transitions first into sc state. The duration of the phase transition was determined to be about 5 min. Figures 3.5 and 3.13 showed that the joint temperatures during the thermal cycles were significantly changing during that period. It is reasonable to conclude that ΔT along the cavity, as well as $S(T)$ of the two materials, decreased during the phase transition leading also to a decrease in thermoelectric field. Cell 9 therefore experienced a higher ambient field during transition than cells 5 and later cell 1. By that conclusion, the directly measured distribution of trapped flux can be explained. In addition, the assumption was confirmed by numerical simulations of the system.

Furthermore, it was demonstrated in Figure 4.7 that the curve of the residual resistance as a function of temperature difference can be fitted based on the temperature-dependent thermopower. However, it was shown that the abscissas had to be chosen differently. The decrease of ΔT during phase transition now explains this discrepancy. The abscissa of the RF data displayed the ΔT at the onset of the sc phase transition, which is the ΔT that caused the maximum trapped flux in cell 9. The RF data, however, was measured as average over the whole cavity, where the trapped flux was decreasing towards cell 1. Hence the integrated thermovoltage corresponded not to the ΔT at the onset of the sc phase transition but more an average value of the ΔT values at transition of all nine cells, which was noticeably smaller.

The duration of the sc phase transition and the temperature distribution during it is specific for our cryostat because it is, among others, limited by maximum helium flow. Hence the resulting distribution of trapped flux is also specific for HoBiCaT

and can be different for other cryostats or even for a different cooldown scheme, as was demonstrated during the initial cooldowns.

In the experiments, data from the initial cooldown did repeatedly not line up with the data obtained after the thermal cycles. A divergent result was shown in both the RF tests with the BCP cavity and in the direct trapped flux measurement with the cavity provided by DESY. Based on the data, it can be concluded that the origin for the difference lies in the temperature distribution during the phase transition. All cycles exhibited comparable distributions with only a different ΔT magnitude. Due to the design of the helium tank, the initial cooldown however yielded a very different temperature distribution since the LHe inlet was on the opposite side of the chimney leading to the two phase pipe and the trapped flux after the initial cooldown accumulated in the center cells.

In the test with the N-doped cavity, the initial cooldown exhibited a smaller ΔT during phase transition and the RF dissipation was reduced accordingly. The reason may lie in the different tank setup (Figure 3.11) where inlet and chimney are on the same side of the tank.

In conclusion, the experimental data of the RF tests and the magnetic field measurements, as well as the simulations fit very well with the proposed thermocurrent model. The hypothesis was thereby proven and every step in the line of argument was traced. Further studies that support the drawn conclusions are given in References [59, 65].

In addition, the presented results explain why the effect was not noticed before in vertical tests. Though the thermocurrents may exist there as well, they are symmetric and hence cause no degradation to the RF surface. The thermocurrents can only become significant in an asymmetric situation as the horizontal test.

One topic that was not included in the discussion so far is the question of flux expulsion. Since the simulated magnetic field values were similar to the trapped magnetic flux, it can be concluded that almost all magnetic field was trapped during the sc phase transition. However, studies that will be discussed in Chapter 5 demonstrated that not all magnetic field that is present during phase transition must get trapped in the material. The percentage can vary from almost no to almost all magnetic flux getting trapped and that probably applies to thermoelectric generated field just the same. Hence, a high level of thermocurrent does not necessarily result in high RF losses. Some aspects of that final topic will be investigated in Chapter 5.

Chapter 5

Flux Trapping and Flux Expulsion

The previous chapters focused on the sources of magnetic field in an SRF environment because the field may get trapped in the superconductor during the phase transition and thereby increase RF dissipation. Hence, the elimination of all sources is a sound approach to achieve high quality factors in SRF cavities. However, as we have seen, magnetic flux can not always be avoided.

There is an ongoing discussion on the proportion of ambient magnetic field that actually gets trapped during the sc phase transition. According to the Meissner effect below H_{c1} , the minimum in energy is reached when all magnetic field is expelled. On the other hand, experimental data has shown that niobium, as it is used in SRF application, traps almost 100% of any ambient field under certain conditions [31, 45]. If the involved mechanisms that lead to either flux expulsion or trapping are understood, the gained knowledge could be used to maximize expulsion and minimize trapping. Thereby, the RF dissipation could be reduced, even in the presence of ambient fields. A detailed understanding of the underlying mechanisms and knowledge on how optimized flux expulsion can be achieved reproducibly in an accelerator environment is important, especially in the context of recent projects that rely on high- Q cavities.

The LCLS-II light source, as one example, is the first accelerator that will employ N-doped cavities. As discussed in Section 2.3 and shown in the experiments in Section 3.4, N-doped cavities exhibit reduced BCS losses while their RF dissipation for the same amount of trapped flux is increased. Until about five years ago, the research on trapped flux losses in SRF cavities was narrow. Furthermore, the estimation of the magnetic field that a cavity is exposed to in an accelerator is not trivial. SRF cavities are installed in modules together with magnets. The cavities are cooled down before the magnets start operation. Thereby, their influence is minimized. Once the cavities are superconducting, the magnets cannot degrade the RF performance further, as long as the resulting field anywhere at a cavity stays below the critical field of niobium.

However, cavities do not stay superconducting all the time and as soon as they are warmed again or quenched they will be exposed to the ambient field. Furthermore, the module's vacuum vessels and other components are fabricated from steel and with time the magnets inside the modules can start to magnetize any iron- or nickel-containing components. Hence, even when all magnets are turned off, the ambient field in the module may grow with time and it will become increasingly challenging to expel all magnetic field during phase transition.

Considering the size and the design specifications of an accelerator like LCLS-II, trapped magnetic flux emerges as one of the main challenges for the project because the ambient field and extent of flux expulsion are parameters that are difficult to predict for a whole module and at the same time trapped flux is a major loss contribution in the cavities.

In the past, different strategies to maximize flux expulsion have been pursued and tests with cavities have yielded results that seem to contradict tests on samples. What both have in common is that either experiment found a way to significantly improve flux expulsion. The next sections will give an overview of the literature on flux expulsion during superconducting phase transition and summarize proposed models. The topic contains numerous open questions, which in their entirety are out of the scope of this thesis. Only two very specific issues, which are important for SRF cavities, will be addressed in dedicated sample experiments.

5.1 The Kinetics of the Phase Transition in Superconductors

The thermodynamics of the superconducting phase transition are well understood and in good agreement with experimental findings. The majority of the research focuses on equilibrium parameters. The transition itself is however, as the name says, a transition between different equilibrium states. While the normal state, the Shubnikov phase, intermediate state and Meissner state are understood, questions remain e.g. on the nature of the phase front and its propagation speed.

The Phase Front

The key to understanding flux trapping and expulsion lies in the phase front, which expands into the normal conducting state. The conditions at the front influence whether a flux line is expelled or gets trapped. Some experimental studies even

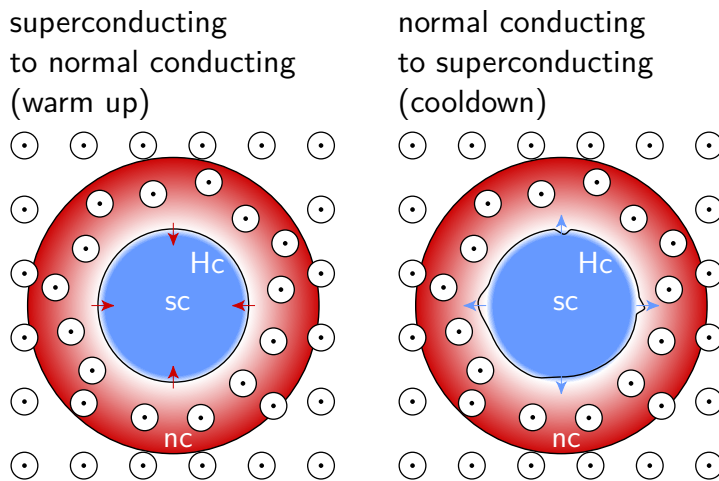


Figure 5.1: A rod in a longitudinal magnetic field during superconducting phase transition. Displacement of flux is easier closer to the surface of the rod. Hence the situation on the left hand side, where the front grows inwards e.g. during warm up, is stabilized. The opposing situation where the front expands outwards, e.g. during cooldown, is destabilized.

found, that complete expulsion or trapping can be achieved in the same cavity just by changing cooling dynamics [33].

During a cavity cooldown, the temperature is continuously lowered from room temperature to below T_c . The niobium transitions first into the Shubnikov phase when $B < B_{c2}(T)$ and then into the (incomplete) Meissner state when $B < B_{c1}(T)$. The vast majority of publications on phase front propagation, in contrast, evaluate the front that is driven by the a change in applied magnetic field at a constant temperature. This kind of transition is much more stable in the experiment and easier to describe in terms of material parameters, which often depend on temperature. The physics behind the transition, however, should not depend strongly on whether T or B is changed.

The first description of the phase propagation was given in 1955 and combined theoretical work by Pippard with experimental results by Faber [66]. Their model assumes a type-I superconductor. They considered a cylindrical rod with a superconducting core and a normal conducting region surrounding it (Figure 5.1). The superconducting area is in complete Meissner state. The normal region is penetrated by a magnetic field that is parallel to the rod. When the superconducting phase advances, latent heat is generated at the boundary and magnetic flux is displaced in front of it. The heat must escape the sample and thereby a gradient of temperature is established. The same applies to the flux, which is expelled from the material. When it is driven through the normal conducting material, it induces eddy currents while a gradient in field strength is established. As a result, H and T are higher on the phase boundary than at the surface of the sample.

The thermal diffusivity in pure metals at low temperatures is high, therefore the

latent heat escapes much more easily than the flux and the temperature gradient is very small. The latent heat can thus be disregarded for most practical purposes and only the eddy currents need to be taken into account. They dampen the motion of the phase propagation and determine the speed of the phase boundary.

The expulsion of flux needs less energy when the flux is close to the outside surface of the cylinder and more energy the longer the way through the material is for the flux. Hence, the closer the front is to the outside surface, the less difficulty it experiences in displacing flux through the intervening normal phase. This leads to very different situations depending on whether the boundary moves inwards or outwards or, whether the superconductivity establishes during cooldown or is destroyed during warm up.

When the front moves inwards, parts that move faster need more energy to displace the magnetic flux. They slow down. Parts that move slower need less energy to displace the flux and hence speed up. The front is naturally stabilized. For the inverted case, when the front grows outwards, the front is destabilized because regions that run ahead are closer to the outside surface and need less energy to displace the flux and regions that lag behind are further thwarted. Any irregularity thus is rapidly magnified.

Nucleation, Growth and Spinodal Decomposition

In contrast to type-I superconductors, on which the model of Pippard and Faber is based, type-II superconductors have negative surface tension, which can cause additional destabilization at the phase front because it causes a maximization of the total interface area. Later studies included type-II superconductors and their properties in experimental and theoretical investigations. The resulting model resembled the description of a solid phase that grows into a supercooled melt.

There are two length scales that influence the growth of the superconducting phase, λ and ξ . Based on time-dependent Ginzburg-Landau equations that calculate the dynamics of the superconducting order parameter $\psi(r, t)$ and the electromagnetic vector potential $A(r, t)$, two dynamic regimes were described: The nucleation regime, where a superconducting seed establishes and subsequently grows and the “spinodal” regime [67, 68]. The spinodal regime applies for external magnetic fields below H_{sp} , which is called the “spinodal field” and is equal to H_{c2} in type-II superconductors. There is no free-energy barrier to nucleation of the superconducting phase in that regime. Therefore, arbitrarily small seeds can grow [68]. The phases rapidly separate and generic features like dendritic patterns establish.

It was also calculated that the propagation of the fronts depends strongly on the amount of flux that is trapped in the front [69]. Many more studies investigated the different forms of phase fronts and parameters that impact them. A detailed summary is beyond of the scope of this thesis. However, for the following sections, which address the phase front in SRF science, it is important to keep in mind that the phase front in a type-II superconductor is far from trivial.

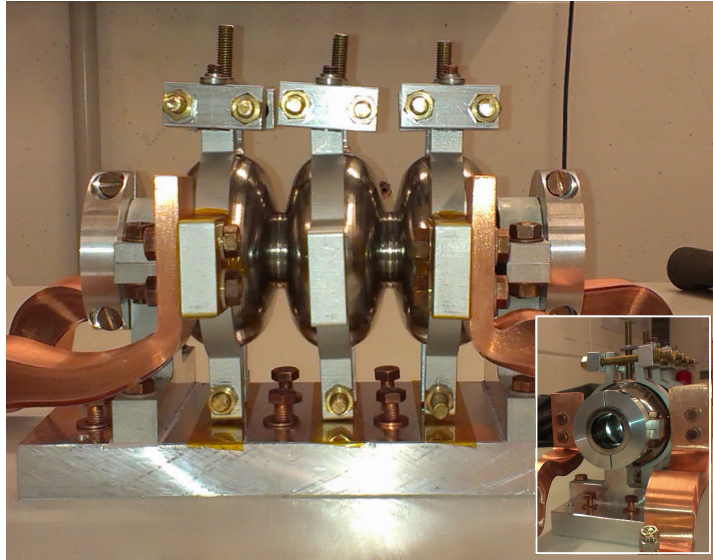
5.2 Recent Progress in SRF Science

The investigation of flux trapping in SRF cavities gained momentum after experimental tests on niobium samples indicated that the fraction of flux that gets trapped during phase transition was impacted by the treatment (bake-out and surface etching) as well as the crystal structure and the cooling rate [45]. In the experiment, the best sample (single crystal, BCP and 1200°C bake) trapped only 42% of the applied field while a polycrystalline sample with no treatment trapped 100%. Furthermore, the single crystal samples showed a logarithmic increase of trapped flux with the cooling rate. The increase was later reproduced on a niobium rod [17] and on a sample in a Quadrupole Resonator [70]. All these studies agreed that a reduction in cooldown speed improved flux expulsion.

Test on cavities in a vertical test assembly, however, yielded a contradicting result [33, 71]. The usually good R_s values measured in the vertical tests degraded drastically when the cooldown speed was reduced. A proposed cause was that, during a fast cooldown, the superconducting phase grew from the bottom to the top and thereby swept the flux out. When the cooling speed was reduced, the number of nucleation spots increased. The flux lines got encircled by superconducting areas and were unable to leave the material. The expulsion was suppressed. This scenario is however only conceivable for magnetic flux lines that are perpendicular to the surface of the superconductor and rejects the complexity of the phase front as it was discussed above. The studies further found a correlation of the residual resistance with the spatial temperature difference over a cavity cell and no correlation with the cooldown rate.

In 2015, a theoretical model was presented that was able to fit the experimental data of this cavity tests [72]. The author assumed a planar phase front with a linear temperature gradient around T_c . The temperature gradient was translated into a spatial distribution with two phase fronts at $B = B_{c1}(T)$ and $B = B_{c2}(T)$ that separated

Figure 5.2: Photo of the 3 GHz three-cell cavity with brackets and posts. The copper straps were later bolted to the 4.2 K table inside HoBiCaT.



a normal conducting region, a region in the Shubnikov phase and one in the (incomplete) Meissner state. The number of trapped flux lines was calculated based on a beam-target collision model where the pinning centers and the flux lines corresponded to beams and a target. A linear dependence on the inverse spatial temperature gradient was deduced. Though the model successfully fitted one experimental data set, the underlying assumptions of two plane phase fronts and a linear temperature gradient are simplified and the model leaves no room to explain the results on samples.

The next section will present a study, which investigates the flux expulsion in a conduction cooled cavity, which is in-between a convection cooled cavity in an RF test and a plane, conduction cooled sample. The test targets the question whether the contradictory results are caused by the different geometry of cavities and samples or by the different cooling schemes. The results will be discussed in the context of the models presented in this section.

5.3 Tests on Samples

5.3.1 3 GHz Cavity

The first sample was a small, elliptical three-cell 3 GHz cavity that was fabricated from niobium. Because the cavity had no tank for LHe, it was clamped in brackets and placed on posts at the beam pipes and at the three equators. Copper straps were attached to the brackets. For the test, the cavity was positioned on the support table in HoBiCaT that was cooled to 4.2 K and the copper straps were bolted to the table.

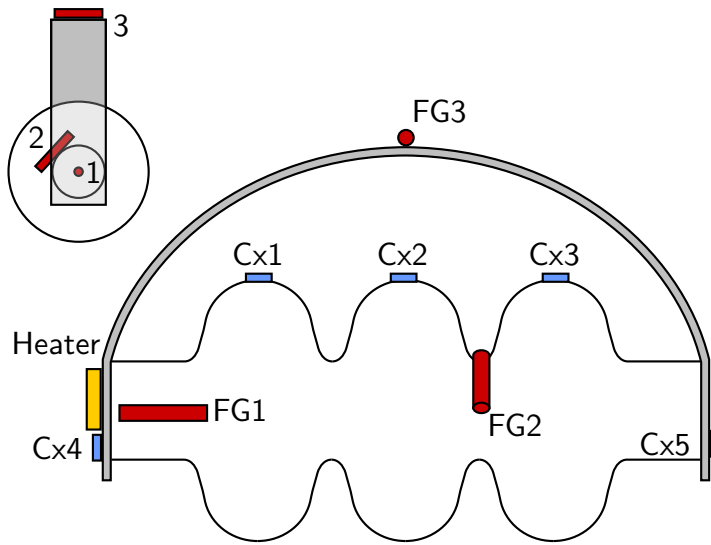


Figure 5.3: Setup of the 3 GHz cavity with three fluxgates FG (red) and five Cernox sensors Cx (blue). The ends of the cavity were shorted by a titanium sheet. The small insert at the top left shows the setup from the side with the numbers of the FGs.

The cavity was thus conduction cooled as it is typical for a sample while it had the geometry of cavity, which is usually convection cooled.

Setup and Instrumentation

The cavity was equipped with Cernox and fluxgate sensors. In addition, the two ends were shorted by a thin titanium sheet to mimic a LHe tank because the setup was also intended for investigation of thermocurrents that will however not be further discussed here. Figure 5.3 displays the position of temperature and magnetic field probes. After the setup was installed in HoBiCaT and cooled to operating temperature, the cavity was alternately warmed above T_c using a heater and left to cool down again. The magnetic signal during the cycles was different for each FG depending on its position and orientation. The magnetic field along the axis of the cavity was mainly caused by the shielded earth's field while the thermocurrent in the cavity was in azimuthal orientation and almost zero inside the cavity. Hence, FG2 and FG3 showed mainly magnetic field changes due to thermoelectric currents and FG1 almost exclusively registered step-like changes due to the expulsion of the shielded earth's magnetic field during the sc phase transition.

During the test, the setup exhibited a different behavior than was expected. The heater was intended to create a temperature gradient along the cavity. After it was turned off, it was expected that the side opposing the heater would transition first into the superconducting state. However, due to the limited heat conduction in the posts and brackets and thermal contact issues, the gradient along the cavity was altered. The side close to the heater was much better cooled and transitioned first.

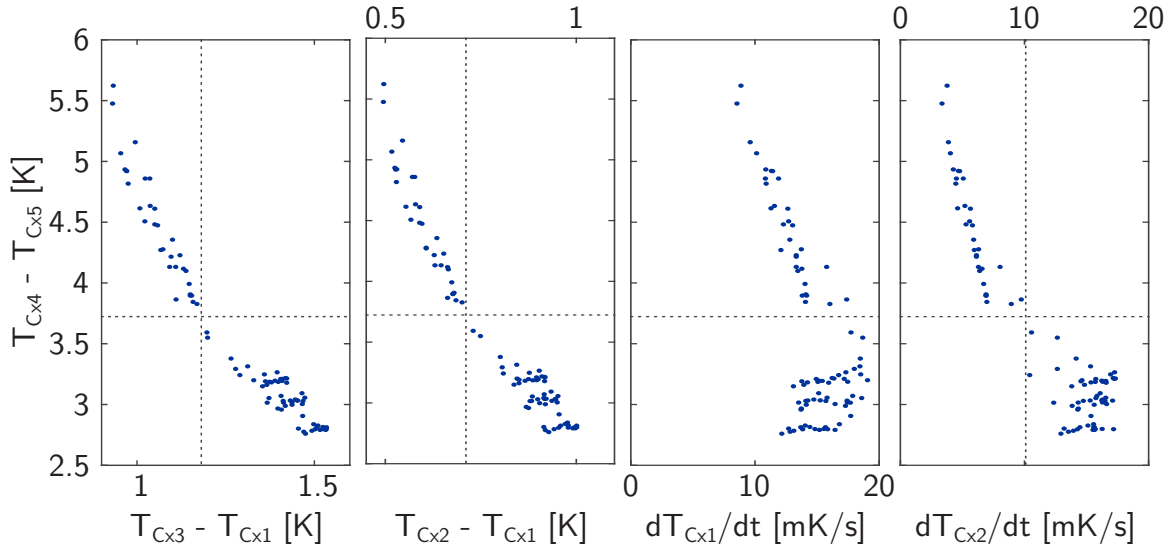


Figure 5.4: Various cooling parameters for evaluation of the 3 GHz cavity test: Temperature difference between Cx 5 and Cx 4 as a function of the temperature difference between sensors 3 and 1, as well as between 2 and 1, and as a function of the cooling rate measured at Cx 1 and Cx 2. All parameters were taken at the instance when Cx 1 dropped below T_c . The quadrants are for later use.

The gradient along the cavity was thus diminished and inverted during the cooling phase. The interpretation of the magnetic field data must therefore be done carefully.

Cooling Parameters

As in the previously described RF tests, the first challenge in the data analysis was the definition of the relevant cooling parameters. One can evaluate the measured magnetic field as a function of the temperature difference between the sensors at the Nb-Ti contacts (Cx 4 and Cx 5) for thermoelectric considerations or as a function of the difference between the sensors on the equators (Cx 1, 2 and 3) for the evaluation of flux expulsion. In any case, all measured parameters were correlated as shown in Figure 5.4. A large difference between Cx 4 and 5 coincided with a small temperature difference between the equators and a small cooling rate - and vice versa.

Reproducibility

Before the change in flux expulsion for the two groups was evaluated, it had to be determined whether the same cooling conditions lead to reproducible results. To achieve that the temperature of the cavity was set close to the transition temperature. An instability in the cryoplant that only occurred during this one measurement campaign caused an oscillation in temperature that forced the niobium to periodically change

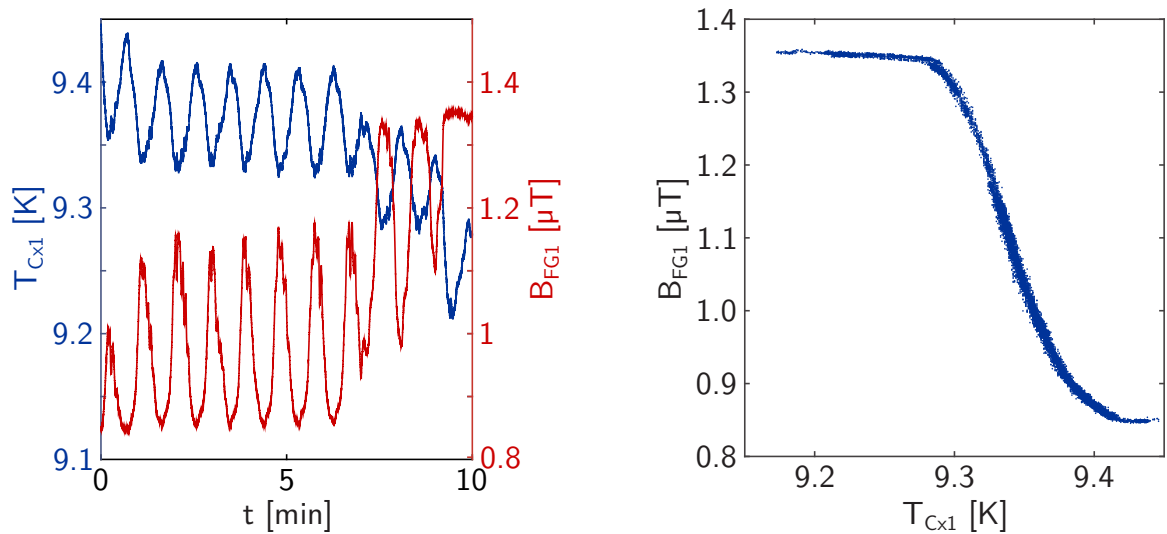


Figure 5.5: Temperature at Cx1 and magnetic field at FG1 during an oscillation of the cavity temperature around the transition temperature.

phase without changing heater settings. Figure 5.5 shows the acquired temperature and magnetic field data. All Cernox sensors on the cavity registered the temperature oscillation. However, only FG1 measured a similar variation in magnetic field. It can be concluded that the signal was caused by the phase front that was repeatedly passing it when the niobium changed phase. In Figure 5.5, the magnetic field measured by FG 1 is also plotted versus the temperature measured by Cx 1. The figure includes all 11 oscillations acquired during the displayed 10 minutes. An increase from 0.85 to 1.36 μT was repeatedly achieved due to flux expulsion that removed magnetic field from the material and hence increases the field density outside the material. The temperature spread of the transition seems to be rather broad, which is due to the measurements setup. The fluxgate is about 3 cm long and parallel to the cavity surface. It starts to register a change in field once the phase front approaches it from one end and keeps measuring flux that is expelled until it has spread all the way to the other end. Based on this plot it can be concluded that phase transitions under similar conditions caused reproducibly the same flux expulsion.

Expulsion Behavior

The change in flux expulsion between different cooling conditions can be evaluated based on the data of FG1. The probe was oriented along the cavity axis, which is the best orientation for addressing flux expulsion because it is the main orientation of the shielded earth's field. In order to be able to compare the different transitions,

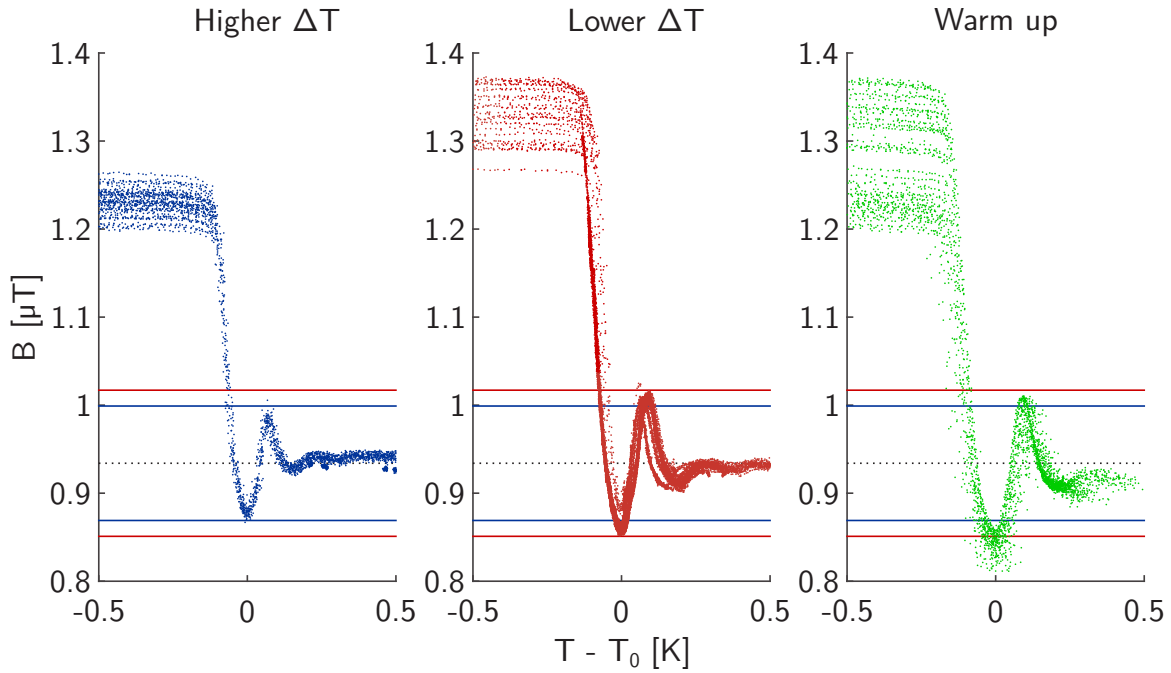


Figure 5.6: Magnetic field measured by FG1 during the normal to superconducting phase transitions and during the super- to normal conducting transitions. The abscissas display the temperature measured with Cx 1 minus T_0 , which is the temperature when the magnetic field reached its minimum in each transition.

the measured magnetic field during all transitions is plotted versus the temperature of Cx 1 in Figure 5.6.

Concerning the normal to superconducting phase transitions, the figure shows that the level of magnetic field in the superconducting state exhibits a spread while the level before the transition, indicated by the dashed line, is always similar. In general, the measured field values in the superconducting state are higher for transitions with a lower ΔT values (between Cx1 and Cx2) compared to higher ΔT values. That indicates that more flux was expelled. The transitions with lower or higher ΔT are separated by the dashed lines in Figure 5.4.

Furthermore, the overshoot-like feature is visible at T_0 (explained in the figure caption). The amplitudes of this features are indicated by the solid blue and red lines. When the superconducting phase front moved along the material and expelled flux, the flux was driven ahead of it. Hence the magnetic field density was increased in the normal conducting volume in front of the already superconducting material. When the field enhanced area passed the fluxgate, it caused this features. According to Reference [66], the amplitude of the peak is increased if either the amount of expelled flux is raised or if the boundary is moving faster. Since the transitions with

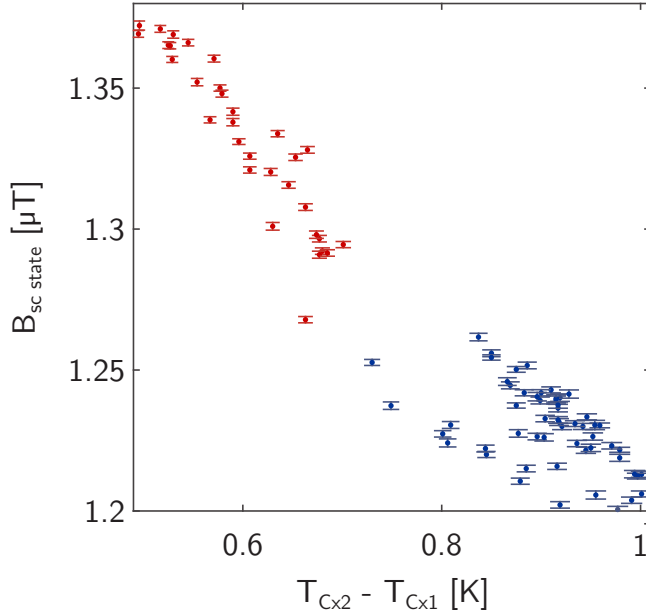


Figure 5.7: The expelled magnetic field measured in the superconducting state as a function of temperature difference between the cavity equators.

lower ΔT have also lower cooling rates (shown in Figure 5.4), a faster moving phase front is unlikely to be the cause of the higher peak amplitudes. It is much more probable that the elevated peaks indicate increased flux expulsion, which matches the higher levels of magnetic field measured after transitions with lower ΔT values.

The last plot in Figure 5.6 shows how the magnetic field enters the material after the cavity is warmed above transition temperature. Again, the peaks due to the increased magnetic field density are visible as the phase front passes the fluxgate and the spread in magnetic field between the various data sets present in the superconducting state vanishes once the material is normal conducting again.

Figure 5.7 shows the level of magnetic field measured in the superconducting state as a function of $T_{C_{x2}} - T_{C_{x1}}$. We can conclude that the best flux expulsion was obtained when the niobium was cooled in a reduced temperature difference, which also coincided with a lower cooling rate. This result is in agreement with the previously discussed sample experiments but not with the RF tests on cavities, which will be addressed in the discussion in Section 5.4.

What the tests with fluxgate could not make accessible is the actual flux inside the material. FGs can only ever measure indirectly the change in magnetic field density with some distance to the niobium. Furthermore, the spatial resolution is very low because the probe averages over its length. Therefore, a technique that opens the possibility to measure the flux closer to the niobium and with much higher resolution will be introduced in the next section.

5.3.2 Magneto-optical Imaging

The last method that will be introduced in this thesis is magneto-optic (MO) imaging. It measures the stray field outside the sample similar to a fluxgate. MO imaging, however, has the advantage over a fluxgate that it enables the user to take a picture of the magnetic field distribution right at the surface of the sample and not just measure one average value. Furthermore, the pictures are taken quickly and hence MO imaging is able to visualize dynamic magnetization processes. Reference [73] provides a comprehensive overview over MO microscopy, though mainly in the context of magnetic domains in ferromagnetic materials. It will be used as basis for the following introduction of the method.

MO Effects and Setup

MO observations are based on the Kerr and the Faraday effects, which occur in materials with magnetic circular birefringence and dichroism. The birefringence arises from different refractive indices of circularly polarized components of light that lead to a rotation of plane of polarization of linearly polarized light. The dichroism originates from a difference in absorption coefficients of left- and right-handed circular polarized light in a medium.

For the Faraday effect, the plane of polarization of a light beam is rotated during transmission through a magnetized and transparent medium. For the Kerr effect, the plane of polarization of the light is rotated during reflection from a magnetized and reflective sample [73].

The measurements for this thesis were performed at the Leibnitz Institute for Solid State and Material Research Dresden in collaboration with the group of Prof. R. Schäfer. The functional principle of the technique will only be explained briefly. Figures 5.8 and 5.10 depict the setup. The photos show the optical microscope with cryostat and helium supply. The material for the samples was high purity niobium provided by Heraeus. It was cut in two small cylinders of 5 mm height and with diameters of 5 mm and 10 mm. The samples did not receive any heat treatment or surface polish. Figure 5.9 shows a microscopic image, which was obtained of the sample surface with several machining marks. The goal was to maximize the number of pinning centers and hence the probability of flux trapping. Thereby, it was easier to evaluate the distribution of trapped flux in the superconducting state. If most flux was be expelled instead of trapped, it would be more difficult to get an MO image

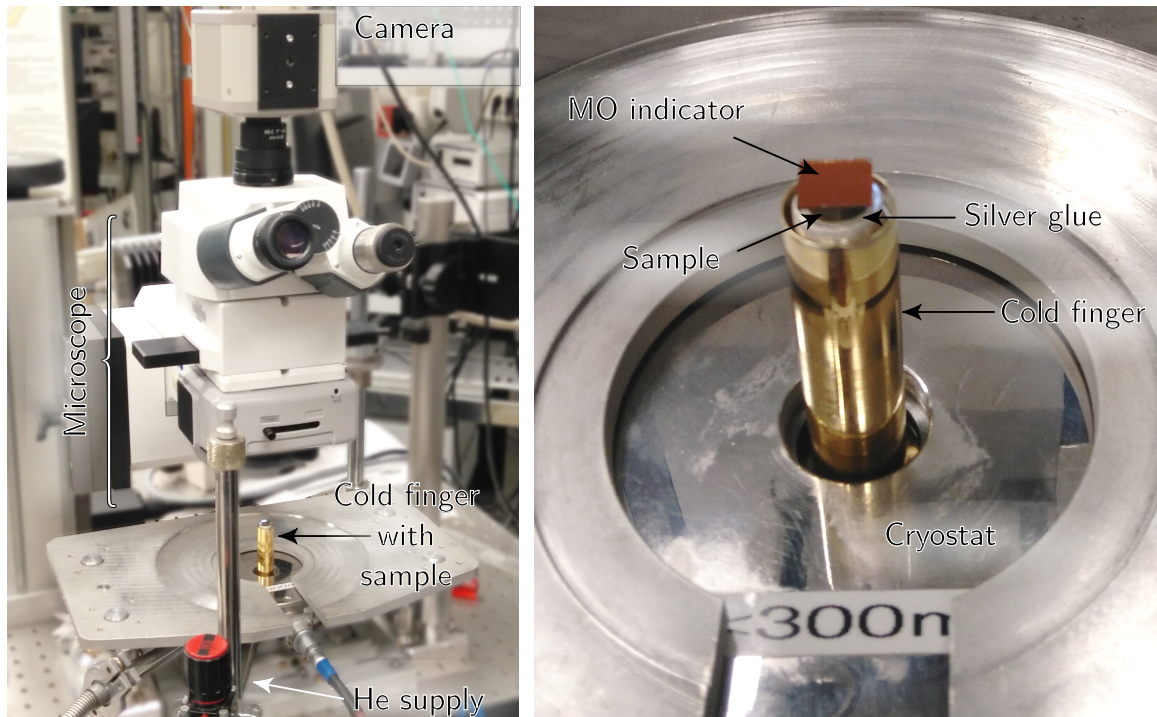


Figure 5.8: Photo of the MO imaging setup.

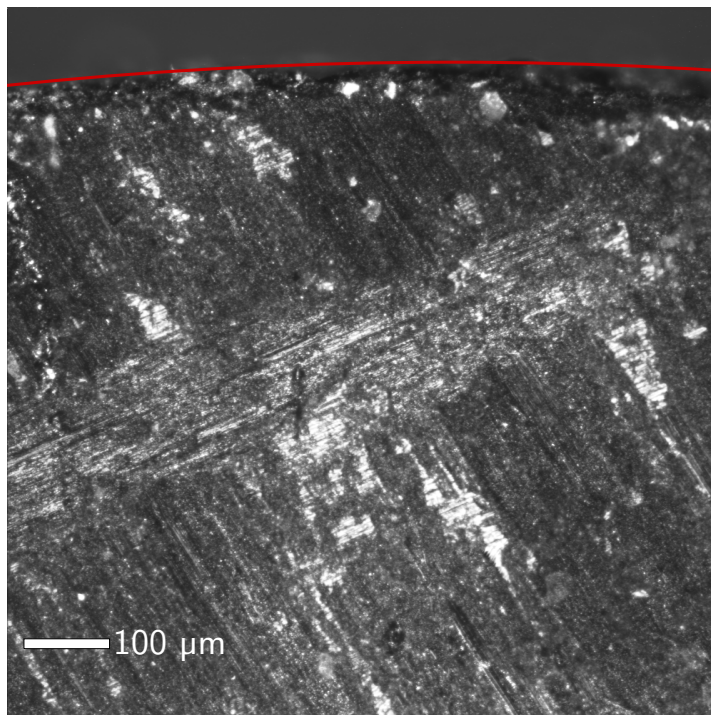


Figure 5.9: Microscopic image of the sample surface (magnification 10x, 10 mm-diameter sample). The red line indicates the edge of the sample. Several machining marks are visible as scratches.

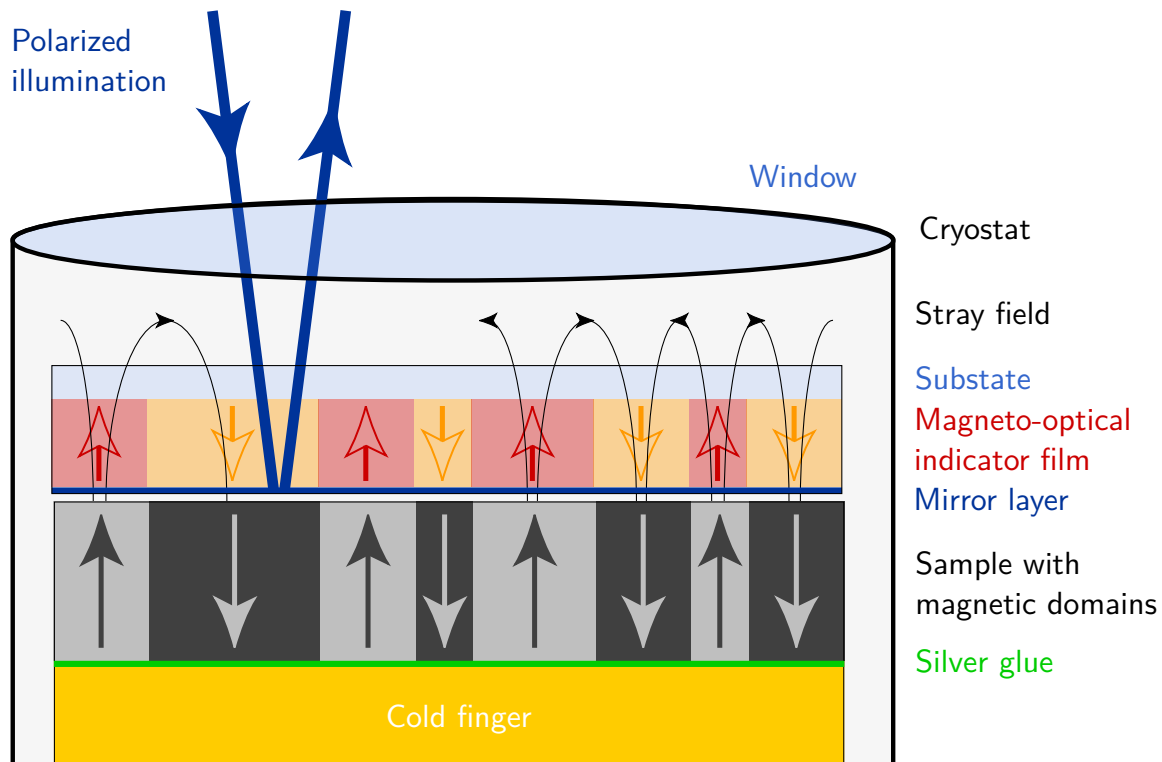


Figure 5.10: Setup of imaging magnetic domains with a magneto-optical indicator film. The stray field from the sample causes a response in the magneto-optical indicator film, which is imaged by polarized light. The light is reflected at the mirror layer between indicator and sample. Light blue parts are transparent. [73]

because an indicator film was used, as will be explained below. In addition to the trapped flux after sc phase transition, the advancing phase front was imaged.

For the experiment, the sample was placed on top of the cold finger, with silver glue in-between to ensure good thermal contact. The magnetic field inside the niobium was not imaged with the MO technique. However, the stray field of the sample was visualized by an indicator material. The indicator was placed on top of the sample. It consisted of a magnetic film with an in-plane magnetic anisotropy as a detection layer, a mirror layer at the bottom and a transparent substrate at the top. The magnetization in the indicator film was altered in correspondence with local stray fields generated from the sample and the altered magnetization was imaged in reflection with the MO microscope using polarized light and an analyzer. The following sections will summarize the obtained results.

Flux Penetration Pattern - The Magnetic Field Loop

In order to achieve a first impression for the images produced by MO technique, a “magnetic field loop” was performed. Figure 5.11 shows the sequence of the applied magnetic field. Initially, the sample was zero field cooled. Then the applied field was continuously increased up to 93 mT and subsequently lowered back to zero. Next, the field was increased again, but with opposite sign to -80 mT, lowered to zero again, increased with positive sign to a slightly lower value and so on.

Figure 5.12 shows the resulting images for the 10 mm diameter sample and a magnification of 2.5. Each image was taken as an average over 16 shots. Small defects in the indicator film caused minor artifacts like white and black dots that did not change with the applied field.

The first image (a) shows the sample after it was cooled to 4K in zero field. Since the magnetic field applied later during the test was in the mT range, zero field meant no applied field. The earth’s field was still present. Then, a magnetic field was applied pointing out of the paper plane (b). The field was increased until the lower critical field was reached at the sample’s edge and the field started to enter in dendric patterns (c to f). The machining marks on the surface, which were shown in the microscopic image of the sample in Figure 5.9, were preferred locations for the flux to penetrate. In Figure 5.13, the field pattern of Figure 5.12(d) is directly compared to the machining marks. Previous studies in References [74] and [75] also investigated the flux penetration in niobium with MO imaging and found a similar preferred flux penetration at defects.

In addition to the magnetic field in the sample, the applied field was also imaged because the indicator was larger than the sample. Figures 5.12(b) to (f) show an increase in grey scale value outside the sample (top region in each figure) when the applied field was increased. Stepping from Figure (f) to (g), the external magnetic field was turned off after it had penetrated almost the whole field of view.

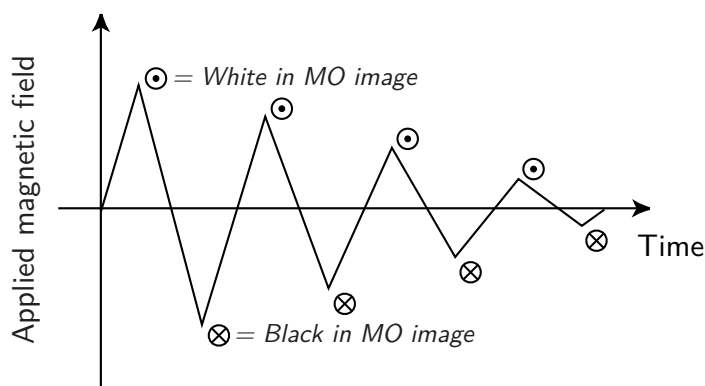


Figure 5.11: Sequence of the applied magnetic field during the magnetic field loop.

5. Flux Trapping and Flux Expulsion

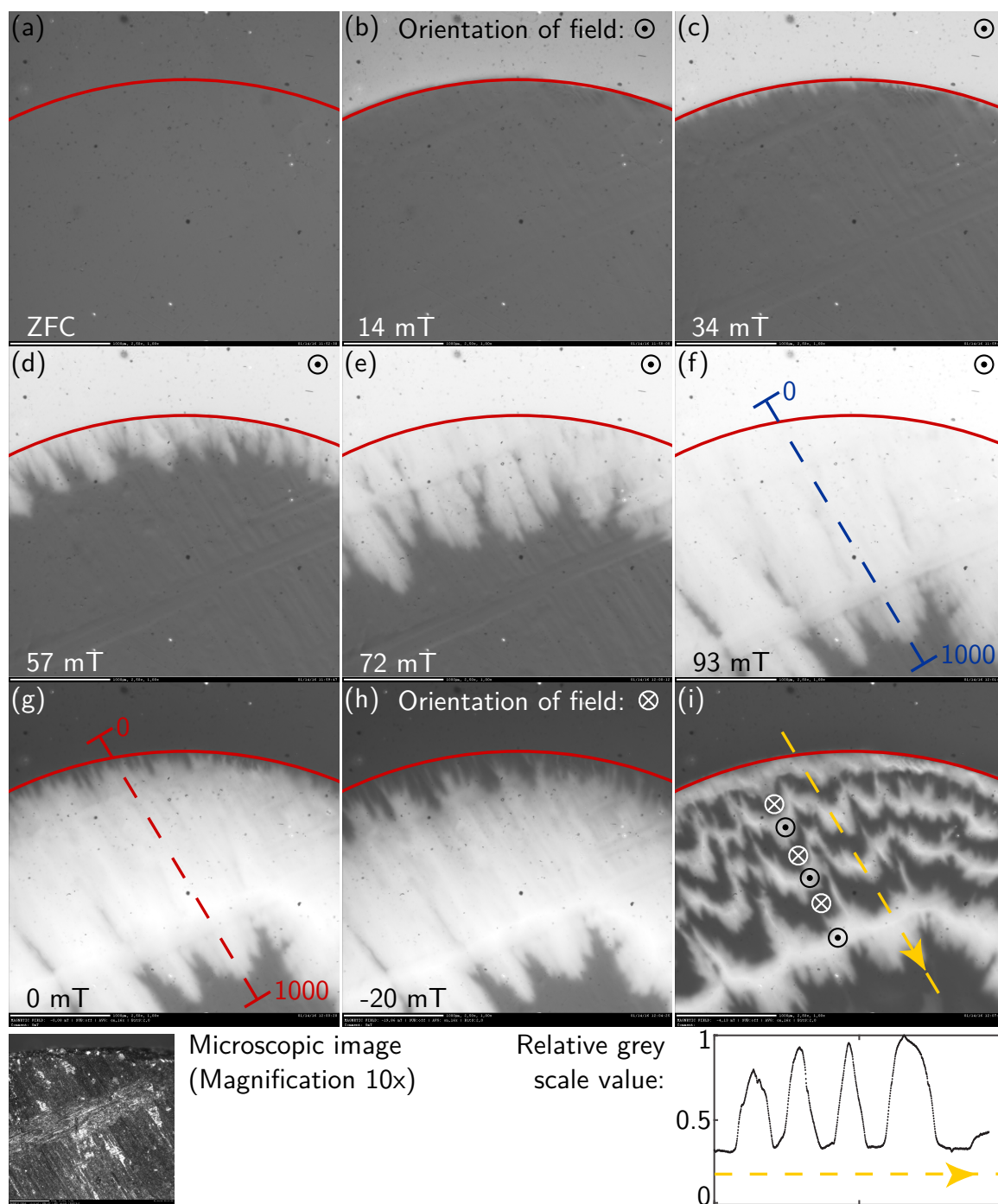


Figure 5.12: Magnetic field loop: Sample with 10 mm diameter, magnification 2.5, cooled in zero field (ZFC). Subsequently, a magnetic field was applied according to the sequence in Figure 5.11 until the striped pattern of trapped flux established inside the sample. The orientation of the applied field is given in the top right corner of (b) - (f) and (h). No external field was applied in (a), (g) and (i). The line plot below (i) gives the relative grey scale value along the yellow dashed line.

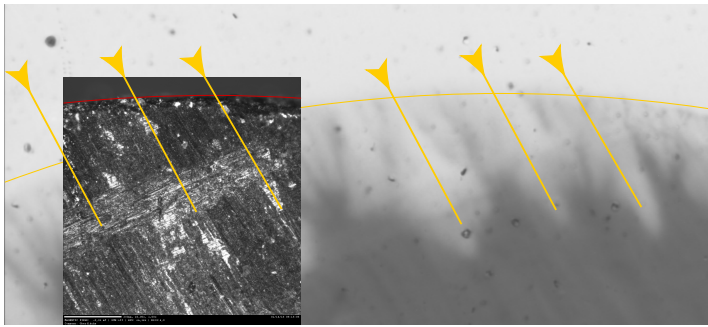


Figure 5.13: Direct comparison of the machining marks and the flux penetration pattern (Figure 5.12(d)).

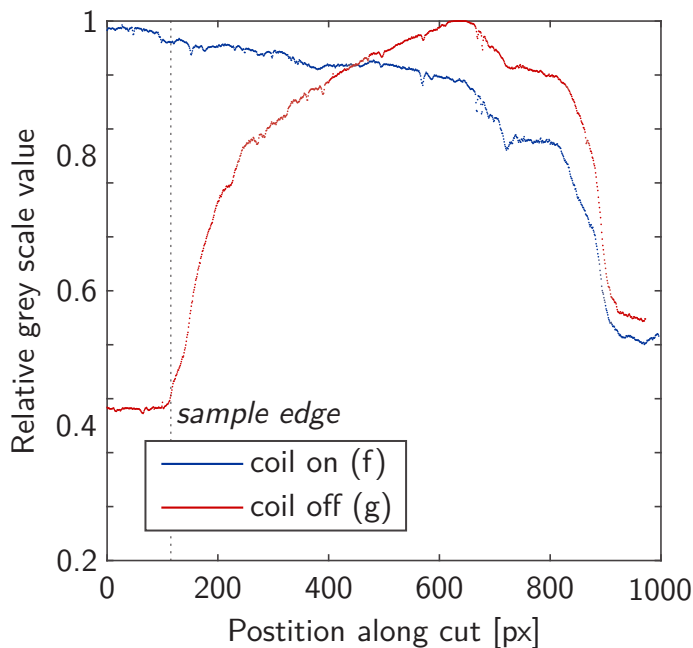


Figure 5.14: The relative grey scale values exported along the blue and red dashed lines in Figures 5.12(f) and (g).

Figure 5.14 shows the relative grey scale values exported along the blue and red dashed lines in Figure 5.12 normalized to the maximum value. The comparison of the two curves confirms that a large portion of the applied magnetic field got trapped inside the sample when the magnetic field was turned off.

After the magnetic field was reduced to zero, the loop sequence was further executed until a striped pattern established in the sample indicating frozen in magnetic flux after each cycle with alternating signs (Figure 5.12(i)). A line plot of the grey scale values of the stripes was exported along the yellow dashed line and is given below the corresponding image. The images show that the sign of the trapped magnetic flux was alternating and that the amplitude of the trapped flux was decreasing towards the edge of the sample. Therefore, the sample displayed trapped flux according to the history of the applied magnetic field.

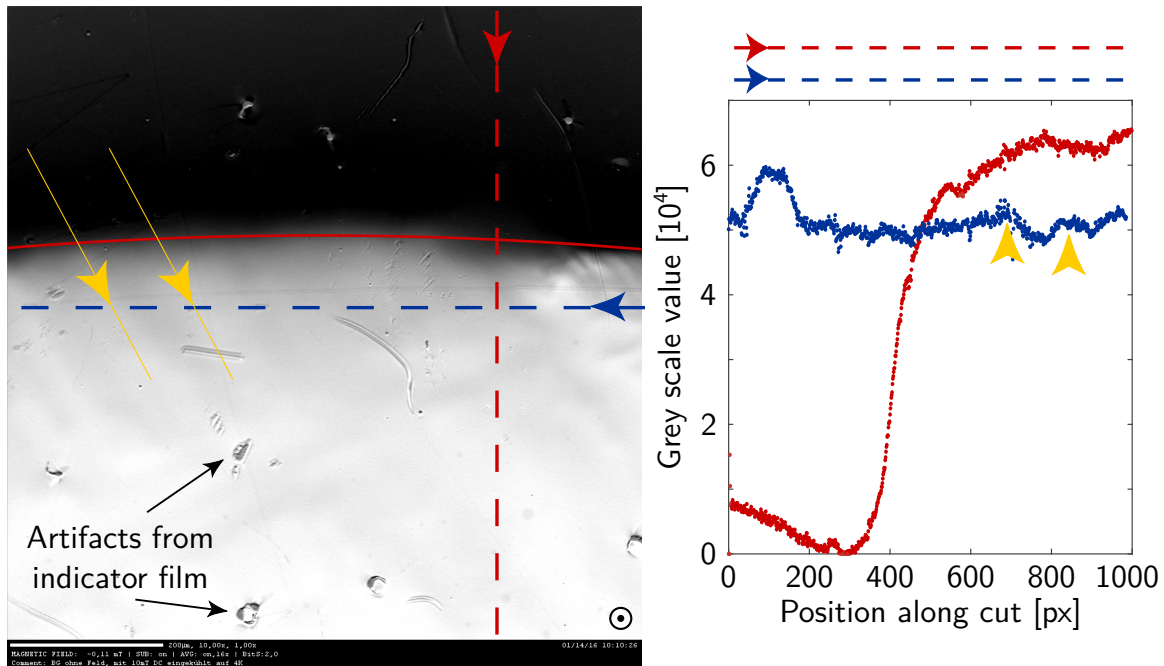


Figure 5.15: Trapped flux after field cooling in 10 mT (magnification 10x).

Trapped Flux After Cooldown

As the next step, the magnetic field before the cooldown was changed (field cooled measurement) and the distribution of the trapped flux was evaluated. Figure 5.15 shows the obtained image after a cooldown in 10 mT and two line plots exported from the image (red and blue). A background image was taken prior to the cooldown and subtracted in order to improve contrast.

The figure shows that the trapped flux was distributed over the whole sample that was in the field of view, though the grey scale value decreased towards the edge. That can indicate a small change in trapped flux but is more likely caused by the change in stray field density close to the edge while the trapped flux itself did not decrease. Furthermore, the grey scale values of the red cut line reached a minimum outside the sample but close to its edge, which indicates a field in opposite direction. It was caused the magnetic field lines that must form a close loop outside the sample and hence point in the opposite direction at that position.

Despite the subtraction of the background image, artifacts caused by defects in the indicator film are visible. They appear sharp because the microscope was focused on the indicator. Other features are more blurred. The blue cut line shows a variation in field between pixels 600 and 1000 that was not caused by the indicator film but indicates a local variation of trapped flux (yellow markers). The darker and brighter

lines in the MO image follow the machining marks on the surface that were discussed previously.

Finally, the external field was turned on again while the sample was still superconducting. The field was increased until the grey scale value outside the sample was the same as inside, which was achieved at 10.6 mT indicating that almost all of the applied field was trapped during the cooldown.

The experiment was repeated with applied field of 20 mT and 50 mT yielding similar results: The grey scale values were decreasing towards the edge and reached a minimum outside the sample close to the edge. Features in the field distribution appeared at the positions of the machining marks. By fixing the grey scale and exposure time, it was further found that the amount of trapped flux increased with applied field.

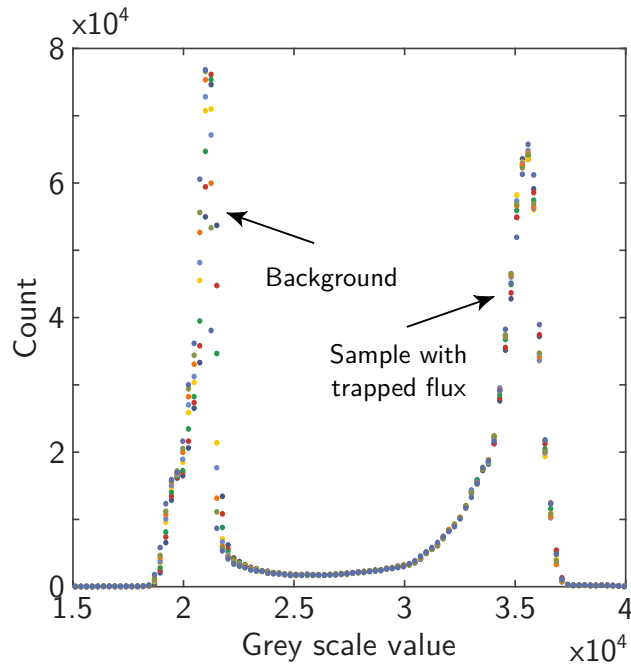
Variation of Cooling Conditions

Furthermore, the cooling conditions were altered. In order to change the cooling speed or temperature gradient over the sample during the sc phase transition, the start temperature measured at the cold finger was altered between close to T_c and 30 K. In addition, the helium flow through the cryostat was manually de- and increased. A constant field of 10 mT was applied during the cooldown and turned off before taking the MO images in the superconducting state.

For the evaluation of a change in trapped flux, the exposure time and grey scale were fixed to obtain comparable conditions in the images. The grey scale data of each image was converted into a histogram. The histograms exhibited two peaks. The first peak at a higher grey scale value corresponded to the level of trapped flux inside the sample. If the level of trapped flux increased, this peak would shift to a higher grey scale value. The peak at a lower values indicated the background, which was visible at the top of each image. This peak should stay constant since no magnetic field was applied when the picture was taken.

Figure 5.16 shows the histograms for eight images obtained under different conditions. The trapped flux peak is less sharp than the background peak because the grey scale value varied over the sample. Since the shape of the peak was reproducible this was probably caused by an inhomogeneous illumination of the image. The positions of the two peaks did not change between the eight histograms. Therefore, it can be concluded that the level of trapped flux was not significantly altered by the variations in cooling conditions.

Figure 5.16: Histograms obtained from MO images after eight different cooldowns with various start temperatures and helium flow levels.



Phase Front Propagation

Finally, the most advantageous property of MO imaging was employed: the short exposure times. Movies with a frame rate of 10 Hz were shot during the cooldown of the two samples. When a sample was cooled in a static field, the phase transition only caused a change in the image close to the sample edge since almost all flux was trapped. In order to see the phase transition also far away from the edge, AC fields were applied instead of the DC field. The applied fields may impact the dynamics of the phase front, which must be kept in mind when the results are evaluated.

First, the smaller sample (5 mm diameter) was cool in a field with 5 mT amplitude and 6 Hz frequency. Second, the larger sample (10 mm diameter) was cool in a field with 10 mT amplitude and 12 Hz frequency. Figure 5.17 shows frames from the movies in 0.1 s steps and the trapped flux pattern obtained after the external field was turned off. The frames were post processed with a median filter (5 px) to minimize the artifacts due to the indicator film and the brightness was adjusted to improve contrast.

For both samples, the phase transition started at the center and moved towards the edge of the sample. The alternating magnetic field was trapped accordingly. The innermost area was black hence the field was pointing into the paper plane (see Figure 5.12) when the phase transition started and was trapped in that direction. The superconducting phase front moved outwards and the sample trapped the applied field as it was decreasing, passing zero and increasing again with opposite sign reaching its maximum value, which is indicated white, and so on.

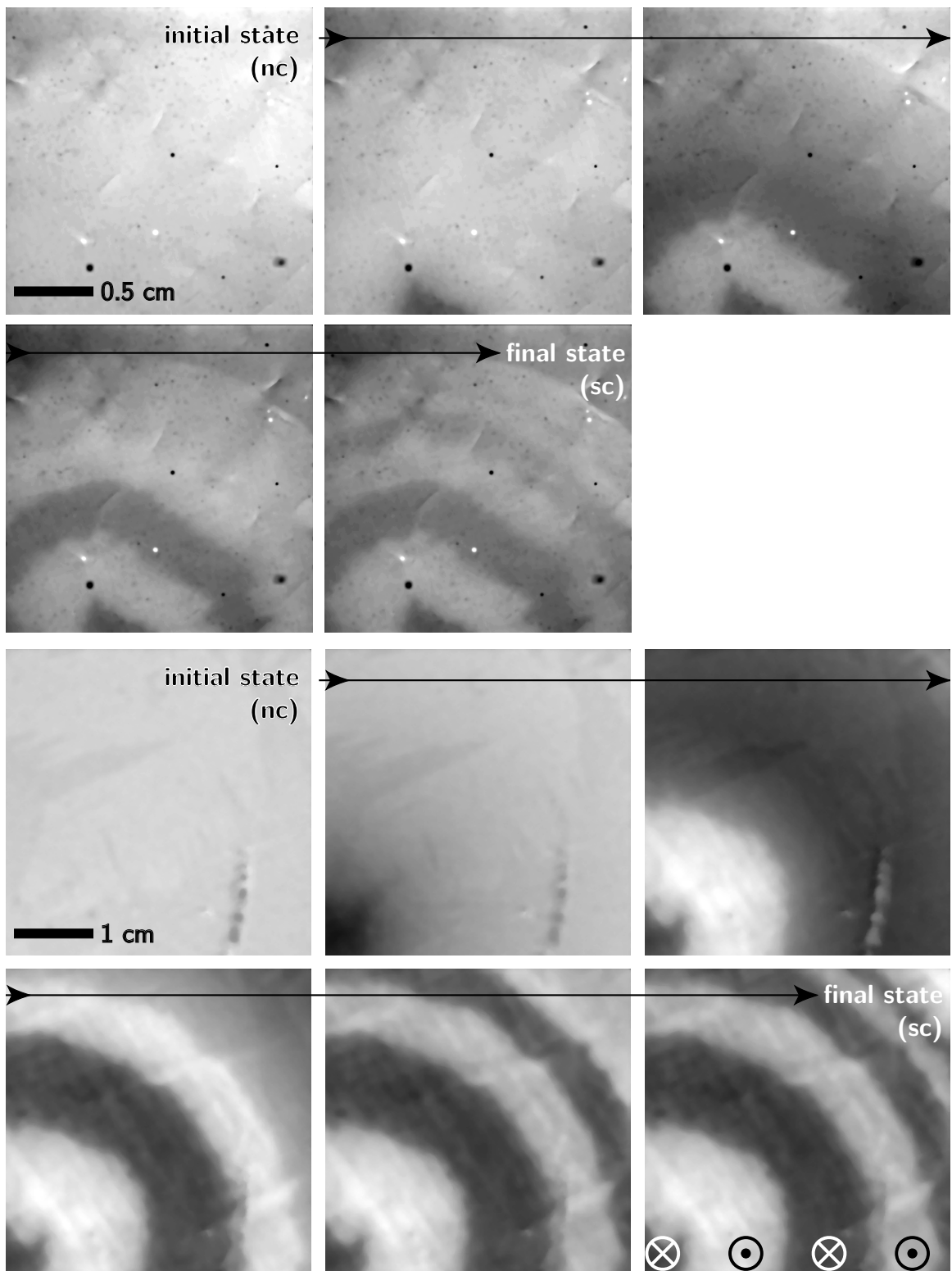
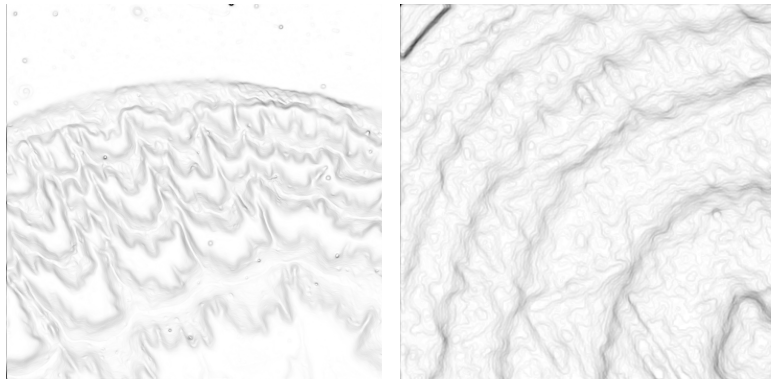


Figure 5.17: Phase front propagation during cooldown of Top: the 5 mm sample in an AC field of 5 mT amplitude and 6 Hz frequency (magnification 2.5). Bottom: the 10 mm sample in an AC field of 10 mT amplitude and 12 Hz frequency (magnification 1.25).

Figure 5.18: Contours of trapped flux pattern that indicate the shape of the phase front.

Left: for a magnetic field loop.

Right: for a cooldown in AC field. (final image of Figure 5.17 but different detail)



By tracing lines of the same grey scale value, the shape and movement of the phase front can be estimated. The final image in Figure 5.17 can be compared to the magnetic field loop performed previously (Figure 5.12). The contours of the two images were carved out and are displayed in Figure 5.18. Both images were obtained with the same sample but with different fields of view. The different magnification was compensated so that the images can be compared directly with each other. The contours resulting from a superconducting phase growing outwards appear to be smoother than the contours caused by flux penetration because the dendric patterns are missing. In Section 5.1, it had been discussed that two factors determine the phase front propagation: the latent heat, which is generated at the boundary and must be conducted away and the magnetic flux, which must be displaced. Pippard had argued that the heat can be neglected and that the process is dominated by the flux expulsion. Under this assumption, however, the obtained MO images should look similar. We must consider that the theoretical model describes the phase transition at a constant temperature where only the applied magnetic field is in- or decreased. In the experiment, in contrast, the temperature was reduces and while the latent heat due to phase transition was still small, the heat in the material itself was not. It had to be conducted away in order to reduce the sample temperature. In conclusion, one possible explanation for the qualitatively different MO images is that the flux penetration experiment was dominated by flux dynamics. It showed the expected dendric patterns and the machining marks on the surface had a large impact on the shape of the inwards growing phase front. The AC experiment, on the other hand, was dominated by heat transport of the bulk material, which is much more homogeneous. Therefore, the dendric patterns did not form.

5.4 Discussion: Flux Trapping and Flux Expulsion

Two major conclusion can be drawn from the previous sections. First, the tests demonstrated how trapped flux increases with ambient field if cooling conditions are kept within a certain window. In the MO experiments, actually no cooling conditions were found to change the percentage of flux that was trapped. It can be concluded that a larger range of cooling conditions must be explored here. However, in the experiments with the 3 GHz cavity the flux expulsion could be altered. The conditions that increased expulsions were those of a smoother cooldown with reduced cooling rates and temperature gradients, which is in agreement with earlier tests on samples but opposes vertical tests on convection cooled cavities. It can now be concluded that the geometry difference between samples and cavities did not cause these contradicting results but the different cooling probably did.

At this point, the dynamics of the phase front should be included in the discussion of flux expulsion in the SRF context. Most literature that was also presented in the beginning of this chapter treats the phase front that propagates when an ambient field in- or decreases. The MO images have shown that the predictions from theory drawn under those conditions are not necessarily the same for a superconducting phase that is growing due to a reduction in temperature. One of the predictions was, for example, that the front of a growing superconducting phase is destabilized by flux expulsion while the front of a growing normal conducting phase is stabilized by it. The statement was made under the assumption of a cylindrical sample with a superconducting core and a normal conducting edge, which applies to the MO setup. The experiments, however, showed that the growing superconducting phase front is not destabilized but, in contrast, exhibits less features like the dendric patterns than the phase front caused by flux penetration. This qualitative difference may have a major impact on flux expulsion.

Despite the promising results, it must be acknowledged that the MO imaging needed applied magnetic fields in the mT range, which is a higher magnitude than the cavity tests that usually operate in the μT range. Flux expulsion dynamics may differ between the two regimes. Furthermore, SRF cavities have less defects and smoother surfaces than the samples used in this thesis. Nevertheless, a better understanding of the phase front dynamics based on these findings may resolve the contradicting results between convection cooled cavities and conduction cooled samples.

Chapter 6

Summary and Outlook

This thesis targeted residual losses in SRF cavities that are caused by trapped magnetic flux. The aim was to identify the origin of trapped flux and investigate means to minimize it. Two main questions were pursued. First, the creation of additional ambient magnetic field by the thermoelectric effect in a cavity-tank system was analyzed in detail. This field occurs inside the cavity-tank-system during the cooldown and can therefore not be reduced by improvement of the magnetic shielding that surrounds it. The second part of the thesis focused on improvement of the expulsion of ambient magnetic field during phase transition.

6.1 Conclusions

6.1.1 Thermocurrents

RF Cavity Tests

Q vs. E_{acc} measurements of high- Q cavities in horizontal assemblies [14, 15] had indicated that the residual losses are often larger than in preceding vertical testing and would change if the cooldown conditions were altered. In this thesis, the effect was investigated by systematically varying the experimental conditions. Additional information on the spatial distribution of the losses in the cavity was obtained by recording Q data not only from the accelerating π mode but also two further passband modes. The results substantiated the claim that the additional surface resistance was caused by trapped, thermoelectrically generated, magnetic flux. Two techniques developed to vary the cool-down conditions were named “thermal cycling” and “parked cooldown”. They allowed for minimization of the trapped magnetic flux down to an average surface resistance of $1.4 \text{ n}\Omega$ measured in the $1/9 \pi$ mode. This corresponded to a quality factor of more than 10^{11} at 1.5 K. Thereby, it was also demonstrated that trapped

flux is the main contribution to residual losses in high- Q cavities and hence the key to their further improvement.

It was shown, that the thermoelectric effect significantly (but reversibly) degraded cavities with a BCP surface treatment ($\approx 10 \text{ n}\Omega$ additional surface resistance) and even more so nitrogen annealed cavities ($\approx 20 \text{ n}\Omega$ additional surface resistance).

Simulations and Direct Measurement

The magnetic field produced by thermocurrents was measured directly inside the LHe tank close to the outer cavity wall. It was shown how the field depended on the temperatures of the two niobium-titanium joints and the field distribution was modeled in numerical simulations. The simulations demonstrated how the mechanically symmetric system exhibited a non-symmetric current distribution following a variation in temperature-dependent DC resistance. Thereby, a magnetic field was generated inside the cavity, which would otherwise have been field free for a symmetric current distribution.

Furthermore, the emerging and growing superconducting area was investigated. The fluxgates inside the tank registered a peak in magnetic field caused by the phase transition. The peak's amplitude was correlated with the residual losses in later operation. The simulations showed that the peak height was given by the amount of thermocurrent in the system thus explaining the correlation with RF dissipation. In addition, the simulations illustrated how the shape of the peak is caused by the expansion of the superconducting area with zero DC resistance.

The orientation of the field inside the cavity was calculated to be orthogonal to the temperature gradient that caused the asymmetry. Based on that finding, magnetic field sensors were placed inside a cavity, orthogonal to its axis, to monitor the magnetic field during thermal cycles. Trapped flux of up to $8.3 \mu\text{T}$ was observed. The measured level of trapped flux was highest in the cells that transitioned first. It decreased the more, the later a cell transitioned because the temperature difference driving the thermocurrent as well as the thermopower of the involved materials was decreasing with time. Furthermore, it was found that more flux was trapped in the bottom of the cells than in the top, which corresponded to the lower local DC resistance and hence higher magnetic field closer to the liquid helium, which was also predicted by the simulations.

In summary, the RF tests, simulations and direct measurements were in good agreement and thereby thermocurrents were proven to be a significant source of RF dissipation in horizontal cavity operation.

Measurement of Thermopower

This thesis also provided directly measured values for the Thermopower values of niobium and titanium at cryogenic temperatures. The material properties were determined as input parameters for the numerical simulations of the cavity-tank system but can likewise be applied in other contexts in the future. A table with the obtained values is given in Appendix D.

6.1.2 Flux Expulsion

The final part of the thesis focused on improvement of flux expulsion during phase transition and targeted two specific topics. First, flux expulsion was improved for a conduction cooled 3 GHz cavity. The change was achieved by a reduction of the cooldown rate and the temperature gradient over the cavity. The result is in accordance with previous tests on samples that were *conduction cooled* [17, 45, 70] and differs from the observations on *convection cooled* cavities [33, 71]. It was concluded that the contradicting results were not caused by the different geometry of samples and cavities but more likely by the different cooling scheme.

Second, the shape of the proceeding phase front was imaged using magneto-optical imaging. It was shown that the shape differs significantly between the case of a superconducting area that grows from the inside out during the cooldown and the case of an applied magnetic field that penetrates the superconductor from the outside. This difference is a hint that different shaped phase fronts may explain the observed differences in flux expulsion.

6.2 Outlook

The research presented in this thesis triggered an increased interest in trapped flux and awareness of its importance in the SRF community. Now, we know that in state of the art cavities trapped flux is distinctly the main contribution to the residual losses and the recent progress allows to tailor the cooling scheme of SRF cavities to the needs. A thermal cycle of a cryo module following the initial cooldown from room temperature can allow for the targeted temperature distribution to both minimize ambient field and maximize flux expulsion to ensure the preservation of high quality factors.

Future research may solve the open questions concerning the flux expulsion differences between convection and conduction cooled niobium. The theory that fitted

the results obtained with cavities [72] has (to date) no parameters to account for the different results obtained in samples. Hence, a comprehensive theory to describe flux expulsion under the various cooling conditions is still lacking and may be accomplished by incorporating phase front dynamics. Further experimental studies on that topic could be performed using MO imaging with samples that do not trap almost any applied field but exhibit measurable flux expulsion during phase transition, e.g. heat treated samples. The tests would complement the data presented in this thesis.

New insights could also be obtained from a system that is able to map magnetic field similar to the established temperature mapping systems [76]. With such a system, the temperature and the magnetic field distribution over a cavity could simultaneously be monitored during the cooldown and also during operation. It would require a large number of magnetic field sensors to cover the whole outer surface of a cavity. Therefore, AMR sensors were tested in the context of this thesis (Appendix E). First, encouraging results indicated that a resolution of 25 nT was obtained at cryogenic temperatures in vacuum. A combination of temperature and magnetic field mapping would allow further investigation of all trapped flux related questions directly at a cavity as well as studies on flux trapping and expulsion during e.g. quench with a direct measurement of both temperature and magnetic field.

Appendices

Appendix A

The Thermoelectric Effect: Charge and Heat Currents

The equations for charge and heat current are given by

$$\begin{aligned}\mathbf{J} &= \mathcal{L}_{11}\mathbf{E} + \mathcal{L}_{12}\nabla T, \\ \mathbf{Q} &= \mathcal{L}_{21}\mathbf{E} + \mathcal{L}_{22}\nabla T.\end{aligned}\tag{A.1}$$

The equations relate the electrical current density \mathbf{J} and the heat current density \mathbf{Q} to the voltage and temperature gradients. These parameters are reasonable for an experimental setup. The material properties, as the Seebeck coefficient, the thermal conductivity and the electrical conductivity, are hidden in the 3×3 tensors \mathcal{L}_{ij} .

A stringent theoretical description follows the Onsager relations [42]. The Onsager reciprocal relations express the equality of certain ratios between fluxes and forces in thermodynamic systems out of equilibrium, but where a notion of local equilibrium exists. The transport coefficients \mathcal{L}_{ij} must therefore be transferred to a generalized transport coefficient $\mathbf{L}_{ij}^{\mu\nu}$ leading to a reformulation of Equation A.1

$$J_i^\mu = \sum_{j\nu} \mathbf{L}_{ij}^{\mu\nu}(H) F_j^\nu\tag{A.2}$$

where the Onsager relation

$$\mathbf{L}_{ij}^{\mu\nu}(H) = \mathbf{L}_{ji}^{\nu\mu}(-H)\tag{A.3}$$

is valid. Now, we must find the correct form of the forces. To achieve that, Reference [42] evaluates the rate of entropy production, the rate of irreversible heat production and the equation of continuity the correct conjugate forces in the transport equation where the temperature enters the equation. The final result is a description of

thermoelectric transport, which now satisfies the Onsager relation:

$$\begin{aligned}\mathbf{J} &= \mathbf{L}_{11} \frac{1}{T} \mathbf{E} - \mathbf{L}_{12} \frac{1}{T^2} \nabla T \\ \mathbf{Q} &= \mathbf{L}_{21} \frac{1}{T} \mathbf{E} - \mathbf{L}_{22} \frac{1}{T^2} \nabla T.\end{aligned}\tag{A.4}$$

At this point, the coefficients \mathbf{L}_{ij} can be related to experimentally measured material properties. We can use $\mathbf{J} = \sigma \mathbf{E}$ to obtain the isothermal conductivity σ_t as

$$\sigma_t = \frac{1}{T} \mathbf{L}_{11}.\tag{A.5}$$

Furthermore, we can determine the thermoelectric power under open-circuit conditions $\mathbf{J} = 0$ to

$$\mathbf{S} = \mathbf{L}_{21} \mathbf{L}_{11}^{-1} / T.\tag{A.6}$$

Appendix B

The Fluxgate Magnetometer in Detail

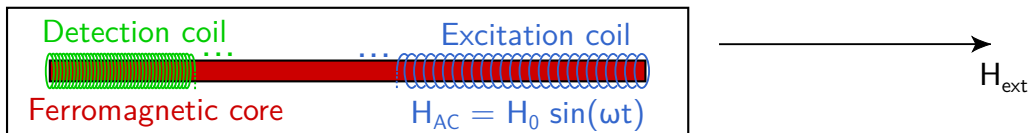


Figure B.1: Sketch of a fluxgate magnetometer.

Figure B.1 reproduces the setup of a fluxgate magnetometer from Figure 2.17. The FG can measure the magnetic field in one spatial direction that is the one of the core axis (red). The excitation coil (blue) creates an AC magnetic field

$$H_{AC} = H_0 \sin(\omega t), \quad (\text{B.1})$$

which oscillates with a frequency in the order of 10 kHz and with an amplitude in the order of 10 mT. The AC field drives the ferromagnetic core into saturation. The detection coil (green) is exposed to the alternating field B in the core and a voltage V_{ind} is induced. It which depends on its number of windings n and its cross-sectional area A as [47]

$$V_{\text{ind}} = nA \frac{dB}{dt}. \quad (\text{B.2})$$

The magnetic field B and thereby its time derivative are given by the magnetization curve of the core. The curve can be approximated with a cubic polynomial in H [77]

$$B(H) = aH^3 + bH \quad (\text{B.3})$$

where a and b are parameters that depend on core material properties as the permeability. In the absence of any external field, the detected field is equal and opposed to the excitation field. If an external field H_{ext} is present, the two signals differ. The

magnetic field in the core is then a superposition of the induced field H_{AC} and the external field H_{ext} , which is set smaller than H_{AC} [47]

$$H = H_{AC} + H_{ext}. \quad (B.4)$$

By combination of Equations B.2, B.3 and B.4, the induced voltage thus expands to

$$\begin{aligned} V_{ind} &= nA \frac{d}{dt} [a (H_{ext} + H_0 \sin(\omega t))^3 + b (H_{ext} + H_0 \sin(\omega t))] \\ &= nA\omega \left[\left(3aH_{ext}^2 H_0 + bH_0 + \frac{3}{4}aH_0^3 \right) \cdot \cos(\omega t) \right. \\ &\quad \left. + \left(3aH_0^2 H_{ext} \right) \cdot \sin(2\omega t) \right. \\ &\quad \left. + \left(\frac{3}{4}aH_0^3 \right) \cdot \cos(3\omega t) \right]. \end{aligned} \quad (B.5)$$

The harmonic decomposition of the induced voltage yields a linear dependence of the second harmonic's amplitude at 2ω on H_{ext} . The FG's read out unit uses this dependence and converts the transformed and filtered signal into a magnetic field value. A FG can detect DC fields as well as AC fields. The resolution is 1 nT and the precision about 10 nT. The spatial resolution is given by the length of the core. The latter must be accounted for when the FG is used in an inhomogeneous magnetic field.

Appendix C

The AMR Sensor in Detail

The anisotropic magnetoresistive effect describes that the electrical resistance in ferromagnetic materials depends on the angle between the material's magnetization and the current flowing inside it. Recent magnetometer devices based on AMR use thin films, which change their resistance by a few percent in the presence of a magnetic field [44]. During fabrication, the films are deposited in a strong magnetic field and thereby the preferred orientation of the magnetization vector \mathbf{M} , called "easy axis", is set parallel to the length of the resistor. Figure C.1 shows an AMR thin film. If an external magnetic field is applied perpendicular to the easy axis, \mathbf{M} will rotate. The angle between \mathbf{M} and the current \mathbf{I} will change leading to a change in resistance. The Figure also displays the change in resistance as a function of angle between \mathbf{M} and \mathbf{I} . The resistance is maximum if they are in parallel and minimum if they are perpendicular to each other. With this setup, the external magnetic field component perpendicular to the easy axis (but in the plane of the thin films) can be measured because it rotates \mathbf{M} while \mathbf{I} keeps its direction. The resistance exhibits a linear region around 45° . Hence, shorting bars are positioned on the thin films at a 45° angle. Their resistance is very low while the AMR's resistance is in the $k\Omega$ range. The current is therefore forced to flow at a 45° angle to the easy axis and the operating point is shifted to the center of the linear region.

Since this change in resistance due to an external magnetic field is small (just a few percent), the AMR thin films are usually assembled as a Wheatstone bridge as displayed in Figure C.2. The supply voltage V_b is provided between bottom and top contacts of the bridge. The output voltage V_{out} is tapped between the right and the left contacts. In first approximation the four resistances are the same $R = R_1 = R_2 = R_3 = R_4$. The change caused by the magnetic field now defines the output voltage of

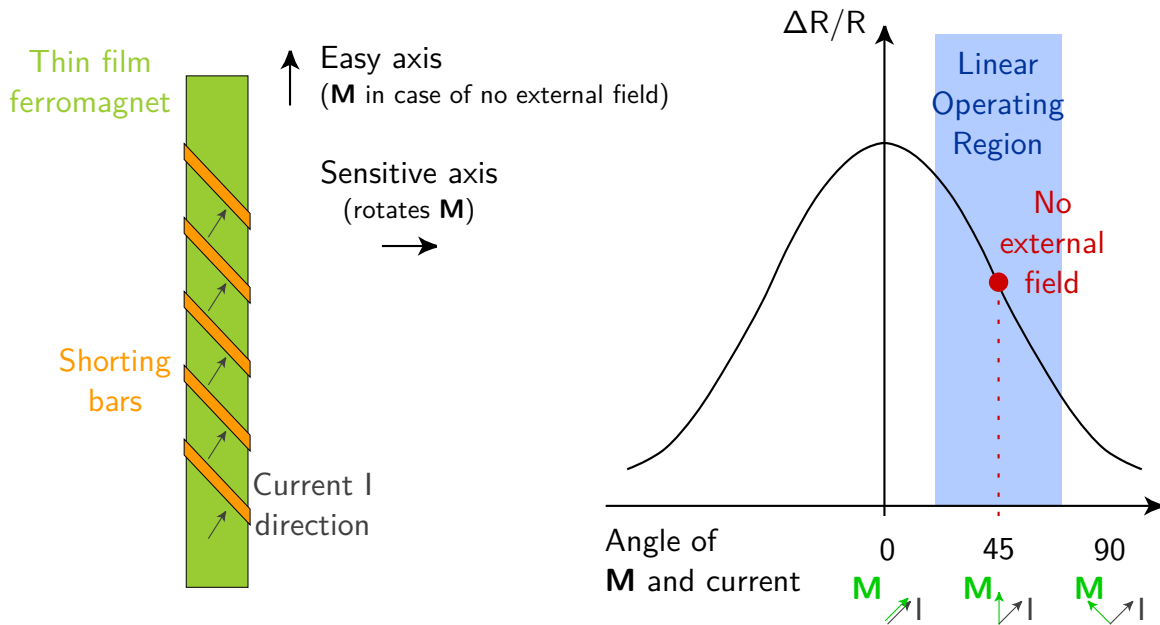


Figure C.1: AMR sensor: Ferromagnetic thin film with 45° shorting bars. The magnetization vector \mathbf{M} is orientated along the easy axis for no external field. If a field is applied, \mathbf{M} is rotated. The Figure is adapted from Reference [44].

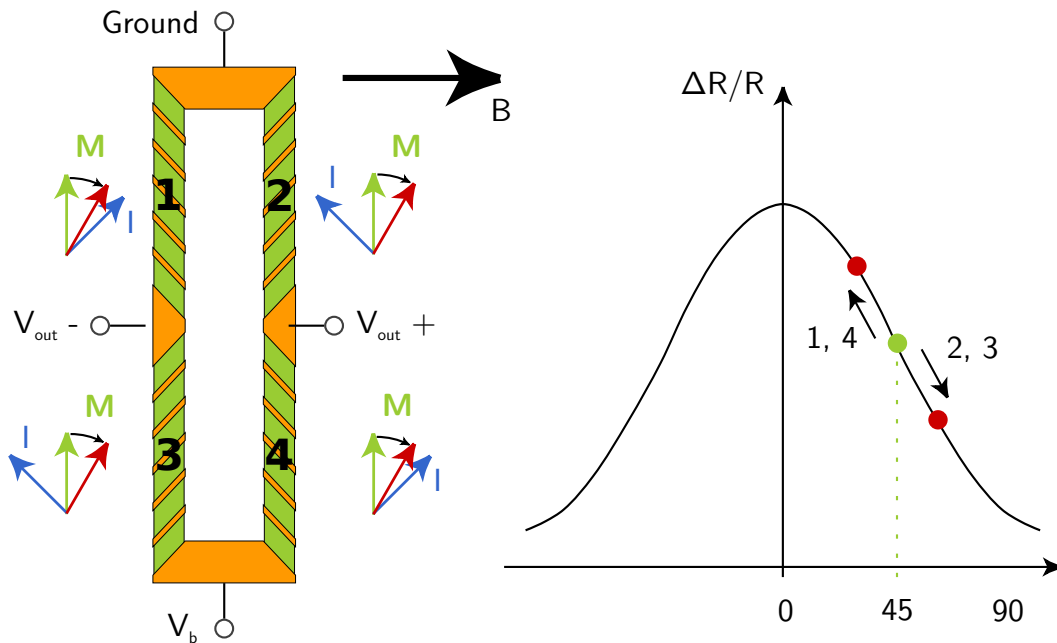


Figure C.2: AMR sensor with typical Wheatstone bridge of four ferromagnetic thin films with 45° shorting bars. The magnetization vector \mathbf{M} equals the superposition of the magnetization of the thin films in the easy axis \mathbf{M} with an external field \mathbf{B} . The Figure is adapted from Reference [44].

the bridge as

$$\frac{V_{\text{out}}}{V_{\text{b}}} = \frac{1}{4} \left(\frac{\Delta R_1}{R} - \frac{\Delta R_2}{R} - \frac{\Delta R_3}{R} + \frac{\Delta R_4}{R} \right). \quad (\text{C.1})$$

In the linear operating region, the change in resistance is similar for the four resistors but with different sign due to the setup of the different shorting bars

$$\Delta R = \Delta R_1 = -\Delta R_2 = -\Delta R_3 = \Delta R_4 \quad (\text{C.2})$$

and hence the output signal is given as

$$V_{\text{out}} = \frac{\Delta R}{R} \cdot V_{\text{b}}. \quad (\text{C.3})$$

In contrast, the voltage drop over just one single ARM is $V = (R + \Delta R)I$, where the relative change is much harder to measure because $\Delta R \ll R$.

Appendix D

Measured Thermopower Values as a Table

Table D.1: Thermopower S of niobium and titanium between 10 K and 100 K. The numbers were retrieved from polynomial fits to the experimental results.

T [K]	S_{Nb} [$\mu\text{V K}^{-1}$]	S_{Ti} [$\mu\text{V K}^{-1}$]	T [K]	S_{Nb} [$\mu\text{V K}^{-1}$]	S_{Ti} [$\mu\text{V K}^{-1}$]
10	-0.156	-0.176	56	2.920	-3.340
12	0.057	-0.254	58	2.973	-3.274
14	0.261	-0.386	60	3.020	-3.193
16	0.456	-0.563	62	3.059	-3.099
18	0.644	-0.772	64	3.091	-2.995
20	0.823	-1.003	66	3.117	-2.883
22	0.995	-1.249	68	3.135	-2.765
24	1.160	-1.502	70	3.146	-2.643
26	1.318	-1.754	72	3.150	-2.517
28	1.470	-2.000	74	3.148	-2.391
30	1.615	-2.236	76	3.139	-2.264
32	1.754	-2.456	78	3.125	-2.138
34	1.886	-2.658	80	3.104	-2.013
36	2.013	-2.840	82	3.078	-1.889
38	2.132	-2.998	84	3.047	-1.766
40	2.246	-3.132	86	3.012	-1.642
42	2.353	-3.242	88	2.974	-1.516
44	2.454	-3.326	90	2.932	-1.385
46	2.549	-3.385	92	2.888	-1.247
48	2.636	-3.420	94	2.842	-1.098
50	2.717	-3.431	96	2.797	-0.933
52	2.792	-3.420	98	2.751	-0.746
54	2.859	-3.389	100	2.708	-0.532

Appendix E

AMR Sensors for SRF Application

This Appendix will treat the data that was measured with the AMR sensors in the experiment presented in Section 4.4. Eight AMRs and six FGs were mounted inside the cavity. Their positions are given in Figure E.1. For better orientation in the data, the sensors were color and marker coded: triangles for FGs in the top, circles for FGs in the bottom, squares for AMRs; green for FGs in cell 1, red for cell 5 and blue for cell 9. The AMRs were positioned at the irises and hence were colored with different shades of brown according to their position between cell 1 and 5 and blue for the one close to cell 9. Three of the eight AMRs (AMR4, AMR6 and AMR8) did not give reasonable data during the tests. They are set white. Potential causes for that are mishandling during installation or testing prior to the cooldown or a connector or sensor was damaged during cooldown.

The five sensors that did work gave a signal of about 1 mV that changed with the external magnetic field. In addition, the output voltage depended on the supply voltage of the Wheatstone bridge (Figure C.2). 9 V block batteries were used as supply

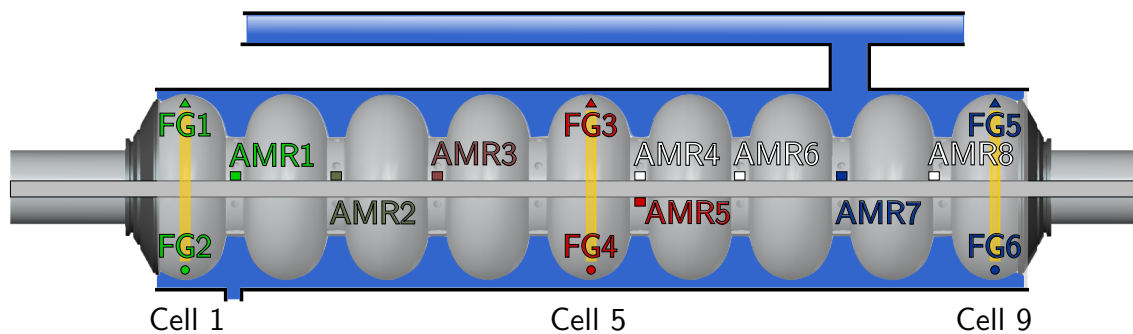


Figure E.1: Direct measurement of the magnetic field inside the cavity by six fluxgates and eight AMRs. The triangles indicate the FGs in the top of the cells and the bullets indicate the FGs in the bottom. The AMRs close to the cavity irises are marked as squares.

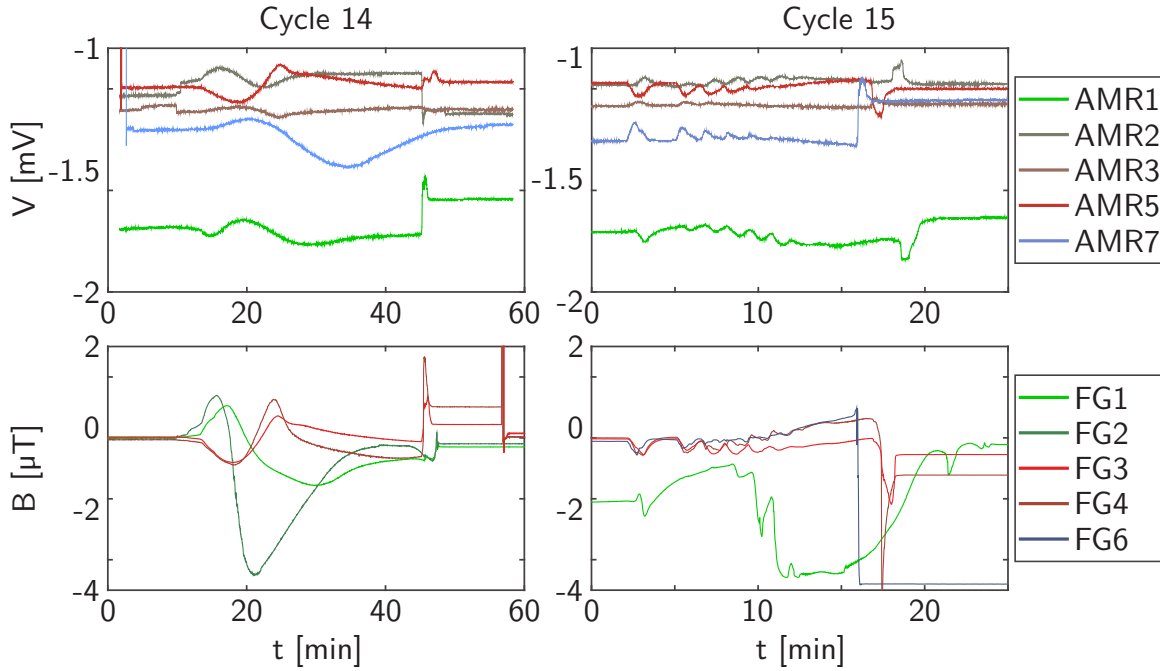


Figure E.2: Output of magnetic field sensors during thermal cycles. The top row shows the AMR signals and the bottom row shows the FG signals.

to minimize the noise. However, the voltage exhibited drifts with time depending on the state of charge, which translated to drifts in the output signal. Altogether, the voltage signal could not be converted to an absolute magnetic field. However, the change in the signal corresponding to the change in magnetic field could be measured and compared to the fluxgates.

Figure E.2 compares the AMR and the FG data obtained during two cycles. The numbers and color codes are taken from Figure E.1. The same color in AMR and FG indicates that the probes are located close to each other. The FGs were located at the equators and the AMRs at the irises. Nevertheless, a qualitatively good agreement was achieved. Especially the data of Cycle 15 shows how the small and fast oscillations that arise from the instabilities in the cryoplant during the beginning of the cooldown are detectable with both, the AMRs and the FGs. Figure E.3 shows a direct comparison of the data for the fluxgate at the top of cell 5 and the AMR between cells 5 and 6. The oscillations were detected at the same time while the phase transition was delayed at FG3 because the phase transition started at cell 9 and moved towards cell 1. It hence reached the AMR first. The amplitude of the oscillations was 500 nT measured by the FG and 65 μ V measured by the AMR. After the transition at $t = 18$ min, the steady field level exhibits a noise of 4 nT at the FG and of 3 μ V at the AMR. From that it can be roughly estimated that the AMR sensor

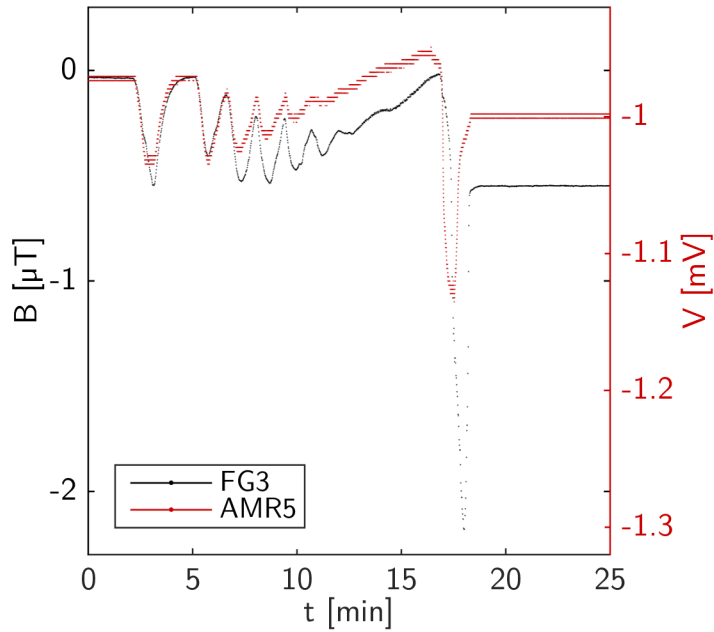


Figure E.3: Direct comparison of fluxgate (at the equator at the top of cell 5) and AMR (at the iris between cell 5 and cell 6) signal during Cycle 15.

can resolve magnetic fields down to 25 nT .

In summary, AMR technology was successfully operated in an SRF test at our institute with a promising resolution. The results open new possibilities for the investigation of trapped flux, which is discussed further in the outlook chapter at the end of the thesis.

Bibliography

- [1] S. Witman, “Ten things you might not know about particle accelerators,” *Symmetry Magazine*, Fermi National Accelerator Laboratory, Retrieved 21 Apr 2014.
- [2] J. Knobloch, “Superconducting RF: Enabling technology for modern light sources,” in *Synchrotron Light Sources and Free-Electron Lasers* (E. Jaeschke, S. Khan, J. R. Schneider, and J. B. Hastings, eds.), pp. 505–559, Springer International Publishing, 2016.
- [3] H. Padamsee, J. Knobloch, and T. Hays, *RF Superconductivity: Science, Technology, and Applications*. Wiley-VCH, 2008.
- [4] J. Galayda, “The new LCLS-II project: Status and challenges,” *Proceedings of the Linear Accelerator Conference*, p. 404, 2014.
- [5] R. A. Byrns and M. A. Green, *An Update on Estimating the Cost of Cryogenic Refrigeration*, pp. 1661–1666. Boston, MA: Springer US, 1998.
- [6] B. Aune et al., “Superconducting TESLA cavities,” *Phys. Rev. ST Accel. Beams*, vol. 3, p. 092001, Sep 2000.
- [7] M. Altarelli, R. Brinkmann, M. Chergui, W. Decking, B. Dobson, S. Düsterer, G. Grübel, W. Graeff, H. Graafsma, J. Hajdu, J. Marangos, J. Pflüger, H. Redlin, D. Riley, I. Robinson, J. Rossbach, A. Schwarz, K. Tiedtke, T. Tschentscher, I. Vartanians, H. Wabnitz, H. Weise, R. Wichmann, K. Witte, A. Wolf, M. Wulff, and M. Yurkov, eds., *The European X-Ray Free-Electron Laser: Technical design report*. DESY XFEL Project Group, 2007. ISBN 3-9809534-0-8.
- [8] E. Jensen, “Progress of the conceptual design work towards the different FCC-hh and FCC-ee RF systems,” *TTC meeting, Paris*, 2016.
- [9] P. Dhakal, G. Ciovati, G. R. Myneni, K. E. Gray, N. Groll, P. Maheshwari, D. M. McRae, R. Pike, T. Proslie, F. Stevie, R. P. Walsh, Q. Yang, and J. Zasadzinski,

- “Effect of high temperature heat treatments on the quality factor of a large-grain superconducting radio-frequency niobium cavity,” *Phys. Rev. ST Accel. Beams*, vol. 16, p. 042001, Apr 2013.
- [10] A. Grassellino, A. Romanenko, D. Sergatskov, O. Melnychuk, Y. Trenikhina, A. Crawford, A. Rowe, M. Wong, T. Khabiboulline, and F. Barkov, “Nitrogen and argon doping of niobium for superconducting radio frequency cavities: A pathway to highly efficient accelerating structures,” *Superconductor Science and Technology*, vol. 26, no. 10, p. 102001, 2013.
- [11] P. Dhakal, G. Ciovati, and G. Myneni, “A path to higher Q_0 with large grain niobium cavities,” *arXiv:1205.6736v1*, 2012.
- [12] D. Gonnella, J. Kaufman, and M. Liepe, “Impact of nitrogen doping of niobium superconducting cavities on the sensitivity of surface resistance to trapped magnetic flux,” *Journal of Applied Physics*, vol. 119, no. 7, 2016.
- [13] P. Kneisel, O. Stoltz, and J. Halbritter, “Investigation of the surface resistance of a niobium-cavity at s-band,” *IEEE Transactions on Nuclear Science*, vol. 18, pp. 158–159, 1971.
- [14] O. Kugeler, W. Anders, A. Neumann, and J. Knobloch, “Improving the intrinsic quality factor of SRF cavities by thermal cycling,” *Proceedings of the 15th International Conference on RF Superconductivity*, p. 724, 2011.
- [15] N. Valles, R. Eichhorn, F. Furuta, M. Ge, D. Gonnella, D. Hall, Y. He, V. Ho, G. Hoffstaetter, M. Liepe, T. O’Connell, S. Posen, P. Quigley, J. Sears, and V. Veshcherevich, “Record quality factor performance of the prototype Cornell ERL main linac cavity in the horizontal test cryomodule,” *Proceedings of the 16th International Conference on RF Superconductivity*, 2013.
- [16] O. Kugeler, J.-M. Vogt, and J. Knobloch, “Influence of the cooldown at the transition temperature on the SRF cavity quality factor,” *Proceedings of the 16th International Conference on RF Superconductivity*, p. 370, 2013.
- [17] J.-M. Vogt, O. Kugeler, and J. Knobloch, “Impact of cool-down conditions at T_c on the superconducting RF cavity quality factor,” *Phys. Rev. ST Accel. Beams*, vol. 16, p. 102002, Oct 2013.

- [18] J.-M. Vogt, O. Kugeler, and J. Knobloch, “High- Q operation of superconducting RF cavities: Potential impact of thermocurrents on the RF surface resistance,” *Phys. Rev. ST Accel. Beams*, vol. 18, p. 042001, Apr 2015.
- [19] J.-M. Köszegei, O. Kugeler, and J. Knobloch, “High- Q operation of SRF cavities: The impact of thermocurrents on the RF surface resistance,” *Proceedings of the 17th International Conference on RF Superconductivity*, 2015.
- [20] O. Kugeler, J.-M. Köszegei, J. Knobloch, A. Grassellino, O. Melnychuk, A. Romanenko, and D. Sergatskov, “Horizontal testing and thermal cycling of an N-doped TESLA type cavity,” *Proceedings of the 17th International Conference on RF Superconductivity*, 2015.
- [21] G. Ciovati, “AC/RF Superconductivity,” *Proceedings of the CERN Accelerator School: Superconductivity for Accelerators*, pp. 57 – 75, 2014.
- [22] J. Bardeen, L. N. Cooper, and J. R. Schrieffer, “Theory of superconductivity,” *Phys. Rev.*, vol. 108, pp. 1175 – 1204, Dec 1957.
- [23] M. Tinkham, *Introduction to Superconductivity. Second Edition*. Dover Books on Physics, Dover Publications, 2004.
- [24] J. P. Turneaure, J. Halbritter, and H. A. Schwettman, “The surface impedance of superconductors and normal conductors: The Mattis-Bardeen theory,” *Journal of Superconductivity*, vol. 4, no. 5, pp. 341–355, 1991.
- [25] A. Gurevich, “Superconducting radio-frequency fundamentals for particle accelerators,” *Reviews of Accelerator Science and Technology*, vol. 5, pp. 119 – 146, 2012.
- [26] A. B. Pippard, “High-frequency resistance of superconductors,” *Nature*, vol. 162, pp. 68 – 69, 1948.
- [27] R. Kaplan, A. Nethercot, and H. Boores, “Frequency dependence of the surface resistance of superconducting tin in the millimeter wavelength region,” *Physical Review*, vol. 116, p. 270, 1959.
- [28] A. B. Pippard, “An experimental and theoretical study of the relation between magnetic field and current in a superconductor,” *Proceedings of the Royal Society of London A: Mathematical, Physical and Engineering Sciences*, vol. 216, no. 1127, pp. 547–568, 1953.

- [29] P. Flecher, J. Halbritter, R. Hietschold, and K. Hofmann, “The preparation and performance of superconducting cavities,” *Proceedings of the Linear Accelerator Conference*, p. 499, 1966.
- [30] T. Matsushita, *Flux Pinning in Superconductors*. No. 178 in Springer Series in Solid-State Sciences, Springer, 2014.
- [31] C. Vallet, M. Boloré, B. Bonin, J. P. Charrier, B. Daillant, J. Gratadour, F. Koechlin, and H. Safa, “Flux trapping in superconducting cavities,” *Proceedings of the 1992 European Particle Accelerator Conference*, p. 1295, 1992.
- [32] A. Gurevich and G. Ciovati, “Effect of vortex hotspots on the radio-frequency surface resistance of superconductors,” *Phys. Rev. B*, vol. 87, p. 054502, 2013.
- [33] A. Romanenko, A. Grassellino, O. Melnychuk, and D. A. Sergatskov, “Dependence of the residual surface resistance of superconducting RF cavities on the cooling dynamics around T_c ,” *Applied Physics Letters*, 2014.
- [34] J. M. Pierce, *The microwave surface resistance of superconducting lead, trapped magnetic flux, and a new magnetometer using superconductivity*. PhD thesis, Stanford University, 1967.
- [35] J. M. Pierce, “Residual microwave surface resistance of superconducting lead,” *Journal of Applied Physics*, vol. 44, no. 3, pp. 1342–1347, 1973.
- [36] J. M. Victor and W. H. Hartwig, “Radio-frequency losses in the superconducting penetration depth,” *Journal of Applied Physics*, vol. 39, no. 6, pp. 2539–2546, 1968.
- [37] J. P. Judish, C. M. Jones, F. K. McGowan, W. T. Milner, and P. Z. Peebles, “Measurements of the low-temperature rf surface resistance of lead at frequencies from 136 to 472 MHz,” *Phys. Rev. B*, vol. 15, pp. 4412–4424, May 1977.
- [38] M. Peiniger and H. Piel, “A superconducting Nb3Sn coated multicell accelerating cavity,” *Nuclear Science, IEEE Transactions on*, vol. 32, pp. 3610–3612, Oct 1985.
- [39] D. Dasbach, G. Müller, M. Peiniger, H. Piel, and R. Roth, “Nb3Sn coating of high purity Nb cavities,” *Magnetics, IEEE Transactions on*, vol. 25, pp. 1862–1864, Mar 1989.

- [40] H. Padamsee, “Superconducting RF cavity technology,” *Proceedings of the Linear Accelerator Conference*, p. 501, 1990.
- [41] P. Zhang, G. Rosaz, A. Sublet, M. Therasse, and W. Venturini Delsolaro, “The influence of cooldown conditions at transition temperature on the quality factor on niobium sputtered quarter-wave resonators for HIE-Isolde,” *Proceedings of the 17th International Conference on RF Superconductivity*, 2015.
- [42] F. J. Blatt, P. A. Schroeder, C. L. Foiles, and D. Greig, *Thermoelectric Power of Metals*. Plenum Press (New York), 1976.
- [43] O. Kugeler, A. Neumann, W. Anders, and J. Knobloch, “Adapting TESLA technology for future CW light sources using HoBiCaT,” *Review of Scientific Instruments*, vol. 81, no. 7, p. 074701, 2010.
- [44] M. Caruso and C. Smith, “A new perspective on magnetic field sensing,” *Sensors*, vol. 15(12), pp. 34–46, 1998.
- [45] S. Aull, O. Kugeler, and J. Knobloch, “Trapped magnetic flux in superconducting niobium samples,” *Phys. Rev. ST Accel. Beams*, vol. 15, p. 062001, 2012.
- [46] L. Bottura and K. Heinrichsen, “Field measurements,” *CERN Accelerator School - Superconductivity and Cryogenics for Accelerators and Detectors*, 2004.
- [47] F. Primdahl, “The fluxgate magnetometer,” *Journal of Physics E: Scientific Instruments*, vol. 12, no. 4, p. 241, 1979.
- [48] S. Aull, “Investigation of trapped magnetic flux in superconducting niobium samples,” Master’s thesis, Humboldt-Universität zu Berlin, 2011.
- [49] R. Wanzenberg, “Monopole, dipole and quadrupole passbands of the TESLA 9-cell cavity,” Tech. Rep. DESY-TESLA-2001-33, DESY, Hamburg, Sep 2001.
- [50] J. Knobloch, W. Anders, M. Martin, S. Bauer, M. Pekeler, D. Belomestnykh, S. Kostin, W. Möller, A. Büchner, H. Büttig, and F. Gabriel, “CW operation of the TTF-III input coupler,” *Proceedings of the Particle Accelerator Conference*, 2005.
- [51] T. Powers, “Theory and practice of cavity RF test systems,” *Proceedings of the 12th Workshop on RF Superconductivity*, p. 40, 2005.

- [52] G. Ciovati, P. Dhakal, and A. Gurevich, “Decrease of the surface resistance in superconducting niobium resonator cavities by the microwave field,” *Applied Physics Letters*, vol. 104, no. 9, 2014.
- [53] H. Potter, “Electrical resistance and thermoelectric power of the transition metals,” *Proceedings of the Physical Society*, vol. 53, no. 6, p. 695, 1941.
- [54] R. Carter, A. Davidson, and P. A. Schroeder, “Thermopower of cubic transition metals,” *Journal of Physics and Chemistry of Solids*, vol. 31, no. 10, pp. 2374 – 2377, 1970.
- [55] I. Weinberg and C. W. Schultz, “Thermoelectric power in niobium-zirconium alloys,” *J. Phys. Chem. Solids*, vol. 27, p. 476, 1966.
- [56] H. Worner, “Thermoelectric properties of titanium with special reference to the allotropic transformation,” *Australian Journal of Chemistry*, vol. 4, p. 62, 1951.
- [57] M. Vedernikov, “The thermoelectric powers of transition metals at high temperature,” *Adv. Phys.*, vol. 18, p. 337, 1969.
- [58] Quantum Design, 11578 Sorrento Valley Rd. San Diego, CA 92121-1311 USA, *Physical Property Measurement System Thermal Transport Option User’s Manual*, 2002. Part Number 1684-100B.
- [59] R. Eichhorn, C. Daly, F. Furuta, A. Ganshyn, M. Ge, D. Gonnella, D. Hall, V. Ho, G. H. Hoffstaetter, M. Liepe, J. May-Mann, T. O’Connell, S. Posen, P. Quigley, J. Sears, and V. Veshcherevich, “Thermocurrents and their role in high Q cavity performance,” *Phys. Rev. Accel. Beams*, vol. 19, p. 012001, Jan 2016.
- [60] J. Jensen, R. Stewart, W. Tuttle, H. Brechna, and A. Prodell, “Selected cryogenic data notebook, vol. 2,” *Brookhaven National Laboratory*, 1980.
- [61] M. Merio and T. Peterson, “Material properties for engineering analysis of SRF cavities,” *Fermilab Specification: 5500.000-ES-371110*, 2011.
- [62] P. Kes, J. Rolfes, and D. de Klerk, “Thermal conductivity of niobium in the purely superconducting and normal states,” *Journal of Physical and Chemical reference data*, vol. 3, 1974.

- [63] A. Crawford, “A study of thermocurrent induced magnetic fields in ILC cavities,” *arXiv:1403.7996v1*, 2013.
- [64] J.-M. Vogt for the FNAL high-Q group, “Fermilab studies of quality factor changes of a N doped cavity from vertical to dressed horizontal test,” *TTC meeting, KEK*, 2014.
- [65] D. Gonnella, R. Eichhorn, F. Furuta, M. Ge, D. Hall, V. Ho, G. Hoffstaetter, M. Liepe, T. O’Connell, S. Posen, P. Quigley, J. Sears, V. Veshcherevich, A. Grassellino, A. Romanenko, and D. A. Sergatskov, “Nitrogen-doped 9-cell cavity performance in a test cryomodule for LCLS-II,” *Journal of Applied Physics*, vol. 117, no. 2, p. 023908, 2015.
- [66] T. E. Faber and A. Pippard, “Chapter IX Kinetics of the phase transition in superconductors,” *Progress in Low Temperature Physics*, vol. 1, pp. 159–183, 1955.
- [67] F. Liu, M. Mondello, and N. Goldenfeld, “Kinetics of the superconducting transition,” *Phys. Rev. Lett.*, vol. 66, pp. 3071–3074, Jun 1991.
- [68] H. Frahm, S. Ullah, and A. T. Dorsey, “Flux dynamics and the growth of the superconducting phase,” *Phys. Rev. Lett.*, vol. 66, pp. 3067–3070, Jun 1991.
- [69] S. J. Di Bartolo and A. T. Dorsey, “Velocity selection for propagating fronts in superconductors,” *Phys. Rev. Lett.*, vol. 77, pp. 4442–4445, Nov 1996.
- [70] S. Aull, S. Doebert, T. Junginger, and J. Knobloch, “High resolution surface resistance studies,” *Proceedings of the 16th International Conference on RF Superconductivity*, 2013.
- [71] A. Romanenko, A. Grassellino, A. Crawford, D. Sergatskov, and O. Melnychuk, “Ultra-high quality factors in superconducting niobium cavities in ambient magnetic fields up to 190 mG,” *Applied Physics Letters*, vol. 105, p. 234103, 2014.
- [72] T. Kubo, “Model of flux trapping in cooling down process,” *Proceedings of the 17th International Conference on RF Superconductivity*, 2015.
- [73] J. McCord, “Progress in magnetic domain observation by advanced magneto-optical microscopy,” *Journal of Physics D: Applied Physics*, vol. 48, no. 33, p. 333001, 2015.

- [74] A. Polyanskii, P. Lee, A. Gurevich, Z. Sung, and D. C. Larbalestier, “Magneto-optical study high-purity niobium for superconducting RF application,” *Proceedings of the First International Symposium on the Superconducting Science and Technology of Ingot Niobium*, 2010.
- [75] M. Wang, T. Bieler, D. Kang, C. Compton, D. C. Larbalestier, A. Polyanskii, and Z. Sung, “Introduction of precisely controlled microstructural defects into SRF cavity niobium sheets and their impact on local superconducting properties,” *Proceedings of the 17th International Conference on RF Superconductivity*, 2015.
- [76] J. Knobloch, *Advanced Thermometry Studies of Superconducting Radio-Frequency Cavities*. PhD thesis, Cornell University, 1997.
- [77] M. Müller, *Fluxgate Magnetometer*. Lecture Notes - Department of Meteorology und Geophysics, University of Vienna, WS 2006/07.

Acknowledgements

I would like to use this very last page to acknowledge the tremendous support, which I received during the last years. First and foremost, I would like to thank my supervisors Prof. Jens Knobloch and Dr. Oliver Kugeler, as well as my appraiser Prof. Andreas Jankowiak.

I am also grateful to the FG-SRF for many open doors, in particular Dr. Axel Neumann, Dr. Adolfo Velez, Dr. Wolfgang Anders and Sebastian Keckert. Similarly, I extend my thanks the colleagues of FG-IA, Jens Völker and Martin Schmeißer. Conversations with all of them have been of enormous help.

Not one single test would have been possible without the efforts of our engineers - Michael Schuster, Sascha Klauke, André Frahm, Hannes Stein, Stefan Rotterdam, Axel Hellwig and former colleague Dirk Pflückhahn.

I also want to thank the undergraduate researchers who have worked on some parts of the experiments - Elizabeth Mondragón, Matthias Wegen Anna-Lena Becker, Mark Krzyzagorski, Benedikt Schmitz and Khaled Alomari.

During the past years, I heavily relied on a large number of collaborations. I extend my thanks to Axel Matheisen from DESY who helped out with a cavity and BCP treatments for several samples. Niobium samples were provided by Bernd Spaniol from Heraeus and Sarah Aull from CERN. I am grateful for the excellent support by the Department Sample Environments, especially Dr. Bastian Klemke, during the PPMS measurements. The magneto-optical measurements were carried out by the group of Prof. Rudolf Schäfer from the IFW Dresden. I extend my thanks to them, and specifically Stefan Pofahl, for their support.

Furthermore, I want to thank the HZB and the “PhD student research abroad” program for providing me with the opportunity to visit Fermilab for three month. It was a memorable stay. Just as much, I am grateful to Anna Grassellino and her group who hosted me and furthermore supplied me with the N-doped cavity for the tests in HoBiCaT.

On a more personal level, a huge thank you to my friends and my family - my husband Andreas, my mother Heidrun, my pfathi Rainer, my sisters Elli and Hanna - for their love, support and encouragement through the years.